# Integrated Computational and Experimental Design of Functionally Graded Materials Made with Additive Manufacturing

by

**Noah Sargent**

Bachelor of Science in Mechanical Engineering, University of Pittsburgh, 2019

Submitted to the Graduate Faculty of the

Swanson School of Engineering in partial fulfillment

of the requirements for the degree of

Doctor of Philosophy

in Materials Science and Engineering

University of Pittsburgh

2023

UNIVERSITY OF PITTSBURGH

SWANSON SCHOOL OF ENGINEERING

This dissertation was presented

by

**Noah Sargent**

It was defended on

August 22, 2023

and approved by

Brian Gleeson, Department Chair, Mechanical Engineering and Materials Science

Jörg Wiezorek, Professor, Mechanical Engineering and Materials Science

Youngjae Chun, Professor, Industrial Engineering

Chantal K. Sudbrack, Ph.D., National Energy Technology Laboratory

Richard Otis, Ph.D., NASA Jet Propulsion Laboratory

Dissertation Director: Wei Xiong, Professor, Mechanical Engineering and Materials Science

# Integrated Computational and Experimental Design of Functionally Graded Materials Made with Additive Manufacturing

Noah Sargent, PhD

University of Pittsburgh, 2023

Using the directed energy deposition (DED) additive manufacturing (AM) process, functionally graded materials (FGMs) are manufactured by dynamically controlling the feedstock composition, yielding one-piece multi-material components with location-specific properties. The development of FGMs has enabled new technological capabilities and an improved understanding of the underlying process-structure-property relationships in AM processes. The goal of this dissertation is to develop CALPHAD-based ICME (CALPHAD: CALculation of PHAse Diagrams, ICME: Integrated Computational Materials Engineering) models and experimental methods for designing defect-free FGMs and developing new alloys specifically designed for AM. Contributions of this dissertation to the framework for modeling FGMs include the prediction of solidification cracking susceptibility and an approach for modeling diffusion in complex multicomponent composition gradients. This modeling framework is then integrated with high-throughput experiments to discover novel AM alloys, leading to the discovery of microsegregation-aided transformation and twinning-induced plasticity in low-manganese steel. This discovery provides a new pathway for achieving transformation and twinning-induced plasticity effects in steel without heat treatment. Additional alloy development efforts aim to address the isotropic properties of AM alloys by employing powder-based DED of FGMs to reveal new relationships between composition, processing, heat treatment, and grain refinement. Next, a successful processing and heat treatment strategy for Inconel 718 and stainless steel 316L FGMs is developed. The mechanical properties of the post-processed Inconel 718 and stainless steel 316L FGM exceed those previously reported in the literature. Further investigation of the microstructural stability and oxidation performance of Inconel 718 and stainless steel 316L under cyclic oxidation at elevated temperatures improves the understanding of FGMs operating in extreme environments. This dissertation presents an integrated computational and experimental design approach for multi-material AM. Leveraging computational tools and high-throughput experiments using FGMs, novel AM alloys, and new process-structure-property relationships are discovered. The contributions of this dissertation have implications for industries seeking to enhance the functionality of AM components while reducing costs, enabling more reliable and efficient solutions using multi-material additive manufacturing.

## Table of Contents

# List of Tables

# List of Figures

# Preface

This dissertation is dedicated to those who supported me throughout my eight years of study at the University of Pittsburgh. To Laurel, we began this journey together, and you remained beside me through every step. The sacrifices you've made to support my studies will forever hold a special place in my heart. To my friends and colleagues, your companionship has been indispensable, and I will always cherish the memories we made. To my parents, your constant encouragement has been my guiding light. To professor Wei Xiong, I extend my heartfelt gratitude to you for responding to my cold email four years ago, seeing potential in me, and helping me find my passion for learning. Your guidance has taught me hard and smart working. I will always expect victory in all my pursuits.

This Ph.D. dissertation was supported by a National Aeronautics and Space Administration (NASA) Space Technology Research Fellowship under the mentorship of mentorship of Dr. Richard Otis, Grant: 80NSSC19K1142. Part of this research was carried out at the Jet Propulsion Laboratory, California Institute of Technology, under a contract with NASA (80NM0018D0004). The National Science Foundation under Faculty Early Career Development Award: CMMI 2047218 funded a portion of this work. Funding for atom probe tomography was provided by Center for Nanophase Materials Sciences (CNMS) Proposal ID: CNMS2021-A-00676. CNMS is a US Department of Energy, Office of Science User Facility at Oak Ridge National Laboratory. The Additive Manufacturing Alloys for Naval Environments (AMANE) program through the Office of Naval Research (Contract No.: N00014-17-1-2586) funded a portion of this work. The Nanoscale Fabrication and Characterization Facility (NFCF) and the Swanson Center for Product Innovation (SCPI) at the University of Pittsburgh provided training and equipment.

# 1.0 Introduction

The development of additive manufacturing (AM) methods has changed the landscape of materials research over the past decade. Researchers are just beginning to realize the full potential of the AM process. Untapped potential lies in its ability to fabricate parts that utilize built-in composition gradients to yield optimized location-specific material properties, known as functionally graded materials (FGMs) [1-5]. FGMs are typically manufactured using the directed energy deposition (DED) process through a dynamic variation of composition in consecutive layers along the building direction. Before the introduction of the DED processes, diffusion bonding, vapor deposition, laser cladding, and dissimilar welding were used to manufacture FGMs [6-12]. Modern manufacturing of FGMs using DED enables efficient production of complex composition gradients on the macroscale, facilitating efficient analysis of the unexplored composition space between two or more alloys. In recent years, the materials research community has tapped into this potential to discover innovative new materials for AM [13-17].

Improvements in AM technology developed over the past decade have allowed researchers to push the boundaries of alloy development using FGMs. This recent scientific interest has led to the discovery of new materials, improved the understanding of fundamental process-structure-property relationships, and enabled modern technologies by combining multiple materials with complementary properties into one-piece components. Manufacturing of FGMs is a promising field of research with applications in alloy design and advanced manufacturing. However, there is a significant gap in the understanding of the fundamental process-structure-property relationships that control the formation of defects as a function of composition in dissimilar alloy systems.

Using CALPHAD-based ICME (CALPHAD: CALculation of PHAse Diagrams, ICME: Integrated Computational Materials Engineering) [18-20] modeling and high-throughput experiments, this dissertation designs defect-free FGMs and develops innovative new alloys for AM. In Chapter 1.0, the motivation and goal of this dissertation are discussed with context from a review of the relevant literature. Chapter 2.0 discusses the development of new modeling capabilities built on top of the existing CALPHAD-based modeling framework for FGMs [1, 3, 21, 22]. These new capabilities include the prediction of solidification cracking susceptibility as a function of composition and processing conditions [23]. Additionally, an approach for predicting the kinetic stability of FGMs during heat treatment and high-temperature operation is proposed. This improved CALPHAD-based ICME modeling framework is then applied to expand the understanding of multi-material AM and discover innovative new materials designed to take advantage of the unique characteristics of the AM process. Chapter 3.0 covers an alloy discovery effort with the goal of developing a novel transformation and twinning-induced plasticity (TRIP and TWIP) steel using high-throughput experiments with dissimilar steel FGMs. Using an integrated experimental and computational approach, a pathway for achieving microsegregation-aided TRIP and TWIP effects in low-manganese steel without heat treatment was discovered. Chapter 4.0 further explores the use of FGMs for accelerating alloy development by investigating the process-structure-property relationships that control grain size and recrystallization in the composition space between stainless steel and nickel-based superalloys during printing and post-processing. In the last main chapter (5.0), the microstructure evolution and mechanical properties of stainless steel 316L and Inconel 718 superalloy FGMs after printing, post-processing, and high-temperature cyclic oxidation are discussed. Finally, this dissertation's scientific contributions are summarized in chapter 6.0 along with directions for future research on FGMs.

## 1.1 Motivation

AM is essential to the development of next-generation technologies and is a key element of Industry 4.0 [24]. Recent advances in rapid prototyping, materials science, and advanced manufacturing have directly resulted from the introduction of the AM process [25]. Although AM has made a significant impact on the high-tech industry, there is considerable room for further advances in the field. The clearest example of this unexploited potential is the continued use of traditional alloys designed for casting, forging, and welding, in AM processes. For example, the two most common AM alloys, stainless steel 316L (SS316L) and Inconel 718 (IN718) were invented in the early 1900s and 1962, respectively. Although these traditional engineering alloys are integral to modern technologies, they were not designed for AM and therefore fail to fully utilize its unique characteristics. One of the major objectives of this dissertation is to pioneer the development of next-generation alloys specifically designed for AM. Next-generation AM alloys should utilize the unique characteristics of AM processes, such as the rapid cooling rates, dynamic process control, and the ability to manufacture spatial gradients in composition, to produce microstructures that are impossible using traditional manufacturing methods.

The opportunity offered by the AM process is the ability to dynamically control both processing conditions and alloy composition. Innovative research has focused on exploiting AM process parameters to produce microstructures that are impossible to achieve using other manufacturing methods. For example, work by Kurnsteiner et al. [26] showed that interlayer pauses during printing can be used to alter the temperature history and produce an intrinsic heat treatment that results in a layered hard and soft microstructure inspired by ancient Damascus steel. AM also provides the flexibility to incorporate multiple materials into a single component by spatially grading the composition along the building direction and even radially within a single layer [27]. Multi-material AM adds an additional layer of complexity because process-structure-property relationships evolve as a function of composition. This added complexity presents both a challenge and an opportunity. If the fundamental process-structure-property relationships can be understood as a function of composition and processing parameters, then the complexity of the AM process can be harnessed to design the next-generation of AM alloys.

Multi-material metal structures known as FGMs are fabricated by dynamically changing the mixing ratio of two or more feedstocks in processes such as DED and wire-arc additive manufacturing (WAAM). FGMs can improve the performance of AM components through location-specific material properties, eliminating fasteners, reducing waste, and improving manufacturing flexibility. This dissertation aims to modernize the alloys used in AM processes and push for the infusion of FGMs into more applications.

Computational modeling of process-structure-property relationships is essential to the development of next-generation AM alloys and FGMs. The capability to predict non-equilibrium solidification, solid-state phase transformations, and multicomponent diffusion in complex composition gradients will facilitate efficient experiments and accelerate the development of new AM alloys. Innovation in this area will widen the range of applications for AM, improve the quality of material databases with more comprehensive standards, and lead to the development of novel AM alloys and FGMs with applications across a broad range of industries.

NASA has made a significant investment in an initiative that highlights multi-material AM and alloy development for AM as a key research area [28]. This dissertation directly contributes to this initiative by developing computational tools and experimental methods for manufacturing defect-free FGMs and designing novel AM alloys. Using CALPHAD-based ICME modeling, dissimilar alloys will be selected and joined to create defect-free FGMs. Moreover, by mixing these alloys at fixed ratios, entirely new alloys with unique properties can be derived. This approach can be applied to reduce the number of feedstock materials needed in various manufacturing contexts, thereby increasing flexibility, and reducing costs. Multi-material AM offers the ability to customize material properties for any given application using monolithic alloy mixtures with tailored properties and FGMs with location-specific properties.

Continued research on FGMs will yield transformative technological developments in high-tech industries such as aerospace. While AM has already made significant strides in high-tech industries, there is untapped potential still to be found in developing next-generation alloys specifically designed for AM processes. By exploiting AM's unique characteristics, such as rapid cooling rates and dynamic process control, this dissertation aims to develop novel AM alloys and FGMs with microstructures that are impossible to produce using traditional manufacturing methods.

## 1.2 Goal

The goal of this dissertation is to develop CALPHAD-based ICME models and experimental methods for designing FGMs made with AM.

## 1.3 Literature Review

This section reviews recent advances in metal-based functionally graded materials (FGMs) manufactured by directed energy deposition (DED). The aim of this review is to describe the current understanding of process-structure-property relationships found in FGMs made by DED, recognize gaps in existing modeling approaches, and inform the design of new compositional pathways for joining dissimilar materials that avoid defects and optimize performance. In section 1.3.1, a brief history and introduction to the DED process and its ability to manufacture FGMs is given. Several advanced engineering applications and the use of FGMs as a tool for high-throughput alloy development are then discussed in section 1.3.2 to demonstrate the potential benefits of further research in the field. Section 1.3.3 discusses familiar challenges and potential solutions for manufacturing and post-processing defect free FGMs. Then, the design of compositional pathways for joining dissimilar materials using existing CALPHAD-based ICME modeling (CALPHAD: CALculation of PHAse Diagrams, ICME: Integrated Computational Materials Engineering) approaches is discussed in section 1.3.4. Finally, section 1.3.5 provides a summary and shares a perspective on state-of-the-art FGM research.

Numerous other reviews about FGMs made with DED are also available in the literature [2, 4, 5, 29-31]. Instead of repeating the basic principles of the DED process and FGMs, this review section focuses on potential avenues for advancement in the field that have not yet received enough attention. In addition to the literature review presented here in section 1.3, brief introductions covering the most relevant literature are included at the beginning of each chapter to provide context for the research contributions made in this dissertation.

### 1.3.1 The History of Directed Energy Deposition and Functionally Graded Materials (FGMs)

The DED process [32, 33], also known as laser engineered net shaping (LENS), is the most common additive manufacturing (AM) method for metal based FGMs. In a few words, the DED process manufactures net shape AM components by blowing one or more feedstock powders into the path of a laser or electron beam, creating a melt pool that is rastered back and forth to deposit single tracks that combine to form a layer making up a slice of the desired net shape. Subsequent layers are then deposited on top of each other to build along the vertical direction. The LENS process (trademark of Sandia Corporation) was originally conceived around 1995 through research conducted at Sandia National Laboratories (SNL). Optomec, Inc., then licensed the technology from SNL with the goal of commercializing the LENS process. The first ever LENS 450 system (Optomec Inc., USA), one of the first commercial LENS/DED machines, was delivered to the Department of Materials Science & Engineering at the University of Pittsburgh over a decade ago. Since then, many research articles and dissertations (including this one) have used the LENS 450 machine to study the unique process-structure-property relationships inherent to the additive manufacturing process.

Since its invention in 1995, DED manufacturing technology has evolved to include advanced capabilities such as in-situ process monitoring [34], ultrasound assisted microstructure refinement [35] and advanced processing control [36]. Although these technological advancements have moved state-of-the-art DED forward, the most important capability of the DED process is the ability to dynamically control the composition of the deposited feedstock material. Using the DED process, alloy composition can be varied dynamically by in-situ mixing of two or more feedstocks to build spatial composition gradients into one-piece AM parts known as FGMs.

Although the concept of FGMs has been around since the 1980s [37], the advent of the DED process has ushered in a new era of research on FGMs by enabling efficient production on the macroscale without geometric limitations and greater control of spatial composition gradients. Before the introduction of the DED process, dissimilar welding/cladding [38], diffusion bonding [39], and chemical vapor deposition (CVD) [12] were used to produce FGMs. Modern manufacturing methods such as explosive welding [40] and friction stir welding [9, 41] can also manufacture multi-material joints. However, these manufacturing methods are limited to simple sharp dissimilar material interfaces or lack the scale/efficiency required to produce FGMs on the macroscale. Other AM processes, such as wire-arc additive manufacturing (WAAM) [42, 43] and laser powder bed fusion (LPBF) [44], are capable of manufacturing FGMs. Although the deposition rate of WAAM is faster than DED, the geometrical accuracy and process control of DED is much better in comparison. While the LPBF process can produce the most accurate net-shape parts, DED provides a much simpler architecture for handling multiple materials. Therefore, the DED process is the state-of-the-art manufacturing method for FGMs. Research on FGMs made by DED is a burgeoning field with applications in advanced manufacturing and alloy development.

### 1.3.2 FGMs: An Innovative Technology and a Tool for Accelerated Alloy Development

Research on FGMs has gained notoriety over the past decade through efforts in collaboration with NASA and US national labs [4, 5, 22, 45-48]. This work focused on combining two or more complementary materials within a one-piece printed component to attain material properties that are impossible using a monolithic alloy. Research interest in FGMs is driven by the potential to revolutionize the design of components operating in most extreme environments. Notable applications of FGMs include plasma-facing components in fusion reactors (tungsten-steel) [49], regeneratively cooled multi-material rocket nozzles (copper-superalloy) [50, 51], and high-temperature power generation systems (superalloy-steel) [43]. These exciting applications of FGMs are discussed here in detail. Although FGMs have been integrated into some of the most challenging applications, significant hurdles still exist to progressing their technology readiness level.

Tungsten alloys are candidates for plasma-facing materials in fusion reactors because of their high melting point, good irradiation resistance, and excellent high-temperature mechanical properties [52]. However, tungsten becomes brittle at low temperatures and is prohibitively expensive. These issues can be mitigated by utilizing irradiation-resistant steel in the cooler areas of fusion reactors using tungsten-steel FGMs. Research on tungsten-steel FGMs has primarily focused on diffusion bonded and brazed joints [53-56] using different combinations of Ni, Ta/Cu, and pure Cu interlayers to prevent intermetallic phase formation and other defects. Manufacturing tungsten-steel FGMs using DED would enable more complex interlayer designs, greater control of component geometry, and reduced manufacturing costs. Metallurgical issues associated with melting tungsten, such as its high ductile to brittle transition temperature, high melting point, and scarcity of suitable feedstock powder have hindered progress. Some success has been found with cold spray additive manufacturing of tungsten-steel FGMs, [57] but many obstacles still need to be addressed. These issues include addressing the thermal stability of tungsten-steel FGMs at high-temperatures, improving the design of printable tungsten-based AM alloys, and the development of printable interlayers used to join tungsten and steel.

The development of next-generation rocket propulsion systems using multi-material AM is an exciting application of FGMs [50, 51, 58]. Aerospace companies and government agencies (NASA, US Air Force, and US Space Force) are privately developing novel propulsion systems with FGMs serving as a key technology. Many modern rocket nozzles are designed using a bimetallic copper insert encased in a high-temperature alloy (e.g., Ni-based superalloy). High conductivity precipitation strengthened copper alloys designed for AM [59] can quickly conduct heat away from the hot inner surface of rocket nozzles using integrated cooling channels while the structural integrity of the nozzle is maintained by a high-temperature superalloy making up the outer wall. DED and brazing are the most common manufacturing methods for joining copper-superalloy bimetallic rocket nozzles. However, significant metallurgical issues such as solubility limits, thermal mismatch, and solidification cracking have plagued the manufacturing process of some designs.

Ni-based superalloys are expensive when compared to steel and therefore should only be used, when necessary, especially in cost conscious applications. One such application is power generation, where the upfront cost of next-generation high-temperature/high-efficiency steam power generation systems is high due to the need for Ni-based superalloy components. Superalloy-steel FGMs have been proposed as a potential cost saving technology for high-temperature steam power generation systems [43]. Other applications of steel-superalloy FGMs also exist in the aerospace industry.

Of the three applications of FGMs discussed here, steel-superalloy and copper-superalloy FGMs have the highest technology readiness level. Copper-superalloy bimetallic rocket nozzles designs are mature and a few steel-superalloy FGM components in power plants are in use. Tungsten-steel FGMs for fusion reactors are still in the developmental stage but hold immense potential in the race to develop nuclear fusion power plants at a reasonable cost. Although FGMs have been infused into some of the most extreme environments, significant gaps in the understanding of their thermal stability, oxidation performance, and manufacturability require further research.

These three examples of the industrial application of FGMs only scrape the surface of the technological possibilities. The field of FGMs is expected to grow in the coming years with applications across a broad range of high cost/high-performance industries such as aerospace and energy production. Another lesser-known application of FGMs is alloy development. The existing literature on FGMs can be split into two categories, joining dissimilar alloys to produce location-specific material properties for improved performance and high-throughput discovery of new AM alloys. Experimental studies on alloy discovery/design have used FGMs to efficiently investigate the composition space between combinations of high entropy alloys, bulk metallic glasses, nickel superalloys, steels, titanium alloys, aluminum alloys, and refractory materials [13-17]. Research articles by Welk et al. [13], Dobbelstein et al. [14], and Pegues et al. [15] clearly demonstrate the utility of using FGMs as a high-throughput experimental tool for accelerated alloy discovery. These publications on alloy discovery using FGMs focus on the screening of alloy compositions and the discovery of new process-structure-property relationships in unexplored multicomponent composition space.

Impactful research on FGMs should simultaneously pursue two goals. The first goal is to advance the understanding of process-structure-property relationships that control the formation of defects in multi-materials structures as a function of composition and processing conditions. Pursuing this first goal will yield new technological capabilities using optimized location-specific material properties. The second goal should be to utilize FGMs as a high-throughput experimental tool for alloy development and discovery. Mixing off-the-shelf commercial alloys using the DED process to create FGMs is an efficient method for characterizing unexplored composition space and discovering new materials [60]. The existing literature on FGMs typically pursues one of these goals at a time. Although single-track studies of FGMs have clear narratives, this dissertation pursues alloy development in parallel with research on manufacturing FGMs for advanced engineering applications (Chapters 3.0 and 4.0). Looking back at the motivation for this dissertation (section 1.1), pursuing a parallel approach to FGMs research closely aligns with NASA's goal of developing multi-material manufacturing capabilities in resource-constrained environments, such as space. The dual ability to mix feedstocks at fixed ratios to yield tailored material properties and dynamically mix feedstocks to produce FGMs with location-specific material properties will create a more flexible AM architecture. Although challenges exist, there is a defendable hypothesis that multi-material AM will dominate the future of advanced manufacturing. FGMs are an innovative technology and a tool for accelerating alloy development.

### 1.3.3 Challenges and Solutions for Defect Mitigation in FGMs

This section reviews the current methods for defect mitigation in FGMs and discusses potential avenues for further innovation. The existing literature on dissimilar welding provides a starting point for controlling defects in FGMs. However, the added processing control of DED enables more complex defect mitigation strategies for combining dissimilar materials, opening the door to new possibilities.

Defects formed in FGMs are commonly caused by solidification cracking [41], formation of brittle intermetallic phases [45], thermal property mismatches [47], processing window variation [61], residual stresses, and diffusional defects [62]. The DED process magnifies the risk posed by these defect formation mechanisms because rapid cooling rates lead to high thermal stresses. Defects are especially common in FGMs containing highly dissimilar materials.

However, even simple steel-steel FGMs can have issues with solidification cracking and degradation of material properties caused by up-hill chemical potential-driven diffusion at material interfaces. Although the cause and mitigation of these defect formation mechanisms are well understood within most commercial alloy systems (e.g., steels, Ni-based superalloys, Titanium alloys ext.) there is extraordinarily little knowledge of defect mitigation techniques in the unexplored composition space between dissimilar materials.

#### 1.3.3.1 Preventing Detrimental Phase Formation using Interlayers

The concept of an interlayer, also known as a buttering layer, originally comes from the world of dissimilar welding. Interlayers separate dissimilar materials that readily form detrimental phases. With the existing literature on dissimilar welding serving as a starting point, the emergence of DED has enabled new capabilities for manufacturing interlayers between dissimilar alloys. Using DED, it is now possible to manufacture complex multi-step interlayers and smooth compositional transitions for combining dissimilar materials.

Highly dissimilar alloys, such as steel and titanium, require a buttering layer consisting of a third alloy or series of alloys to deter the formation of intermetallic phases during joining. When deciding which alloy to use as an interlayer, the simplest design approach is to look for a principal element or series of elements that share a phase diagram free of detrimental phases with both the principal elements of the alloys being joined. The driving principle of this approach is to eliminate detrimental intermetallic compounds using an isomorphous or multi-phase solid solution transition layer between dissimilar materials. With this simple approach, binary phase diagrams can be used to assess the feasibility of potential interlayer alloys.

One example of this simplistic yet powerful design approach is the use of Ni-Cr-V interlayers to prevent the formation of Fe-Ti intermetallic phases in stainless steel and titanium

FGMs [46, 63]. Using pure Ni-Cr-V elemental feedstocks, steel and titanium alloys can theoretically be joined through a multi-step solid solution phase interlayer. Steel is joined to Ni, Ni is joined with Cr, Cr is joined with V, and then finally V is joined with a titanium alloy. This approach can achieve a solid solution phase transition layer free of intermetallic phases between steel and titanium. Taking this roundabout path through the Ni-Cr-V ternary avoids the sigma phase (formed in the Ni-V binary phase diagram) while separating the Fe and Ti alloys which are joinable with Ni and V, respectively. This transition layer design is complex and is difficult to visualize in two dimensions. Thermodynamic calculations can help visualize this interlayer design using phase diagrams (see section 2.3). However, visualization of higher-order phase diagrams with more than three components is technically challenging in two dimensions [64]. Innovative approaches for visualizing high-order phase diagrams and computationally generated composition pathways will improve the ability to design complex interlayers for joining dissimilar materials.

The added complexity of multi-step buttering layers can cause unforeseen consequences that have typically been overlooked in previous studies [46, 63]. Below are a few lessons learned and considerations for future designs of interlayers between incompatible alloys.

1. Increased hardness from solid solution strengthening near the solubility limits of solid solution phases can cause brittle failure (e.g., BCC-Cr with supersaturation of Ni).
2. Variations in the melting points of mixed feedstocks, especially pure elemental powders, can lead to incomplete melting. Therefore, pre-alloyed powder (if available) is usually better than mixing pure elemental feedstocks.
3. Pure elements, such as Cr, can be susceptible to impurity-induced embrittlement and may require additions of alloying elements to improve manufacturability [65]. Careful control of the manufacturing environment is also essential to success.

4. The kinetics controlling the formation of topologically closed packed (TCP) phases with complex crystal structures, such as the sigma phase, is slow when compared to intermetallic phases like FeTi with a simpler crystal structure. Therefore, future interlayer designs should consider both thermodynamic and kinetic effects to create a more comprehensive design approach. For example, it may be allowable to pass through regions of TCP phase stability if the kinetics of formation is slow and thermal stability is not a concern.
5. Although smooth composition gradients can mitigate stress from differences in thermal expansion, the solidification cracking susceptibility of the deposited mixtures along the composition gradient must be considered. When a sharp composition transition is possible, it is typically the best choice for simplicity.
6. As interlayer designs get more complex, the need for more advanced thermodynamic and kinetic models will grow. New tools for visualization of multicomponent phase diagrams also have potential.

#### 1.3.3.2 Mitigating Diffusional Defects

During heat treatment and high-temperature operation, elemental diffusion in FGMs is driven by gradients in composition and chemical potential. Diffusion can affect mechanical properties at material interfaces, especially in sharp composition gradients where the driving force for diffusion is high. The most common example of diffusional defects in FGMs is the up-hill diffusion of carbon at the interface of dissimilar steels. Even if the carbon content of the two materials is the same, differing concentrations of alloying elements can cause the rapid chemical potential-driven diffusion of carbon at low temperatures [66]. In steels, even slight changes in carbon concentration can have adverse effects on the phase equilibria and mechanical properties.

Since carbon occupies the interstitial sites of solid solution phases in steel, carbon diffusion is fast. This means that even short heat treatments can result in significant diffusion lengths, imperiling the properties of dissimilar steel joints. Gradual composition gradients have been proposed to mitigate the detrimental effects of chemical potential-driven carbon diffusion in FGMs [62]. Spreading the chemical potential gradient out over a longer distance using a gradual compositional transition between dissimilar steels reduces the slope of the chemical potential gradient, thus lowering the driving force for diffusion [67]. DED's ability to control spatial composition gradients is a useful tool for preventing diffusional defects in FGMs which was previously impossible using dissimilar welding.

There is a limited number of studies on diffusion in FGMs, which is surprising given that they contain steep concentration gradients and have many high-temperature applications. Some inspiration can be drawn from research on diffusion couples [68, 69] and the heat treatment of dissimilar welds, such as Darken's famous experiment [66]. However, diffusional effects in the complex multi-step interlayer designs, such as the Ni-Cr-V interlayer design discussed in section 1.3.3.1, remain unstudied. Future work should focus on developing a modeling methodology capable of predicting diffusion pathways in complex multi-step interlayers because present studies have only focused on diffusion in direct and gradual transitions between dissimilar materials. Modeling approaches for predicting diffusion in complex interlayer designs will face several challenges. These challenges include a lack of comprehensive mobility databases, the high computational expense of existing multicomponent diffusion models, the complexity of multi-phase diffusion, and difficulties visualizing the phase equilibria along multicomponent diffusion pathways. Section 2.3 of this dissertation attempts to address these challenges by proposing a novel modeling approach for complex multi-step interlayers. Proper models for diffusion in complex multi-step interlayers will create a more comprehensive design approach for FGMs by including both thermodynamic and kinetic modeling.

Another diffusional defect that deserves further consideration in FGMs is Kirkendall void formation. The Kirkendall effect, discovered in 1947 [70], describes the movement of the interface between two dissimilar materials caused by an imbalance in the diffusional flux across the interface. Experimental evidence of the Kirkendall effect was discovered by tracking the movement of an interface between copper and alpha brass (Cu-Zn) in a diffusion couple relative to inert fiduciaries placed at the original interface [70]. Since the diffusion of Zinc is much faster than Cu, the material interface moved relative to the stationary inert fiduciaries because of the flux imbalance. An important consequence of the Kirkendall effect is the formation of Kirkendall voids, which form because of a flux imbalance across a material interface. If there is a net flux of substitutional atoms across an interface, there will be a flux of vacancies in the opposite direction. Over time, these vacancies will coalesce into Kirkendall voids that create stress concentrations. Kirkendall voids have been known to sever electrical connections between soldered SnPb/Cu joints [71, 72]. Risks of Kirkendall void formation should be considered in future designs of FGMs, especially in high-temperature applications with long lifetime requirements. An established theory for predicting the net flux imbalance across multicomponent material interfaces is available [73]. Modern diffusion modeling tools, such as KAWIN [74] and DICTRA [75, 76], can simulate the net flux of voids across material interfaces and can predict void fraction [77]. The existing literature on Kirkendall void prediction focuses on simple cases such as diffusion couples and coatings [77, 78]. Complex multi-step interlayer designs for FGMs made with DED will require innovative approaches for predicting Kirkendall void formation because comprehensive thermodynamic and mobility databases for dissimilar multicomponent material systems are not currently available.

#### 1.3.3.3 Solidification Cracking Defects

Solidification cracking continues to afflict the manufacturability of FGMs made with DED. Rapid cooling rates and high residual stresses during the DED process further compound cracking issues in FGMs. Although there are well-established methodologies for mitigating solidification cracking in welding literature, predicting the solidification cracking susceptibility of complex composition gradients is much more challenging. This section will discuss the established theories behind solidification cracking and models for predicting an alloy's susceptibility to it. It should be noted that the models discussed in this section have not yet gained mainstream attention in the field of FGMs. One of the major contributions of this dissertation is the recognition and integration of a solidification cracking model into the existing CALPHAD-based ICME framework for FGMs (see section 2.0).

Solidification cracking, also known as hot cracking, occurs at the end of the solidification when increased liquid density and narrow channels between dendrite arms make it difficult for liquid to fill voids [79]. These voids can serve as initiation sites for cracks that are then propagated by thermal stresses, imperiling the mechanical properties of the alloy. In the DED process, rapid cooling rates exacerbate an alloy's susceptibility to solidification cracking. Although the DED process offers many benefits for manufacturing FGMs, an increased risk of solidification cracking is the main drawback. Integration of thermal models for AM processes with microstructure models for predicting solidification cracking susceptibility will improve the CALPAHD-based ICME framework for FGMs [23].

Several models for predicting the susceptibility of a material to solidification cracking exist in the literature [80-82]. Solidification range is the original design factor when assessing the solidification cracking susceptibility of a material. The logic behind using solidification range as an indicator of solidification cracking risk is as follows, the more time a material spends in the mushy zone (solid + liquid), the higher the risk of solidification cracking susceptibility. Or in other words, the longer an alloy spends as mostly solid (>90% solid), the more difficult is for liquid to fill the voids between dendrite arms. Thus, increasing the risk of solidification cracking. In the early 1980s, Clyne and Davies [80] improved upon this approach by using the Scheil-Gulliver model for non-equilibrium solidification to estimate the temperature range over which an alloy exists in the mostly solid region. Later Kou and collaborators [81-83] developed a more refined approach based on computing the slope of the square root of solid fraction vs. temperature curve predicted by the Scheil-Gulliver model. The Kou criteria is based on the logic that the narrowness of pathways between secondary dendrite arms is related to the risk of solidification cracking susceptibility. By calculating the slope of the square root of solid fraction vs. temperature curve, determined from the Scheil-Gulliver model, the Kou criteria correlates liquid feeding ability with the risk of solidification cracking susceptibility. Creating a qualitative index for comparing the relative risk of solidification cracking susceptibility between different alloys. The Kou criteria was originally developed for asses the weldability of aluminum alloys but can be extended to other alloy systems and FGMs.

### 1.3.4 Modeling of Functionally Graded Materials using CALPHAD

The power of the CALPHAD approach lies in its sound experimental foundation and ability to make extrapolative predictions in unexplored multicomponent composition space [19]. CALPHAD can handle added complexity of dissimilar alloy mixtures and complex interlayers contained within FGMs. Whereas high-fidelity materials modeling approaches, such as density functional theory, phase field, and molecular dynamics, cannot handle complex multicomponent problems with kinetic and thermodynamic factors. CALPHAD modeling has demonstrated the ability to predict the phase equilibria and non-equilibrium solidification behavior of FGMs made with DED [21, 22]. However, there is still room to improve the existing CALPAHD-based modeling frameworks for FGMs. Through careful review of the literature, this section identifies several opportunities for further development of CALPAHD-based ICME models for FGMs that are later discussed in Chapter 2.0.

Thermodynamic equilibrium calculations using CALPHAD software are a useful tool for assessing the compatibility of dissimilar alloys, designing interlayers, and evaluating post-processing routes for FGMs. Material to material thermodynamic calculations, binary/ternary phase diagrams, and several types of property calculations are possible using CALPHAD software tools such as Thermo-Calc [76] and PyCalphad [84]. These models rely on thermodynamic assessments to make predictive extrapolations into unexplored composition space. The ability to treat composition as a variable makes CALPHAD modeling an essential tool for predicting the behavior of FGMs. With a few assumptions, it is even possible to simulate non-equilibrium/metastable thermodynamic states using only thermodynamic data.

The Scheil-Gulliver (Scheil) model, developed in the mid-1900s and later implemented into Thermo-Calc software [85], is commonly used to predict non-equilibrium solidification reactions in FGMs. The Scheil model uses a few simple assumptions to predict non-equilibrium reactions using equilibrium thermodynamics. The assumptions of the Scheil model are:

1. Redistribution of solute is neglected by assuming that solute incorporated into the solid stays where it is and does not diffuse. This assumption describes the case where cooling occurs infinitely fast.
2. Diffusion is infinitely fast in the liquid. Therefore, the composition of the liquid is considered uniform during solidification.
3. Local equilibrium is held at the solid liquid interface according to the lever rule.
4. The solidification rate is constant.

With these assumptions, the Scheil model can extrapolate equilibrium thermodynamic data to make simple yet powerful predictions about non-equilibrium solidification. Since cooling rates in AM processes are fast ($10^3$-$10^6$ K/s), the assumptions of the Scheil model align well with the AM process. Researchers have applied the Scheil-Gulliver model to AM alloys and FGMs and found it reasonably accurate if a proper thermodynamic database is available [21, 22]. The Scheil model has been coupled with the solidification cracking susceptibility models discussed in section 1.3.3.3 to study weldability. However, the ability to predict the solidification cracking susceptibility of FGMs has not been evaluated.

Predicting diffusion during heat treatment and high-temperature operation is an important capability for designing FGMs operating in harsh environments. Diffusion modeling tools, such as KAWIN [74] and DICTRA [75, 76] can simulate multicomponent diffusion problems in two dimensions. Two important kinetic modeling problems that warrant further study are isothermal diffusion and kinetic solidification models that consider back diffusion and thermal history.

Although diffusion modeling has been successfully applied to simulate diffusion couples and dissimilar welds, awareness of the relevance of these tools to FGMs is limited.

Researchers have also coupled CALPHAD modeling with path planning algorithms to design compositional pathways in FGMs that avoid defects [86, 87]. This research has demonstrated the potential of applying CALPHAD modeling to design composition pathways that avoid defects and optimize the performance of FGMs. However, the existing literature on the CALPHAD-based design of FGMs has not demonstrated a comprehensive approach capable of discovering previously unreported compositional pathways for FGMs.

### 1.3.5 Summary and Perspective on State-of-the-Art FGM Research

In summary, FGMs have garnered significant attention and research interest, particularly since the introduction of DED in 1995. DED has emerged as the most common and efficient manufacturing method for metal based FGMs, allowing for the controlled deposition of two or more feedstock materials on the macroscale for the first time. DED has opened new possibilities for the design of complex components with tailored material properties, without the geometric limitations of traditional manufacturing techniques. Moreover, research efforts in collaboration with organizations like NASA have focused on combining dissimilar materials within a single FGM component to achieve location-specific material properties. Despite the tremendous potential of FGMs, there are still challenges to overcome, such as defects arising from solidification cracking, brittle intermetallic phase formation, thermal property mismatches, processing window variation, diffusional defects, and residual stresses. To address these issues, researchers have employed CALPHAD modeling to predict phase equilibria and solidification reactions that occur during the printing of FGMs and have coupled these capabilities to path planning algorithms. This literature review highlights the significant contributions of DED technology to the development and exploration of FGMs and identifies several gaps in the state-of-the-art that require further investigation. From its inception, DED has provided a pathway for novel materials research, enabling the discovery of new materials, and revealing new process-structure-property relationships. The future of FGMs is promising, with ongoing research efforts aiming to overcome manufacturing issues and conceive of exciting new technologies.

## 2.0 A CALPHAD-Based ICME Framework for Functionally Graded Materials

CALPHAD-based ICME (CALPHAD: CALculation of PHAse Diagrams, ICME: Integrated Computational Materials Engineering) [19, 88] models are a useful tool for screening the gradient in composition between two or more alloys for potential defects including detrimental phases, solidification cracking, and differences in thermal expansion. Non-equilibrium solidification, caused by the rapid cooling rates inherent to the AM process, complicates the development of computational models for FGMs. Rapid solidification during AM causes microsegregation and leads to the formation of metastable phases in the as-built microstructure [89, 90]. Therefore, equilibrium thermodynamics cannot accurately model the highly non-equilibrium phase transformations that occur in additively manufactured FGMs. Researchers have applied CALPHAD-based models for non-equilibrium solidification to FGMs and found reasonable agreement with experimental observations [21, 22, 42]. However, further improvement of these models is needed to accurately capture the complex physics of non-equilibrium solidification as a function of composition [23]. Realizing the full potential of additively manufactured FGMs requires the development of a comprehensive modeling framework that is both efficient and accurate in multicomponent alloy systems.

This chapter proposes a framework of computational tools for creating digital twins that predict the microstructural evolution of FGMs during printing, post-processing, and high-temperature operation to evaluate the feasibility of novel designs without costly experimental studies. The integrated computational modeling approach developed in this dissertation can accelerate the development and qualification of FGMs for space flight applications. For example, a computationally designed SS316L and Ti-6Al-4V FGM, covered in section 2.3 of this chapter, was considered for use on NASA’s Mars sample return lander. Although significant gaps remain, this dissertation represents an advancement in state-of-the-art modeling for FGMs.

## 2.1 Integration of Processing and Microstructure Models for Non-Equilibrium Solidification in Additive Manufacturing

Content from the following open access journal paper is used in this chapter:

- Sargent, Noah, Mason Jones, Richard Otis, Andrew A. Shapiro, Jean-Pierre Delplanque, and Wei Xiong. 2021. "Integration of Processing and Microstructure Models for Non-Equilibrium Solidification in Additive Manufacturing" Metals 11, no. 4: 570. https://doi.org/10.3390/met11040570

Integration of models that capture the complex physics of solidification on the macro and microstructural scale with the flexibility to consider multicomponent materials systems is a significant challenge in modeling AM processes. This chapter aims to link process variables with non-equilibrium solidification by integrating AM process simulations with solidification models that consider thermodynamics and diffusion. Temperature histories are generated using a semi-analytic laser powder bed fusion (LPBF) process model and feed into a CALPHAD-based ICME (CALPHAD: Calculation of Phase Diagrams, ICME: Integrated Computational Materials Engineering) framework to model non-equilibrium solidification as a function of both composition and processing parameters. Solidification cracking susceptibility (SCS) is modeled as a function of composition, cooling rate, and GED in Al-Cu Alloys and stainless steel 316L (SS316L). Trends in SCS predicted by the model are validated by experimentally observed solidification crack length measurements of Al-Cu alloys. Non-equilibrium solidification in additively manufactured SS316L is investigated to determine if this approach can be applied to commercial materials. Modeling results show a linear relationship between GED and SCS in additively manufactured SS316L. This work shows that integration of process and microstructure models is essential for modeling solidification during AM.

### 2.1.1 Overview of State-of-the-Art Modeling for Non-Equilibrium Solidification

Deviation from equilibrium during solidification in AM processes causes microsegregation, reduction of the solidus temperature, and increased solidification cracking susceptibility (SCS) [79, 83]. Computational models with the flexibility to predict non-equilibrium solidification in multicomponent materials are limited, and new computational frameworks are desired to design the next-generation of additively manufactured materials. CALPHAD-based ICME (CALPHAD: Calculation of Phase Diagrams, ICME: Integrated Computational Materials Engineering) [18, 19] frameworks have shown the ability to model the effects of non-equilibrium solidification in both welding and AM process [45, 91-93]. However, these models typically fail to couple the thermodynamics and kinetics of materials with changes in processing parameters. Overcoming this challenge requires the integration of macroscale process simulations with microstructure level models [20] for non-equilibrium solidification.

The Scheil-Gulliver model [85] for solidification is commonly coupled with CALPHAD-based thermodynamics and provides a simple approximation of non-equilibrium solidification in the case of a well-mixed liquid and no solid back-diffusion. Scheil-Gulliver models are frequently used to model solidification in additively manufactured materials and have demonstrated success in modeling SCS using the models proposed by Clyne [80, 94] and Kou [81, 82] et al. Due to its simplicity, the Scheil-Gulliver model cannot quantitatively consider changes in the cooling rate, or the effect of cyclic heating and cooling encountered during AM processes. One-dimensional kinetic models provide a more robust prediction by considering the effect of back-diffusion across mobile phase boundaries [85] and dynamic changes in the cooling rate caused by variable processing conditions. Although one-dimensional kinetic models are more computationally expensive than Scheil-Gulliver models, they are still more efficient than high-fidelity microstructure simulation approaches such as phase-field modeling, particularly in the case of multicomponent systems. The DICTRA module within Thermo-Calc software [75] for modeling diffusion-controlled phase transformations can be used to construct one-dimensional solidification models. Lippard et al. [90] modeled the microsegregation behavior during solidification of high-alloy steel using DICTRA and found good agreement between the model prediction and experimental measurements of microsegregation using electron dispersive spectroscopy. Zhang et al. [95] showed that reliable mobility and thermodynamic assessments are necessary to accurately model solidification using DICTRA. Valiente et al. [96] used DICTRA to estimate the ferrite content in austenitic stainless-steel welds and found good agreement with the experimentally observed phase fraction. Work by Keller and Lindwall et al. [89, 97] demonstrated the potential of applying one-dimensional kinetic models to AM processes by coupling DICTRA with a finite element process model to predict microsegregation in additively manufactured Inconel 718 and 625. These efforts have demonstrated the ability of one-dimensional kinetic models to approximate non-equilibrium solidification in additively manufactured materials. However, previous works have focused on a small number of calculations and have not investigated the effects of changes in composition or processing conditions on DICTRA solidification models using high-throughput calculations. The recent development of the Thermo-Calc Python (TC-Python) Application

Programing Interface (API) has enabled high-throughput DICTRA calculations by adding the capability to automatically setup and post-processing batches of DICTRA calculations that cover large ranges in composition and processing parameters. Furthermore, DICTRA solidification models have never been coupled with models for SCS. Integrating process models with DICTRA solidification calculations and the Kou SCS criteria can be used to extend SCS models to the process level, enabling SCS to be investigated as a function of processing variables and composition. Integrating these models in a high-throughput computational framework creates a linkage between processing and microstructural effects that reveals new relationships between the AM process and non-equilibrium solidification.

### 2.1.2 CALPHAD-based ICME Framework for Non-Equilibrium Solidification in Additively Manufactured Materials

One-dimensional DICTRA solidification models are implemented using the TC-Python API to enable batch calculations as a function of both processing conditions and composition. The semi-analytic laser powder bed fusion (LPBF) process model developed by Wolfer et al. [98], which uses a green's function approach, is coupled with DICTRA simulations and the Kou SCS model [81, 82] to create a CALPHAD-based ICME framework for modeling non-equilibrium solidification in additively manufactured materials. Temperature histories under different processing conditions are used as an input for DICTRA solidification calculations to investigate the relationship between the AM process and non-equilibrium solidification. This approach couples alloy thermodynamics and diffusion with process variables such as laser power, scan speed, and global energy density (GED) to model the effect of process parameters on non-equilibrium solidification.

**Figure 1** shows how the models used in this work are coupled together using the TC-Python API to create an automated CALPHAD-based ICME framework for modeling solidification in additively manufactured materials. The TC-Python API is used to automate the Scheil-Gulliver, equilibrium, and DICTRA solidification calculations presented in this work. Integrating the LPBF process model, DICTRA calculations, and the SCS model defined by Kou using the TC-Python API expedites the tedious process of running models and post-processing data. Calculation results, such as microsegregation and SCS, are automatically post-processed and saved in a convenient text file format. This automated workflow enables the user to efficiently model large ranges in processing conditions and multicomponent composition space. The connection between macroscale process simulations and CALPHAD solidification models simplifies the complex process-structure relationship in additively manufactured materials into a resolvable problem by considering processing effects on the temperature history at a microstructural scale.

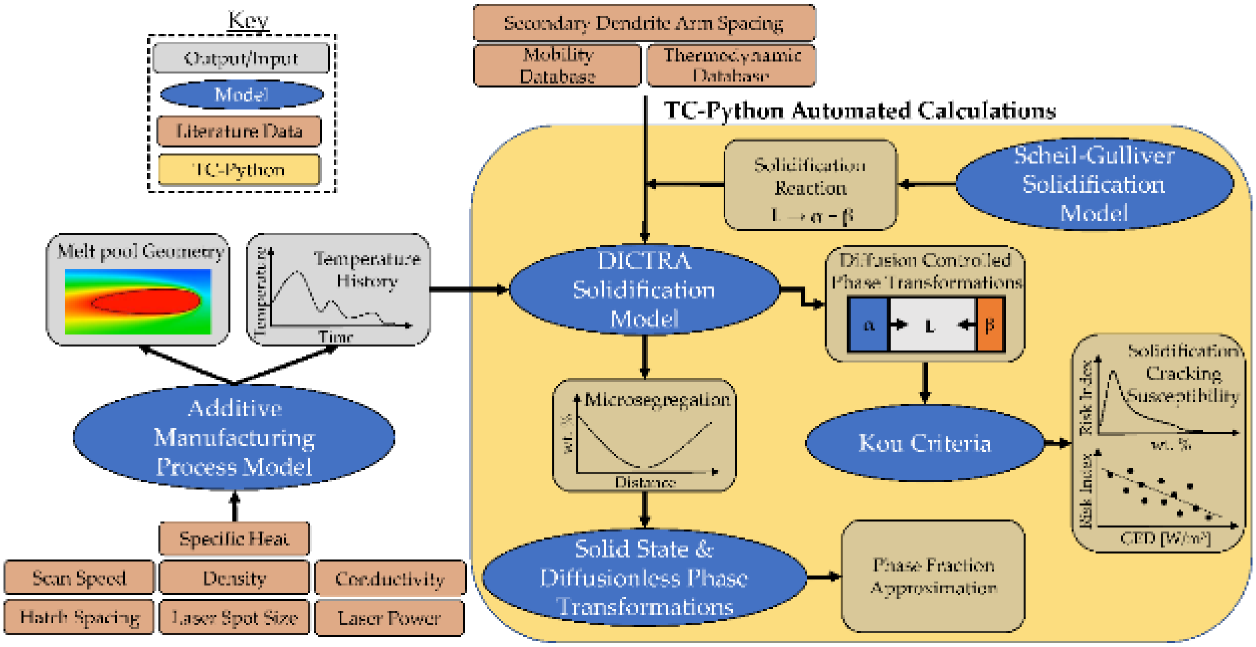

**Figure 1 – CALPHAD-based ICME framework for modeling non-equilibrium solidification in additively manufactured materials.This modeling framework integrates processing and microstructure models for non-equilibrium solidification.**

Setting up solidification calculations using DICTRA requires the user to understand the expected solidification pathway. The liquid and solid phases present during solidification and the type of solidification reaction must be known to properly set up the calculation. For example, SS316L typically undergoes a peritectic reaction with the liquid phase solidifying as BCC and then transforming into FCC. Modeling peritectic type solidification with DICTRA requires that the primary and secondary solidification phases be initialized on the same side of the one-dimensional diffusion cell. For eutectic type solidification reactions, such as the eutectic in the Al-Cu system, the primary and secondary solidification phases must be initialized on opposite sides of the one-dimensional DICTRA simulation. Conversely, the Scheil-Gulliver model does not require prior knowledge of the materials system and can be used to gain insight into the expected solidification pathway in cases where there is limited kinetic knowledge available. From the Scheil-Gulliver model, the expected solidification phases and reaction type can be determined and used to set up a higher fidelity solidification calculation using DICTRA. Using information from the Scheil-Gulliver model to determine the solidification pathway and automate the construction of high-throughput DICTRA calculations gives the modeling framework flexibility to investigate large ranges of unexplored composition space by dynamically changing the phase transformation model. Although significant challenges, such as numerical convergence issues and a deficiency of multicomponent mobility assessments still limit this approach, the CALPHAD-based ICME framework outlined in this work takes a step towards utilizing high-throughput DICTRA calculations as a tool for materials design and discovery.

Solidification cracking, also referred to as hot tearing or hot cracking, is caused by the contraction of solid in the mushy zone during solidification. When the liquid becomes trapped between dendrite arms, it causes tensile stress resulting from the lower density of the liquid when compared to the solid. SCS is related to the liquid's ability to move out of the area between dendrite arms when shrinkage occurs. The ability of the liquid to escape the region between dendrite arms is referred to as liquid feeding ability and is related to the slope of the temperature versus the square root of the solid fraction as defined by the Kou SCS model [81, 82]. The Kou SCS model can predict trends SCS and rank compositions relative to each other. This work aims to extend the Kou criteria to the process level by using DICTRA calculations to rank SCS based on processing parameters. The temperature versus the square root of the solid fraction is obtained using the Scheil-Gulliver or DICTRA solidification models and used to calculate the SCS according to Eq. (1),

$$SCS = max\left|\frac{dT}{d(f_s^{1/2})}\right|, \text{near } f_s = 1 \qquad (2\text{-}1)$$

where $f_s$ and $T$ are the total solid fraction and temperature, respectively. Computing the derivative shown in Eq. (1) from DICTRA results causes numerical issues because the time and temperature step size vary throughout the simulation. The time step of the DICTRA model used in this work is controlled by the movement of phase boundaries to ensure that changes in the rate of phase transformations are captured by the model. Variations in the time and temperature step size implies that standard finite difference approximations of Eq. (1) cannot be applied. Lagrange polynomial differentiation is used to overcome this limitation because a constant point spacing is not required for the derivative to be calculated. The numerical approximation of Eq. (1) using three-point central Lagrange polynomial differentiation [99] is given in Eq. (2),

$$\left|\frac{dT_{i+1}}{d\left(f_{s_{i+1}}^{1/2}\right)}\right| \approx \left|\begin{matrix} \left(\dfrac{f_{s_{i+1}}^{1/2}-f_{s_{i+2}}^{1/2}}{\left(f_{s_i}^{1/2}-f_{s_{i+1}}^{1/2}\right)\left(f_{s_i}^{1/2}-f_{s_{i+2}}^{1/2}\right)}\right)T_i + \\ \left(\dfrac{2f_{s_{i+1}}^{1/2}-f_{s_i}^{1/2}-f_{s_{i+2}}^{1/2}}{\left(f_{s_{i+1}}^{1/2}-f_{s_i}^{1/2}\right)\left(f_{s_{i+1}}^{1/2}-f_{s_{i+2}}^{1/2}\right)}\right)T_{i+1} + \left(\dfrac{f_{s_{i+1}}^{1/2}-f_{s_i}^{1/2}}{\left(f_{s_{i+2}}^{1/2}-f_{s_i}^{1/2}\right)\left(f_{s_{i+2}}^{1/2}-f_{s_{i+1}}^{1/2}\right)}\right)T_{i+2} \end{matrix}\right|. \tag{2-2}$$

The thermal model used to generate temperature histories for the LPBF process is the fastest semi-analytical method developed by Wolfer et al. [98]. This method is utilized because it is an order of magnitude faster than an equivalent finite element model, allowing the user to quickly sweep the chosen parameter space while introducing minimal error. The model treats the powder bed as a homogeneous continuum with uniform and constant material properties and ignores explicit melt pool dynamics, focusing instead on a conduction-based approximation. With some calibration, this conduction-only method can be used to reproduce, with a reasonable degree of accuracy, the melt pool dimensions generated by high-fidelity simulations [100]. This calibration involves adjustment of the volumetric source term and a selection of material properties representative of the material at elevated temperatures. When high-temperature material properties are unavailable or the materials system is unstudied, CALPHAD databases can be used to determine the density, specific heat, conductivity, and Gibbs free energy as a function of composition and temperature [20]. The significant speed increase over traditional methods is achieved by using a green's function solution to the reduced-order conduction-based model. This semi-analytical solution takes the form of a Gaussian filtering function and is fast because it is computationally simple and allows for the use of larger time steps and coarser meshes. Though the long-time step results in a more complicated laser source term, it can be re-used for identical time-steps, maintaining the speed of the model.

### 2.1.3 Evaluation of Solidification Modeling Framework for Binary Al-Cu Alloys

Non-equilibrium solidification of Al-Cu alloys is modeled to validate the ability of DICTRA to predict trends in SCS as a function of the cooling rate. DICTRA calculations for the Al-Cu system are set up using the eutectic phase transformation model, a cell size of 1µm, and a constant cooling rate. The TCAL7 and MOBAL5 databases released with Thermo-Calc software version 2020b are used. The liquid, FCC, and $Al_2Cu$ phases are included in the model, and all metastable phases are suspended. The effect of nucleation barriers is also neglected, and a planar geometry is used for all calculations. Three constant cooling rates, $-10^3, -10^4,$ and $-10^5$ K/s, were investigated to determine if DICTRA can accurately model the reduction of the solidus temperature caused by microsegregation and match the experimentally observed trend of SCS reported in the literature. **Figure 2(a)** shows the solidus and liquidus temperature predicted using the equilibrium, Scheil-Gulliver, and DICTRA models for solidification. DICTRA predicts a decreasing solidus temperature with an increase in the cooling rate. As the cooling rate is increased, the solidus temperature predicted by DICTRA approaches the result of the Scheil-Gulliver model.

The liquidus temperature is predicted to be the same by all models investigated in this work because all nucleation barriers are assumed to be negligible. **Figure 2(b)** shows the SCS predicted by the Scheil-Gulliver and DICTRA models with a cooling rate of $-10^3, -10^4,$ and $-10^5$ K/s. Experimentally measured solidification crack length data [101-103] is overlaid on a second axis to compare with the trend in SCS predicted by DICTRA using the model proposed by Kou et al. [81, 82]. Model results are plotted using a five-point moving average to smooth out the numerical error associated with calculating the derivative at higher copper content.

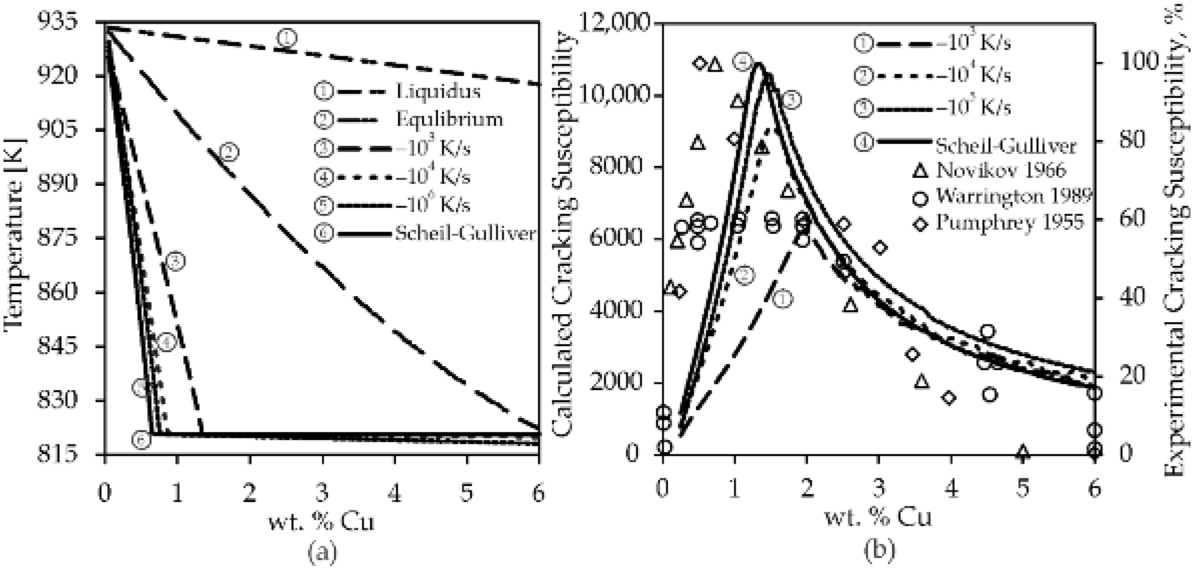

**Figure 2 – Modeling the impact of cooling rate of solidus temperature and solidification cracking susceptibility of Al-Cu alloys.(a) Modeling the effect of cooling rate on the solidus temperature of Al-Cu alloys using the equilibrium, Scheil, and one-dimensional DICTRA solidification models under different cooling rates. (b) Solidification cracking susceptibility of Al-Cu alloys calculated by the DICTRA and Scheil models coupled with the Kou criteria for solidification cracking susceptibility with experimental cracking susceptibility data [101-103].**

### 2.1.4 Predicting Thermal History During the LPBF Process

The LPBF process model used in this work to predict the temperature history during printing of SS316L consisted of a single layer 1080µm square with a bidirectional raster scanning pattern and a 90µm hatch spacing. The material properties were taken at 700 K by performing a linear interpolation of the properties given by Khairallah and Anderson *et. al* [104], yielding a density of 7.9g/(cm$^3$), thermal conductivity of 20.2 W/(m·K), and specific heat of 470 J/(kg·K). This temperature was chosen as previous results have shown that the melt pool dimensions in SS316L are more accurate when modeled using material properties from this elevated temperature range. The model was run with a selection of laser velocities, 0.8-1.2 m/s varying by 0.2 m/s, and laser powers 170-190W varying by 10W based on the optimal parameters proposed by Yan et al. [105]. A range of processing parameters was investigated to determine if the CALPHAD-based ICME framework can predict the effect of processing conditions on non-equilibrium solidification. The results were then inspected to determine which locations may be of interest to the microstructural model. These points were chosen to give a broad representation of thermal histories produced by the model. Three subsets of points were selected; the first were points from a cross section of the melt pool to capture dependence on relative location. Second, points were selected that melted more than once. Lastly, points were selected with higher and lower than average cooling rates. These points were down selected to three points; one which rapidly remelted, one at the center of the path, and one between subsequent passes. This down-selection was carried out to avoid convergence issues with the DICTRA model for certain cooling curves. **Figure 3** shows the development of the thermal field as the laser moves through the bidirectional raster scanning pattern. The white X's shown in **Figure 3** mark the location of temperature histories used as inputs to the CALPHAD-based ICME framework.

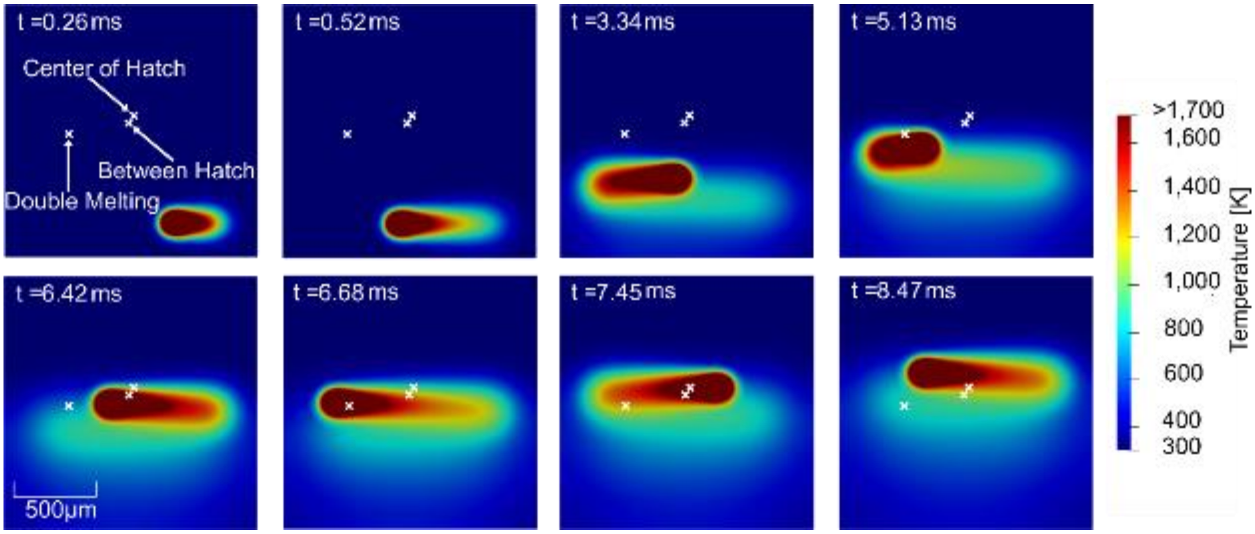

**Figure 3 – Heat map of the thermal history of SS316L manufactured by LPBF predicted by the model developed by Wolfer et al. [98]**Temperature histories taken from the locations marked in **Figure 3** are shown as a function of time in **Figure 4**. The location that undergoes rapid double melting was screened for by finding the location where the liquidus temperature is reached consecutively in the shortest period. Rapid double melting was investigated to determine if the non-equilibrium DICTRA solidification model is affected. The inset plot shown in **Figure 4** highlights the rapid double melting cycle. One feature of the thermal histories that is worth addressing is the high peak temperatures predicted at the point of incidence of the laser during melting. Because the thermal model uses a conduction-only approach (combined with calibrated effective transport parameters) to capture multiple heat transfer mechanisms, it produces peak melt temperatures that are beyond what is expected. However, because the model was calibrated using high-fidelity numerical simulations by comparison of the melt pool geometry, it is hypothesized that the accuracy of the predicted thermal field outside of the melt pool would be reasonable. Since the boundary of the melt pool is constrained to the melting temperature, it is analogous to a Dirichlet boundary condition, and the thermal field calculated inside the melt pool can be ignored as it has

no effect on the overall thermal field. This hypothesis was verified by comparing the isotherms predicted by the thermal model with those obtained by high-fidelity numerical simulations [100].

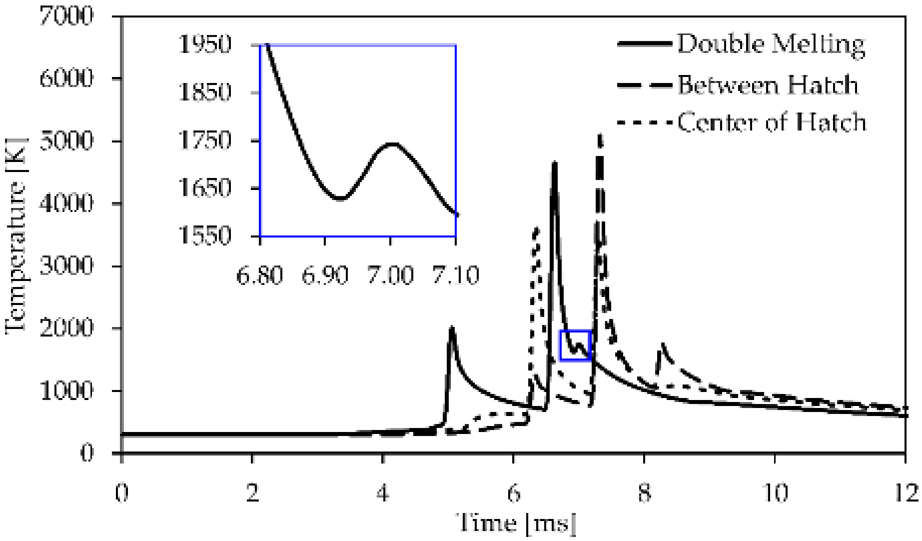

**Figure 4 – Thermal history of additively manufactured SS316L generated using the LPBF process model developed by Wolfer et al.[98] at a location between the hatch lines, in the center a hatch line, and at a location that undergoes rapid double melting. The inset figure is taken from the area marked by the blue square to highlight the rapid double melting seen at various locations in the model.**

### 2.1.5 Solidification of SS316L During Additive Manufacturing

Non-equilibrium solidification of SS316L is modeled using the CALPHAD-based ICME framework shown in **Figure 1** to test the convergence of DICTRA models under different temperature histories and investigate the effect of processing conditions on non-equilibrium solidification. A six-component system, consisting of Fe66.985-Cr17-Ni12-Mn1.5-Mo2.5-C0.015 in weight percent, is considered using the TCFE10 and MOBAL5 databases available in the 2020b release of Thermo-Calc software. The effects of nucleation barriers are neglected, and a constant cell size of 10 nm with planar geometry is used for all calculations. Temperature histories generated from the LPBF process model for various processing conditions and locations throughout a single layer build are used as inputs to the DICTRA solidification model. Figure 5 shows the results of a representative DICTRA simulation from a location in the LPBF process model that undergoes multiple remelting cycles. The temperature history is directly used from the LPBF process model as shown in **Figure 5(a)**. Cutoff temperatures, defined as the solidus and liquidus, are used to select only the portion of the temperature history that relates to solidification. This minimizes the computational expense of each model and enables high-throughput calculations by only modeling phase transformations during solidification. The phase fraction of BCC and FCC as a function of temperature predicted by DICTRA deviates significantly from the Scheil-Gulliver prediction as shown in **Figure 5(b)**. Thus, the effect of back-diffusion is significant in SS316L at the high cooling rates seen in AM processes. During the second solidification cycle, the phase fraction of BCC and FCC moves closer to the Scheil-Gulliver prediction, indicating that multiple remelting cycles cause solidification to deviate further from equilibrium if segregation in the liquid is not given enough time to homogenize. **Figure 5(c)** shows the phase fraction as a function of time predicted by DICTRA and highlights the rapid solidification and remelting that occurs because of the temperature history shown in **Figure 5(a)**. The plot of temperature versus the total solid fraction shown in **Figure 5(d)** shows reasonable agreement between the Scheil-Gulliver and DICTRA prediction.

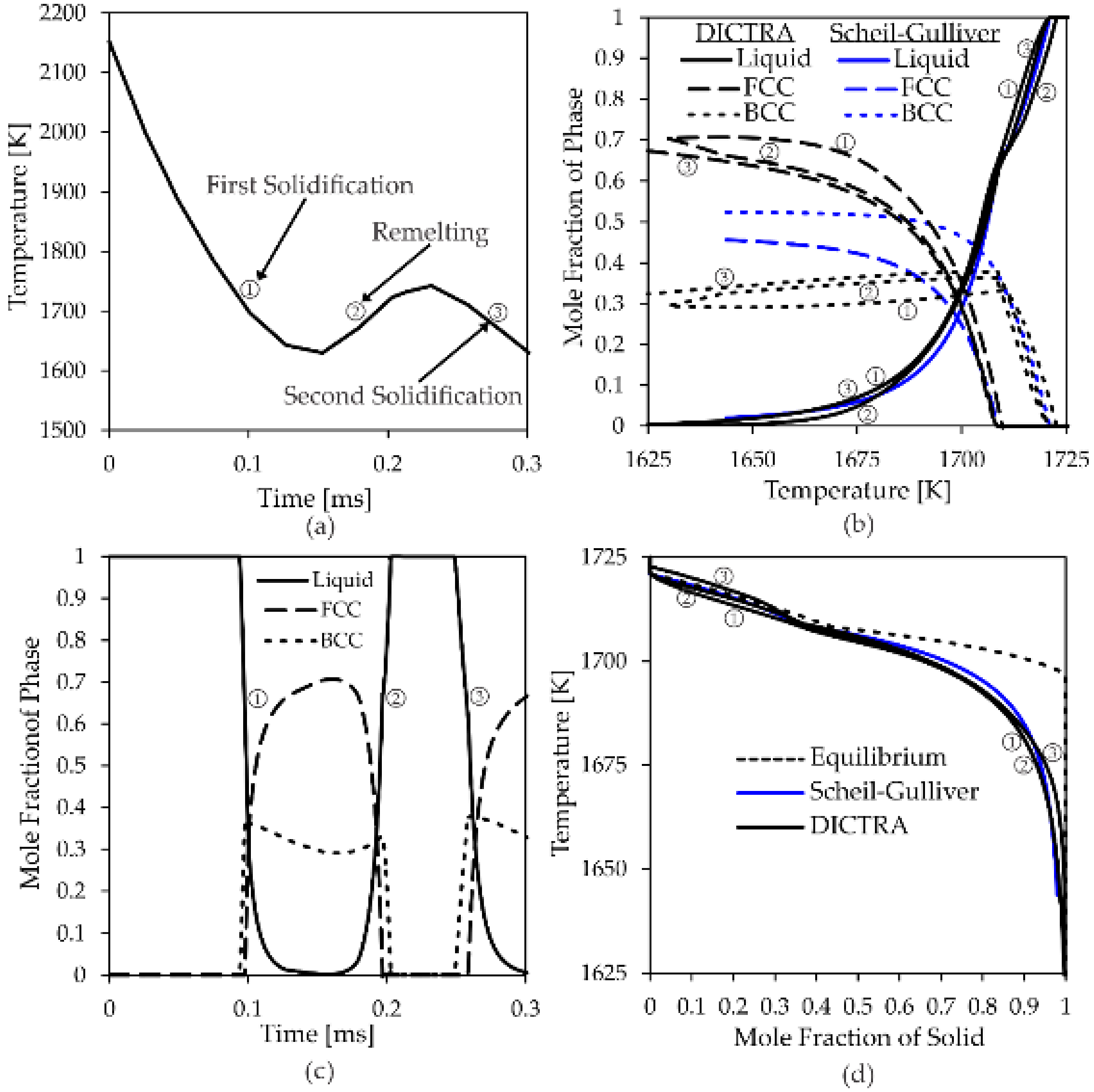

**Figure 5 – Non-equilibrium solidification modeling of SS316L undergoing rapid double melting.(1) corresponds to the first solidification transformation, (2) refers to remelting, and (3) marks the second solidification transformation. (a) Temperature history with rapid double melting directly used as an input to the DICTRA model. (b) Mole fraction of each phase as a function of temperature predicted using the DICTRA and Scheil-Gulliver models. (c) Mole fraction of each phase as a function of time modeled using DICTRA. (d) Temperature versus the mole fraction of solid as predicted by the equilibrium, Scheil-Gulliver, and DICTRA models for solidification.**

**Figure 6** shows the results of the Kou SCS model applied to DICTRA solidification calculations for SS316L as a function of GED. A linear relationship is observed between SCS, and the GED used in the LPBF process model. Considering the inherent numerical error associated with DICTRA, the relationship between the Kou SCS model prediction and GED is significant. The correlation between GED and SCS is related to changes in the cooling rate during solidification. Temperature histories generated by the LPBF process model under processing conditions with lower GED yielded faster cooling rates and higher SCS. No significant difference in the Kou SCS model is found based on the location the temperature history is taken from. Some calculations resulted in convergence issues and could not be resolved. However, convergence was achieved in most temperature histories tested in this work.

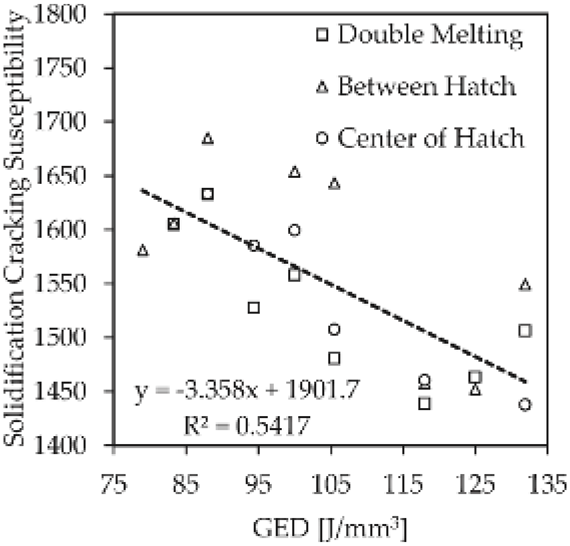

**Figure 6 – SCS of SS316L as a function of GED calculated by DICTRA using the SCS model proposed by Kou.The trend line considers the temperature history from all three locations shown in Figure 3.**

### 2.1.6 Discussion of Integrated Processing and Microstructure Models for Non-Equilibrium Solidification

Non-equilibrium solidification of Al-Cu alloys is used as a case study to demonstrate the ability of DICTRA to correlate changes in the cooling rate with SCS as a function of composition. In general, the trend in SCS predicted by the Scheil-Gulliver and DICTRA models is consistent with experimental solidification crack length measurements. The peak in SCS predicted by the Scheil-Gulliver and DICTRA models occurs at slightly higher Cu content than the experimentally observed peak reported by Novikov et al. [24] However, the characteristic lambda shape commonly observed in SCS measurements of binary aluminum alloys [7] matches well with the experimental data as shown in **Figure 2(b)**. It is also observed that increasing the cooling rate during solidification pushes the solidification reaction further from equilibrium which reduces the solidus temperature, increases microsegregation, and leads to increased SCS. The experimentally observed trend in SCS is reproduced by the model, demonstrating its ability to correlate process-level variables with microstructural effects. Intuitively, the model also predicts a reduction in the SCS with a decrease in the cooling rate.

The linear relationship between GED and SCS predicted for SS316L made by LPBF demonstrates the value of coupling process models with microstructure level CALPHAD models. Increasing the GED decreases the cooling rate because a larger amount of thermal energy is applied to the material, thus taking a longer time to cool. Reductions in the cooling rate led to a reduced SCS at higher GED. Future work may be able to correlate changes in scanning strategy with SCS, microsegregation, and phase fraction using high-throughput DICTRA calculations by investigating the effect of temperature histories at various locations throughout a single layer build. No trends in SCS based on the location in the LPBF process model were found. However, switching to a material with higher SCS, such as Ti-6Al-4V or Al-Cu, may reveal spatial dependence.

Non-equilibrium solidification is an important metallurgical phenomenon to consider in materials design for AM. Optimization of new alloys should focus on controlling solidification during the AM process to obtain improved properties in the as-built condition. Models for predicting microsegregation, SCS, and phase transformations in AM materials as a function of processing parameters and composition are limited and the potential for impact in the field is apparent. The CALPHAD-based ICME framework proposed in this work attempts to address the disconnect between macroscale processing effects and microstructure level models for solidification. This work falls short of defining a quantitative process-structure relationship but demonstrates that modern materials models can predict qualitative relationships in AM processes.

Improvement of the numerical solver within DICTRA is needed to realize the full potential of the CALPHAD-based ICME framework developed in this work. Convergence issues with DICTRA affected about half of the temperature histories tested in this work and limited the ability to use DICTRA in high-throughput calculations. This work also highlights the importance of reliable thermodynamic and mobility assessments of critical materials systems. Improvement of thermodynamic and mobility databases will directly improve the ability of the CALPHAD approach to design the next-generation of AM materials.

## 2.2 Prediction of Location-Specific Solidification Cracking Susceptibility

Content from the following open access journal paper is used in this section:

- S. Sridar, N. Sargent, X. Wang, M.A. Klecka, W. Xiong, Determination of Location-Specific Solidification Cracking Susceptibility for a Mixed Dissimilar Alloy Processed by Wire-Arc Additive Manufacturing, Metals 12(2) (2022), doi:10.3390/met12020284.

This section employs a CALPHAD-based ICME approach to investigate location-specific solidification cracking susceptibility in a graded alloy composed of P91 steel and Inconel 740H superalloy produced using wire arc additive manufacturing (WAAM). Experimental and computational analysis revealed that the alloy mixture of 26 wt.% P91 steel with 74 wt.% Inconel 740H has the highest susceptibility of solidification cracking among the possible alloy mixtures. The microstructure of this alloy mixture consists of intergranular solidification cracks that progressively lengthen along the build height. Using an integrated experimental and computational approach, the ability to predict location-specific solidification cacking susceptibility is demonstrated for the first time. DICTRA solidification modeling, the Kou criterion [81, 82] for solidification cracking susceptibility, and back calculated cooling rates generated from experimental measurements of the secondary dendrite spacing are coupled together to reproduce the location specific solidification cracking susceptibility observed experimentally. The top region, characterized by the highest cooling rate, exhibits the greatest susceptibility to solidification cracking, which aligns well with the observed crack length in experimental findings. This research contributes to the evaluation of solidification cracking susceptibility in FGMs using a CALPHAD-based ICME approach and demonstrates the synergy of combining experimental and computational techniques. Although the WAAM process is not the primary manufacturing technique investigated in this thesis, the modeling approach applied in the section is universally applicable to other AM processes.

**Figure 7** shows the solidification cracking susceptibility calculated using the Kou criterion and the solidification range for the alloy mixtures of P91 steel and Inconel 740H. According to the Kou criteria, the highest SCS occurs at 26 wt.% P91. This finding was experimentally validated after a large build of 26 wt.% P91 steel, originally thought to be a suitable interlayer material for joining P91 steel and Inconel 740H, was found to be full of large cracks formed between columnar grains oriented in the build direction. **Figure 8** shows a cross section of the as-built 26 wt.% P91 steel mixture with three SEM images of progressively larger solidification cracks forming along the build direction. For brevity, the experimental methods used to manufacture the samples studied in this work are not included because this chapter focuses on the microstructure of modeling FGMs. Interested readers are suggested to read the full open-access publication for more details [42].

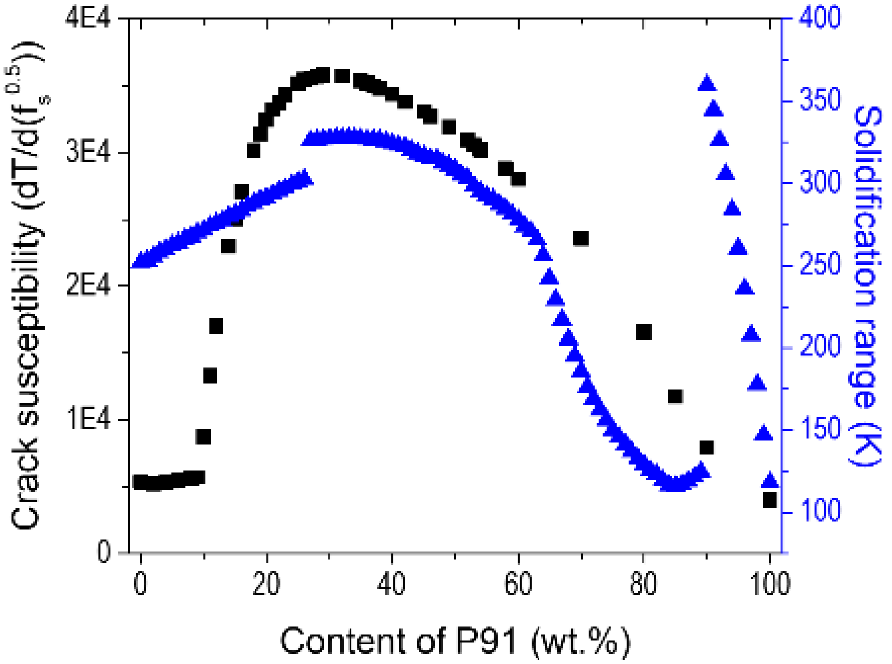

**Figure 7 – Overall solidification cracking susceptibility determined using Kou criterion and freezing range calculated using Scheil simulations for different mixed compositions between P91 steel and 740H superalloy.**

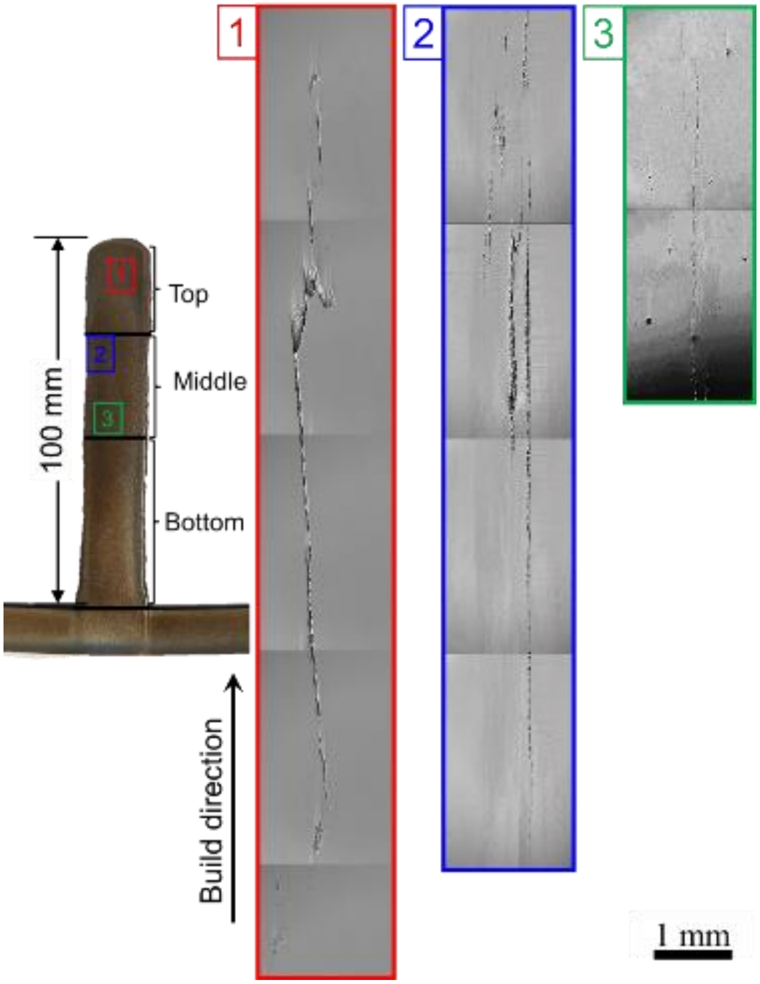

**Figure 8 – Secondary electron SEM micrographs showing cracks of varying length from various locations of the 26 wt.% P91 steel mixture along the build direction.**

To assess the susceptibility of solidification cracking at specific locations in the 26 wt.% P91 steel mixture processed by WAAM, the Kou criterion is used in conjunction with DICTRA simulations. Using DICTRA allows the effects of back diffusion during solidification to be considered but requires prior knowledge of the solidification pathway, secondary dendrite arm spacing and cooling rate. To collect the additional information required for the DICTRA solidification model, the etched microstructure of the 26 wt.% P91 steel mixture was used to measure the secondary dendrite arm spacing (SDAS) at various locations along the build direction. **Figure 9(a)** shows a representative image of the etched microstructure used to measure the SDAS.

The average cooling rate was then back calculated using the empirical relationship between SDAS and average cooling rate for Inconel 625 developed by Tinoco *et al.*:

$$\lambda = 58.02R^{-0.31} \tag{2-3}$$

where $\lambda$ is the experimentally measured SDAS and R is the average cooling rate. Although this equation was originally developed for IN625, it can be qualitatively used for other superalloys with similar compositions. The measured SDAS based on the etched micrographs and the average cooling rate back calculated from the SDAS are shown in **Figure 9(b-c)**. A negative correlation between SDAS and cooling rate is observed. The back calculated cooling rates and SDAS values were then used as inputs for DICTRA solidification calculations.

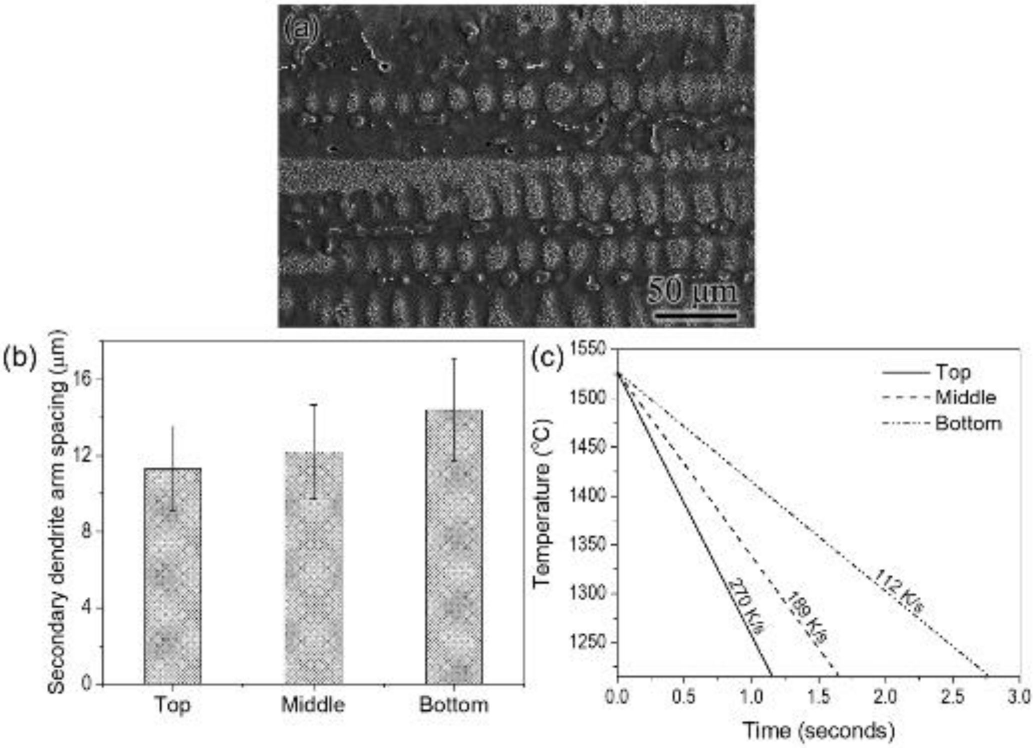

**Figure 9 – Back calculating the average cooling rate from SDAS measurements.(a) SE-SEM micrograph showing the etched microstructure from the top portion of the sample with the secondary dendrites. (b) SDAS calculated from the etched microstructure and (c) Average cooling rates calculated using the SDAS from various locations of the sample.**

**Figure 10** It is noteworthy that the solidus temperature exhibits significant variation depending on the calculation method, primarily due to the different assumed cooling rates. The equilibrium calculation assumes the slowest cooling rate, allowing for complete diffusion in both solid and liquid phases during solidification. Consequently, it results in the highest solidus temperature among the different calculation methods. On the other hand, the Scheil model assumes a faster cooling rate, considering complete diffusion in the liquid phase and negligible diffusion in the solid phase, leading to the lowest solidus temperature. The solidus temperatures calculated using one-dimensional DICTRA simulations fall between the equilibrium and Scheil calculations since the assumed cooling rate is intermediate. Furthermore, it is observed that the solidus temperature increases from the top to the bottom sections of the sample, corresponding to an increase in the cooling rate.

**Figure 10(b)** displays the solidification cracking susceptibility, determined based on the maximum slope of the temperature vs. fraction of solid curve ($dT/df_s^{0.5}$) obtained through DICTRA simulations using the Kou criterion, from various locations within the sample. The top portion of the sample, experiencing the highest cooling rate, exhibits the highest cracking susceptibility. Conversely, the middle and bottom portions of the sample display decreased cracking susceptibility as the cooling rate decreased. These findings align well with the observed cracking behavior in different sections of the sample, as depicted in **Figure 8**.

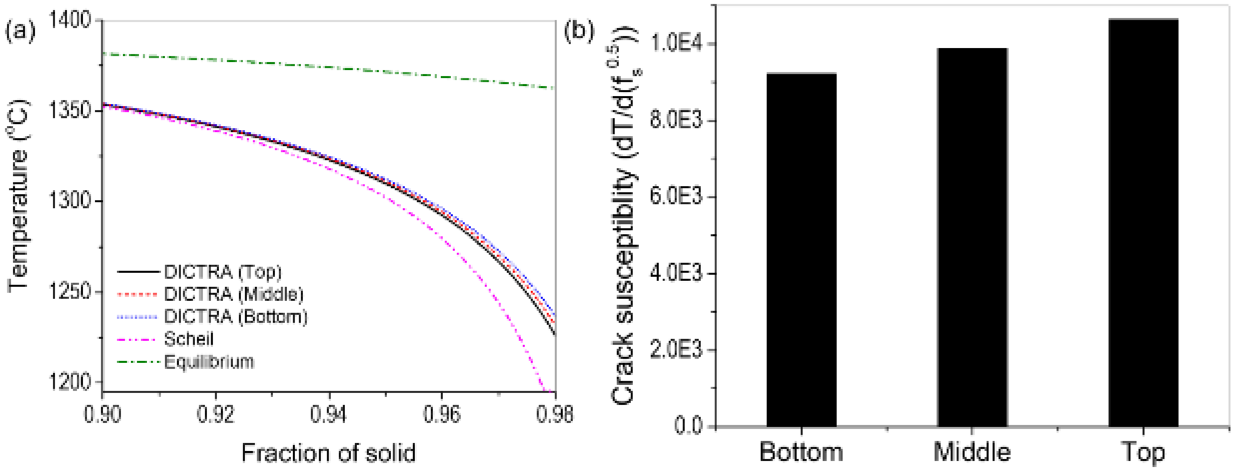

**Figure 10 – Prediction of location specific solidification cracking susceptibility for 26 wt.% P91 steel mixture.(a) Temperature vs. fraction of solid curves obtained using equilibrium, DICTRA and Scheil calculations at the end of solidification showing the difference in solidus temperatures at ~98% solid fraction and (b) solidification cracking susceptibility calculated from different locations of the sample using the Kou criterion coupled with DICTRA calculations.**

Temperature histories during WAAM vary significantly depending on the location in a build, causing significant location-specific variations in the as-built microstructure. In the case of the alloy mixture of 26 wt.% P91 steel and 74 wt.% Inconel 740H processed by WAAM, the average cooling rate became faster as the build height increased, as shown by the gradual decrease in the SDAS with increasing build height. Taking the average cooling rate and SDAS determined from experiments as inputs for DICTRA solidification modeling enables the location-specific cracking behavior to be described using Kou criteria for solidification cracking susceptibility. This work presents a novel integrated computational and experimental approach for understanding the location-specific solidification cracking susceptibility of multicomponent alloy mixtures encountered when manufacturing FGMs.

## 2.3 Diffusion Coupled Functionally Graded Materials: An Approach for Modeling Diffusion in Complex Composition Gradients

The compositional instability of FGMs is best described by invoking the second law of thermodynamics which states that the entropy of an isolated system will tend to increase over time in the absence of external intervention. If we consider an FGM to be an isolated system, it follows that over time, entropy (disorder) will increase and eventually result in the homogenization of the composition gradient. Predicting diffusion in FGMs over time under isothermal conditions will be important for predicting the lifetime and heat treatability of multi-material parts. To address the inherent compositional instability of FGMs, this chapter proposes the concept of diffusion coupled FGMs for modeling the diffusion of complex composition gradients. The inspiration for this modeling approach is drawn from the kinetic modeling of diffusion couples, hence the name diffusion coupled FGMs.

Fick's second law of diffusion, derived from Fick's first law and the continuity equation [106], governs the kinetics of FGMs:

$$\frac{\partial C}{\partial t} = D\frac{\partial^2 C}{\partial x^2} \tag{2-4}$$

where $\frac{\partial C}{\partial t}$ is the change in concentration with respect to time, $D$ [m$^2$s$^{-1}$] is the diffusion coefficient and $\frac{\partial^2 C}{\partial x^2}$ is the curvature of the composition gradient. Ficks' laws can be solved for multicomponent alloys systems by solving partial differential equations and applying the finite element method, given that there is a proper thermodynamic and kinetic database available. Software for solving one-dimensional isothermal diffusion couple problems is mature and available in both commercial (DICTRA) [75] and open source (Kawin) [74] forms. Although FGMs operating at any temperature are unstable, FGMs operating at high-temperature require careful consideration due to increased diffusivity. The temperature dependent diffusivity of a species $k$ is simply described by the Arrhenius equation:

$$D_k = D_k^0 \exp\left(-\frac{Q_k}{RT}\right) \tag{2-5}$$

where $R$ is the gas constant [8.314 J mol$^{-1}$], $Q_k$ [J mol$^{-1}$] is the activation energy, $D_k^0$[m$^2$s$^{-1}$] is the frequency factor, and $T$ is the temperature in Kelvin. Modeling of multicomponent diffusion also requires the consideration of interdiffusion coefficients because the diffusivity of a given species $k$ depends on both its own composition gradient and that of the other species in the alloy. This effect was famously described by Darken's experiment [66], where two steels of similar carbon content but different amounts of silicon were welded together and then heat treated. During heat-treatment, the carbon diffused towards the steel with lower silicon content despite the uniform composition of carbon across the joint. Darken's experiment clearly demonstrated that the driving force for diffusion is the chemical potential gradient across a material interface, which is influenced by the composition gradient of all the elements in a system. Diffusion within FGMs is driven by gradients in chemical potential as described in Darken's experiment.

Diffusion couples have been the subject of extensive scientific interest over the past few decades [11, 69, 107] and there are established theories for predicting the diffusion paths of binary and ternary diffusion couples [68]. The established rules for predicting diffusion pathways in diffusion couples can be applied to FGMs. Although the rules that govern diffusion pathways in diffusion couples have been established for several decades, this thesis represents the first acknowledgement of their application to FGMs made by AM. Drawing on the laws of diffusion and the established fundamental research on modeling diffusion couples, this chapter proposes the concept of diffusion coupled FGMs for predicting diffusion in complex composition gradients.

The concept of diffusion coupled FGMs requires two major assumptions. First, the interfaces between alloys are treated as sharp compositional changes, fundamentally we are ignoring dilution from the AM process and treating each interface as an ideal diffusion couple. If experimental measurements or estimates of dilution between subsequently deposited alloys are available, this information can also serve as the initial condition for the model. Second, each alloy interface is decoupled from each other and treated as an individual diffusion couple. This simplification means each interface (diffusion couple) can be modeled using a different thermodynamic and kinetic database tailored for the given alloy system. These two assumptions simplify an FGM into a series of diffusion couples stacked on top of each other, creating several one-dimensional isothermal diffusion problems that can be solved individually using the different thermodynamic and mobility databases. Simplifying FGMs into a series of diffusion couples creates a simplified modeling framework for predicting the lifetime of multi-material parts, making the qualification of complex FGMs operating at elevated temperatures feasible.

There are multiple benefits to diffusion coupled FGMs, but there are still situations where continuous gradients between materials are beneficial, such as limiting the effect of thermal expansion differences. However, diffusion coupled FGMs simplify multi-materials joints by limiting the number of different alloys deposited during printing. This simplification allows each deposited alloy to be qualified as an individual material. Also, the interfaces between each alloy can be qualified in an equivalent way to dissimilar welds. I believe the approach of modeling FGMs as a series of individual diffusion couples will increase the technology readiness level of complex multi-material joints by simplifying a complex problem into something that is predictable and can be qualified under industry standards.

To demonstrate the diffusion coupled FGM modeling approach, a SS316L and Titanium-6Al-4V (Ti-6Al-4V) FGM joined by several interlayers is taken as an example. Joining steel and titanium is challenging because Fe-Ti intermetallic compounds with poor mechanical properties easily form at the interface between iron and titanium-based alloys [8]. **Figure 11** shows the binary Fe-Ti phase diagram containing the brittle intermetallic compounds $Fe_2Ti$ and FeTi, demonstrating the need for an interlayer alloy for separating steel and titanium alloys. There have been numerous attempts to join SS316L and Ti-6Al-4V. Researchers have proposed copper [6] and the Ni-Cr-V ternary system [46, 63] as potential interlayers for separating SS316L and Ti-6Al-4V. Explosive welding has successfully produced steel and titanium joints [7]. However, explosively welded steel and titanium joints cannot be heat treated or operate at elevated temperature without forming Fe-Ti intermetallic phases. These previous attempts have based their designs solely on thermodynamic equilibrium calculations and have not considered any kinetic factors.

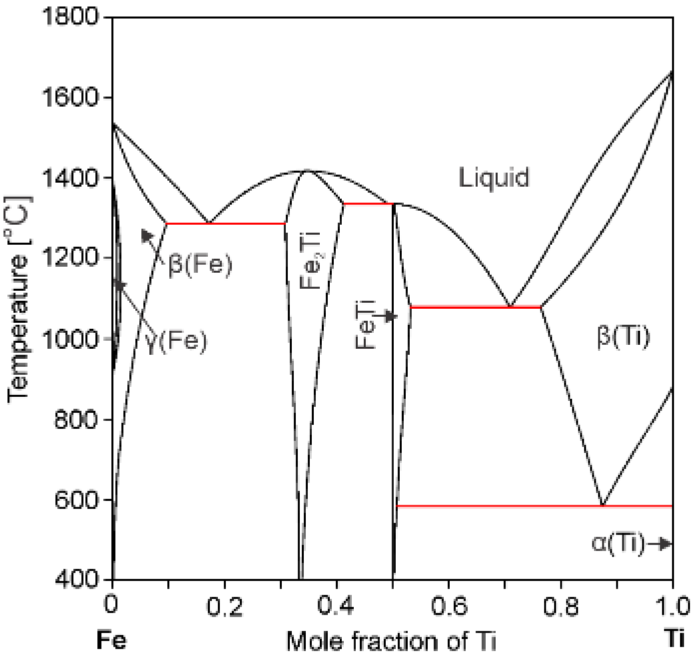

**Figure 11 – Fe-Ti binary phase diagram calculated using Thermo-Calc software version 2022b with TCFE12 database.**

Joining titanium and steel has significant commercial relevance in aerospace applications. While visiting NASA JPL (Jet Propulsion Laboratory) during the summer of 2022, there was interest in developing a stainless steel and titanium joint with a Ni-Cr-V interlayer for an application on the Mars sample return lander. Previous attempts to manufacture a joint between steel and titanium using the Ni-Cr-V ternary system as an interlayer have shown promise [46, 63]. However, these attempts failed to produce samples suitable for space flight applications. This motivated a thorough analysis of the kinetics and mechanical properties of Ni-Cr-V interlayers for joining Steel with Titanium.

The idea for using the Ni-Cr-V ternary system as an interlayer was conceived by other researchers through investigating binary phase diagrams containing either Fe or Ti that form single phase solid solutions phases across the entire composition space at elevated temperature [3]. This logic led to the hypothesis that steel could be joined to nickel, nickel could then be joined to chromium, chromium could be joined to vanadium, and finally vanadium could be joined to titanium. Taking a roundabout pathway through the Ni-Cr-V ternary is necessary to avoid the sigma phase which forms in binary Ni-V phase diagram and extends into the Ni-Cr-V ternary phase diagram [46]. **Figure 12** shows a 900°C isothermal section of the Ni-Cr-V ternary phase diagram with the proposed roundabout pathway [3] that avoids the sigma phase and separates steel and titanium alloys to avoid Fe-Ti intermetallic phases. The 900°C isothermal section is presented in **Figure 12** because the typical heat treatment temperature of Ti-6Al-4V is 900°C and therefore is representative of the quenched in microstructure after heat treatment.

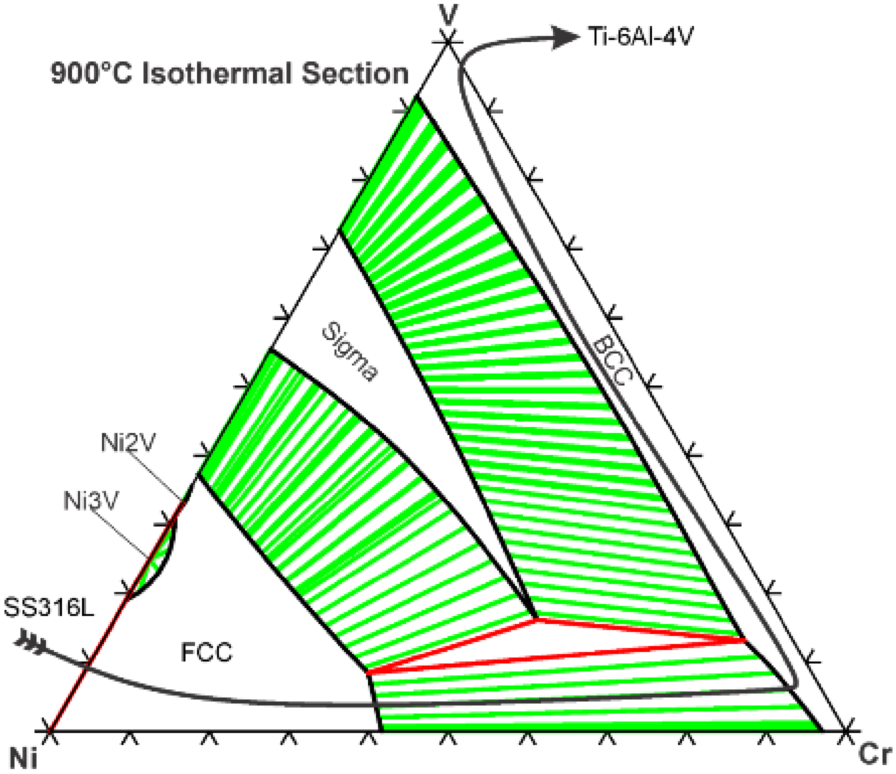

**Figure 12 – 900°C isothermal section of the Ni-Cr-V ternary phase diagram.The roundabout pathway to avoid the sigma phase through the Ni-Cr-V ternary diagram is marked. Calculated with Thermo-Calc software using the thermodynamic assessment by Choi et al. [108].**

There is not a comprehensive thermodynamic and kinetic database capable of covering the steel, titanium, and Ni-Cr-V ternary composition space. Therefore, a stainless steel and titanium joint with a Ni-Cr-V interlayer must be decoupled into several individual diffusion couples so that the appropriate database can be applied. **Figure 13** shows a schematic of the proposed design for a diffusion coupled FGM combining SS316L and Ti-6Al-4V through the Ni-Cr-V ternary. The FGM is split into four diffusion couples modeled using three different pairs of thermodynamic and kinetic databases. The commercial steel and iron databases available in Thermo-Calc software version 2022b are used for the diffusion couple one and four, respectively. Diffusion couple two and three are modeled using the thermodynamic assessment of the Co-Cr-Fe-Ni-V by Choi et al. [108] and several mobility databases [109-113] were combined to create a comprehensive FCC and BCC mobility assessment for the Ni-Cr-V ternary system. Using three different combinations of thermodynamic and kinetic databases, the diffusion pathways of the four diffusion couples shown in **Figure 13** were modeled using DICTRA.

One-dimensional 900°C isothermal diffusion problems were solved for each of the four diffusion couples to simulate the standard heat treatment of Ti-6Al-4V and predict the resulting diffusion pathway. Diffusion couples one and four were modeled as single-phase diffusion couples containing FCC and BCC, respectively. Two phase FCC and BCC diffusion with FCC set as the matrix phase was used to model diffusion couples two and three. The homogenization model [114] implemented within DICTRA and cross validated with the open-source diffusion modeling software Kawin.

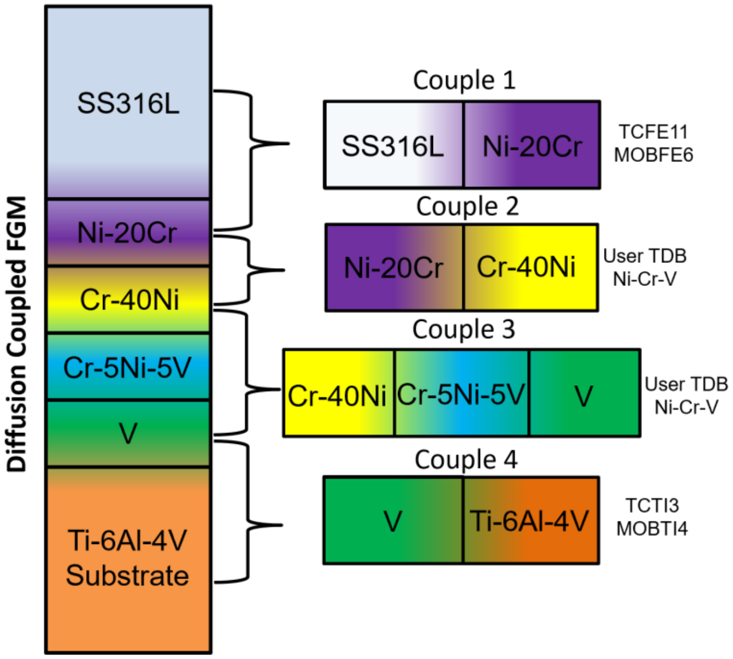

**Figure 13 – Schematic of additively manufactured stainless steel to titanium diffusion coupled functionally graded material (FGM).Decoupling the complex compositional pathway into discrete blocks enables the use of kinetic models for predicting diffusion during heat treatment and elevated operating temperatures. This schematic illustrates a new methodology for designing FGMs that can be qualified for space flight applications.**

The results of the four one-dimensional 900°C isothermal diffusion problems are superimposed onto a series of ternary 900°C isothermal sections to visualize the diffusion pathway at each of the interfaces between composition blocks as shown in **Figure 14**. The simulated diffusion pathway within the FGM does not cross into regions of detrimental phase stability (Sigma phase) during heat treatment at 900°C for one hour. This methodology can be applied to other FGMs to inform the selection of interlayer materials by predicting the diffusion pathway. Although visualization of diffusion pathways containing more than three elements in two dimensional plots is challenging, this methodology can still be used to gain insight into the diffusion pathway in complex multicomponent alloys.

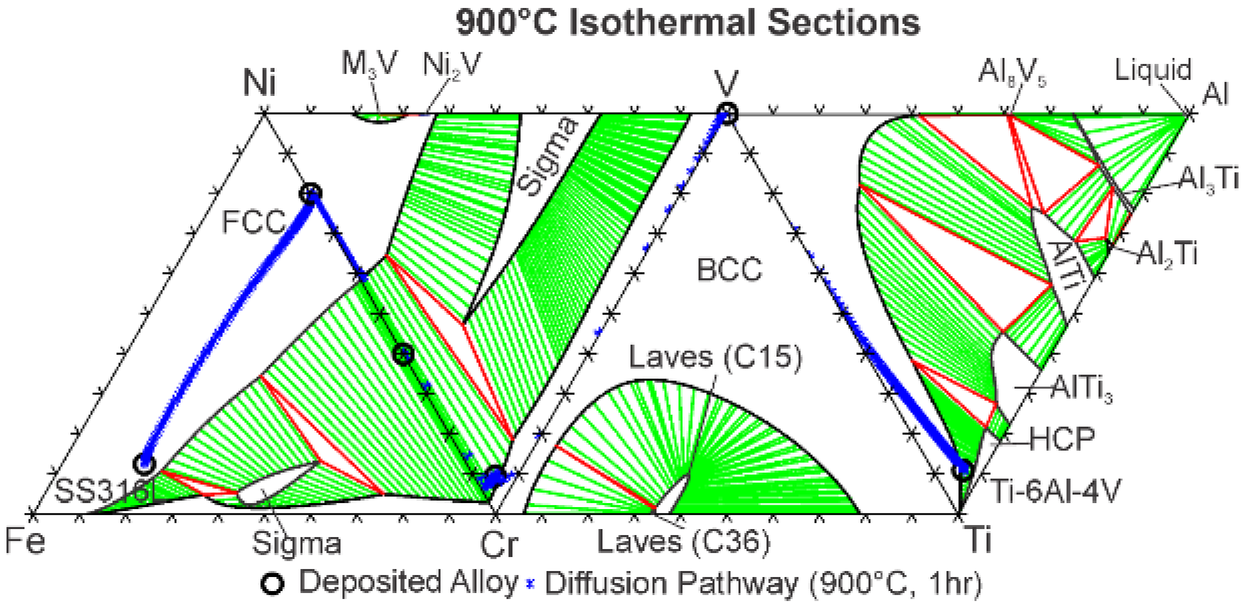

**Figure 14 – Ternary isothermal sections at 900°C showing the thermodynamic phase equilibria along the compositional pathway used to connect stainless steel to titanium.Kinetic modeling was used to predict the diffusion between the deposited alloys using DICTRA module within Thermo-Calc software. The SS316L and Ni-20Cr diffusion pathway is plotted by adding the trace elements (C, Mn, Mo & Si) to Fe for visualization purposes.**

The results of the kinetic modeling presented in **Figure 14** show that diffusion between dissimilar materials is not trivial. Assuming diffusion occurs uniformly down the composition gradient is always false in multicomponent alloy systems. Differences in the chemical potential across alloy interfaces result in complex diffusion pathways which must be considered when designing FGMs. An example of a non-trivial diffusion pathway in this system is the SS316L and Ni-20Cr diffusion couple, shown by the curvature of the diffusion pathway within the Fe-Ni-Cr 900°C isothermal section in **Figure 14**. By considering the effects of kinetics and thermodynamics using the concept of diffusion coupled FGMs, a more comprehensive computational design methodology has been developed for predicting the behavior of FGMs.

Decoupling of FGMs into discrete compositions blocks using the concept of diffusion coupled FGMs simplifies both the modeling and manufacturing process. Forgoing a continuous gradient between two alloys in favor of a sharp transition results in the deposition of fewer materials during printing. Ideally this simplification results in fewer complications when optimizing processing parameters while also streamlining the qualification process. Additionally, the modeling process is also simplified because a few simple thermodynamic calculations can be used to represent the phase stability throughout the diffusion coupled FGM. Scheil solidification calculations shown in **Figure 15** provide insight into the as-built microstructure while the phase fraction in thermodynamic equilibrium as a function of temperature is shown in **Figure 16.**

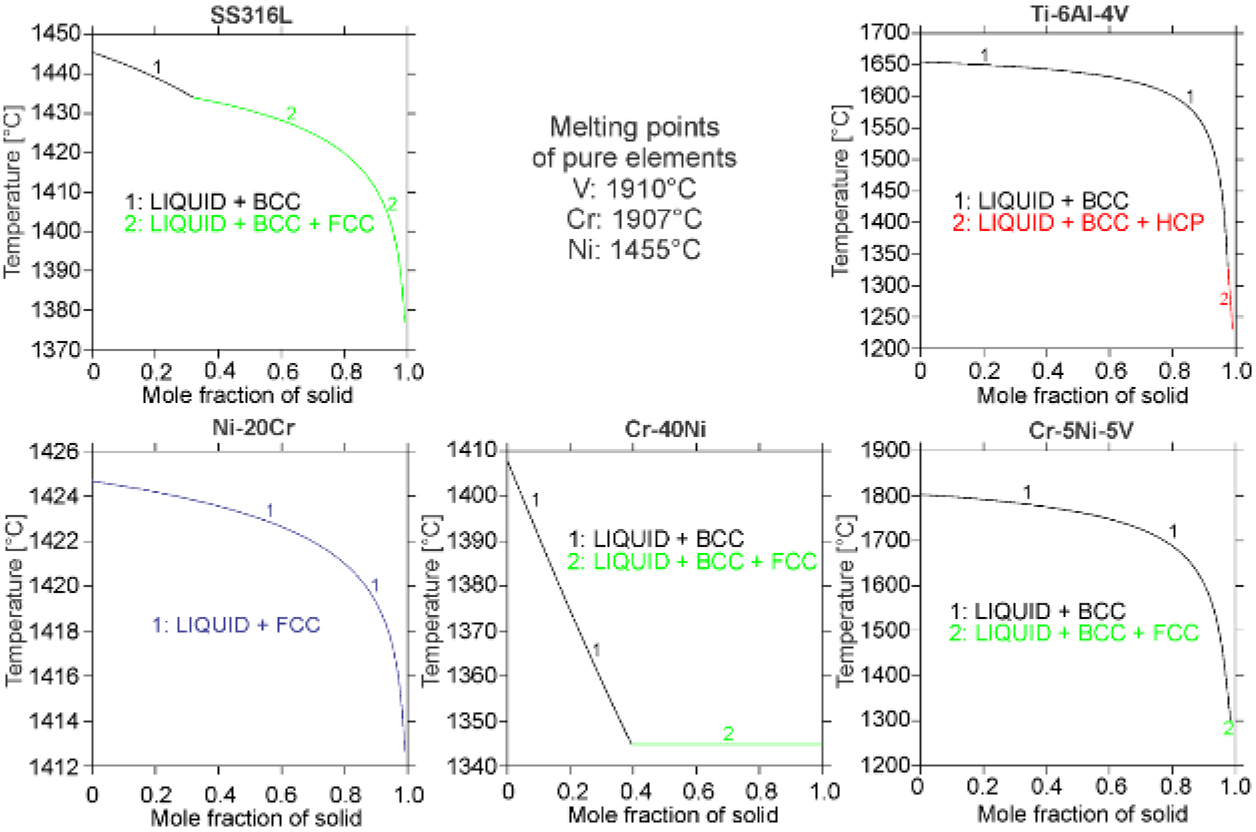

**Figure 15 – Scheil solidification modeling of the composition bocks making up the SS316L and Ti-6Al-4V diffusion coupled FGM.**

**Figure 15** presents the results of Scheil solidification modeling for the SS316L and Ti-6Al 4V FGM joined using a Ni-Cr-V interlayer. The results of the Scheil model show that Sigma phase is not predicted to form during rapid solidification. However, the solidification range of both the Ti-6Al-4V and Cr-5Ni-5V alloy is predicted to be larger than 400°C. Although Ti-6Al-4V is known to be a printable alloy, the large solidification range of the Cr-5Ni-5V alloy is concerning given that most Cr alloys are known to have poor mechanical properties at room temperature [115].

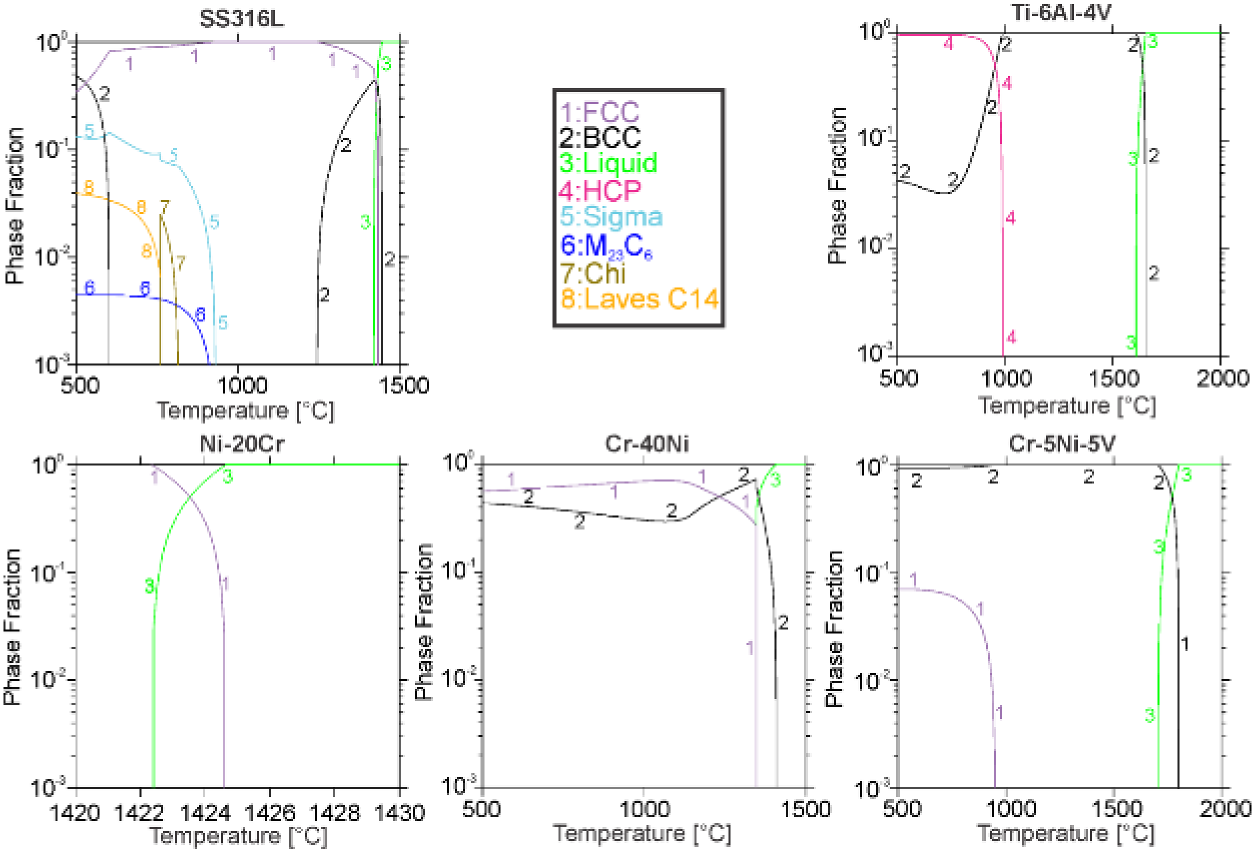

**Figure 16 – Prediction of the thermodynamic equilibrium phase fraction as a function of temperature for the composition bocks making up the SS316L and Ti-6Al-4V diffusion coupled FGM.**

Thermodynamic equilibrium predictions of the phase fraction as a function of temperature are presented in **Figure 16**. Except for SS316L, all alloys are expected to be sigma phase free at all temperatures. Although Sigma phase is thermodynamically stable in SS316L, the kinetics of its precipitation are sluggish and therefore only forms after prolonged high-temperature exposure. Among the other alloys, only FCC, BCC, and HCP phases are expected to form.

This section presents a novel modeling approach called diffusion coupled FGMs for conceptualizing and predicting the kinetic behavior of FGMs. Drawing inspiration from the foundational research on diffusion couples, this work applies proven methods for predicting isothermal diffusion pathways in binary/ternary diffusion couples to the complex multicomponent composition gradients contained within FGMs. The key development described in this section is that decoupling a complex composition gradient into discrete composition blocks with sharp composition boundaries creates a simplified kinetic modeling problem consisting of a series of stacked diffusion couples. With this approach, several databases can be used in combination to solve several simplified one-dimensional isothermal diffusion couple of problems. Combining the predicted diffusion pathways from each of these diffusion couples' pieces together a complete picture of effect of heat treatment and high-temperature exposure on the complex composition gradients within FGMs.

Although no experimental data is presented to validate the modeling approach presented in this section, the theoretical basis for diffusion coupled FGMs is rooted in the decades of research on diffusion couples. Future work will focus on developing new strategies for joining dissimilar multicomponent alloys that utilize the complex rules that govern binary and ternary diffusion couples. Although visualization of multicomponent diffusion pathways is a challenge, the available models for isothermal diffusion in metals can predict complex multicomponent diffusion pathways. In the coming years, the concept of diffusion coupled FGMs is expected to have a significant impact on multi-material components exposed to high-temperatures. Applications of the diffusion coupled FGMs include copper-superalloy bimetallic structures used in rocket engines and plasma facing multi-material structures in fusion reactors.

## 2.4 Chapter Summary & Conclusion

This chapter covers three novel advances in modeling the microstructure of AM materials and discusses their application to FGMs. In section 2.1, processing and microstructure models for non-equilibrium solidification are coupled together to predict the impact of processing parameters and changes in composition on the solidification cracking susceptibility of AM materials. In section 2.2 an integrated experimental and computational approach is used to demonstrate the ability to predict location-specific changes in solidification cracking susceptibility caused by variations in temperature history and composition. Finally, section 2.3 describes a framework for predicting the kinetic behavior of FGMs during heat treatment and high-temperature operation. The modeling concepts described in this chapter represent a contribution to the CALPHAD-based ICME design of FGMs.

# 3.0 Discovery of Microsegregation-Aided Transformation and Twinning-Induced Plasticity in Steel through Directed Energy Deposition of Functionally Graded Materials

In this chapter, functionally graded materials (FGMs) combining stainless steel 316L and high-strength low-alloy steel were manufactured using DED to discover new steel compositions for AM. High-throughput experiments using FGMs led to the discovery of a low-manganese (Mn<1 wt.%) TRIP (transformation-induced plasticity) and TWIP (twinning-induced plasticity) steel with a metastable microstructure enabled by non-equilibrium solidification. Microsegregation from non-equilibrium solidification caused heterogeneity in the phase stability and stacking fault energy, leading to TRIP and TWIP effects in the as-built condition without heat treatment. Tensile testing demonstrated the design of an as-built low-manganese TRIP and TWIP steel with an ultimate tensile strength of 960 MPa, total elongation of 26%, and a unique strain hardening rate that increases after yielding. We compare experimental measurements of microsegregation with thermodynamic modeling to discuss the impact of microsegregation on phase stability, stacking fault energy, and solidification cracking susceptibility in AM alloys. This work improves our understanding of FGMs and demonstrates a novel pathway for achieving TRIP and TWIP effects in AM alloys without heat treatment.

## 3.1 Chapter Introduction

FGMs [4, 29, 93] can be synthesized by DED process by controlling the volumetric flow rate of multiple feedstocks in successive layers along the build direction. This approach enables the creation of a one-piece component with spatially varying material properties. FGMs offer several advantages over conventional monolithic materials, including reduced part complexity and enhanced performance using location-specific material properties.

Manufacturing of FGMs is a promising field of research with applications in alloy design and advanced manufacturing. However, a significant gap remains in our understanding of the fundamental process-structure-property relationships that govern the formation of defects in dissimilar alloy systems. CALPHAD-based ICME (CALPHAD: Calculation of Phase Diagrams, ICME: Integrated Computational Materials Engineering) models [19, 88] have proven to be a valuable tool for screening composition gradients between two or more alloys for potential defects such as detrimental phases, solidification cracking, and differences in thermal expansion [21, 116-119]. Researchers at the NASA JPL have pioneered the modern manufacturing of FGMs using directed energy deposition (DED) and the application of CALPHAD tools in the design process [27, 46-48, 117, 118]. This work focused on combining two or more complementary materials to achieve location-specific properties that are unattainable using a monolithic alloy. Recent studies [13-15, 120] have further demonstrated the utility of using FGMs as a high-throughput tool for assessing novel alloy compositions at a reduced cost.

The laser-based AM process, with its inherent rapid heating and cooling rates, poses a challenge to the development of computational models for FGMs due to the non-equilibrium solidification that occurs [23]. Rapid heating and cooling cycles can lead to microsegregation and the formation of metastable phases in the as-built microstructure of AM materials, making it difficult to accurately model the highly non-equilibrium phase transformations using equilibrium thermodynamics alone. To overcome this challenge, researchers have applied the Scheil-Gulliver (Scheil) model [85] for non-equilibrium solidification to FGMs, which has shown reasonable agreement with experimental observations [21, 117]. However, further research is needed to accurately capture the complex physics of non-equilibrium solidification as a function of composition in dissimilar alloy systems.

Post-processing steps offer a means to reduce the microstructural deficiencies commonly associated with AM alloys, including microsegregation, residual stress, anisotropy, and the formation of detrimental phases [121]. Although post-processing techniques such as homogenization and aging are widely employed, the next-generation of AM materials should seek to minimize or eliminate the need for such steps to achieve the desired property targets. Doing so would effectively reduce lead times and costs associated with AM alloys. This will also avoid compatibility issues when heat-treating FGMs with two dissimilar alloys requiring different heat treatments. Two promising strategies for achieving this goal are controlling process-structure-property relationships through judicious manipulation of process parameters [26] and harnessing the unique non-equilibrium solidification behavior of the AM process [122].

Our research objective is twofold: first, to demonstrate the successful fabrication of a dissimilar steel FGM with location-specific properties that cover a wide range of the steel property space, and second, to develop a TRIP (transformation-induced plasticity) and TWIP (twinning-induced plasticity) steel by mixing dissimilar steel feedstocks. We employ a combination of CALPHAD modeling, metallurgical knowledge, and a data-driven machine learning approach for predicting stacking fault energy (SFE) to select two dissimilar steel feedstocks, i.e., stainless steel 316L (SS316L) and high strength low alloy 100 (HSLA-100) steel, that are compatible for manufacturing FGMs and produce TRIP and TWIP effects. Our work represents an advancement in the state-of-the-art thermodynamic modeling of FGMs and demonstrates the successful development of a low-manganese (Mn<1 wt.%) steel with TRIP and TWIP effects in the as-built condition without heat treatment using high-throughput FGM experiments.

## 3.2 Experimental Design & Methodology

SS316L and HSLA-100 steel FGMs were manufactured using a 222XR DED (RPM Innovations Inc., USA) system in an argon purged environment (<5ppm $O_2$, dew point of -53 °C). All the samples studied in this work were printed using a constant laser power of 650 W (1 mm laser spot size), a contour scan speed of 7.62 cm/min, and a hatch scan speed of 10.16 cm/min, giving an energy density of 37.8 J/mm$^2$. Furthermore, a hatch spacing of 0.635 mm, layer height of 0.254 mm, and a hatch rotation of 45° are used. Separate monolithic builds of SS316L, and HSLA-100 steel were manufactured to verify the printing quality before manufacturing the FGM. **Figure 17** shows the morphology of the feedstock powders and the as-built microstructures of SS316L, and HSLA-100 steel. **Table 1** lists the powder feedstock compositions. The HSLA-100 steel feedstock powder is a customized composition (Praxair Surface Technologies, Inc., USA) [123] with a powder diameter of 44-74 µm and the SS316L feedstock powder (Carpenter Technology Corp., USA) has a powder diameter of 45-105 µm.

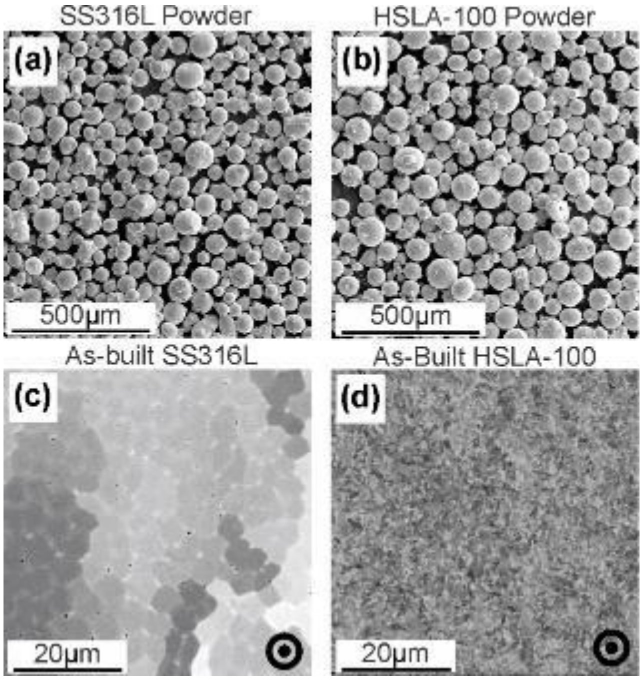

**Figure 17 – Back scatter electron images of the feedstock powders (a & b) and the as-built microstructures of stainless steel 316L (SS316L) and high strength low alloy-100 steel (HSLA-100) (c & d) with the building direction oriented into the page.**

The FGM studied in this work consisted of eleven incremental composition blocks in steps of 10 wt.%, building from SS316L to HSLA-100 steel. Each composition block is approximately 2.4 mm in height. Cylindrical specimens were manufactured such that a compression cylinder could be easily machined from the FGM according to ASTM-E9. Between the deposition of different composition blocks, a 30 second wait time was added to stabilize the powder feeders. The volumetric flow rate of SS316L and HSLA-100 steel powders was calibrated such that the total volumetric flow rate was constant at 1.24 cm$^3$/min, with the volumetric ratio of the feedstocks varying along the build direction. Printed coupons were removed from the substrate using wire electrical discharge machining.

**Table 1 – SS316L and HSLA-100 feedstock powder compositions.**

| Feedstock Alloys | Composition (wt.%) | | | | | | | | | | | | |
|---|---|---|---|---|---|---|---|---|---|---|---|---|---|
| | Fe | Cr | Ni | Mo | Mn | C | Cu | Si | Nb | Al | O | S | P |
| HSLA-100 | Bal. | 0.03 | 3.47 | 0.8 | 0.9 | 0.046 | 1.33 | 0.19 | 0.03 | 0.01 | 0.031 | <0.001 | <0.005 |
| SS316L | Bal. | 17.6 | 12.6 | 2.4 | 1.05 | 0.02 | 0.03 | 0.59 | - | - | 0.01 | 0.004 | 0.008 |

The composition gradient within the FGM was quantitatively measured using a JEOL JXA-8530F (JEOL Ltd., USA) field emission electron probe microanalyzer (EPMA). Compositionally similar steels were used as standards, and the carbon measurement was calibrated using the calibration curve method [124]. To mitigate contamination, a liquid Nitrogen cold finger was used. Bulk composition measurements were done using a probe size of 20 µm, accelerating voltage of 10 kV, and probe current of 50 nA. **Table 2** provides the EPMA-measured composition of the TRIP and TWIP alloy developed in this work. Localized measurements for microsegregation were performed with a probe size of 100 nm, voltage of 10 kV, and probe current of 50 nA. Electron backscatter diffraction (EBSD) images were taken using an EDAX EBSD camera (AMETEK Inc., USA) and analyzed using the TSL-OIM version 8 software. Scanning electron microscopy (SEM) imaging was done using a Scios DualBeam scanning electron microscope (FEI, Thermo Fisher Scientific Inc., USA) operating at 20 kV.

**Table 2 – Composition of the #40HSLA alloy measured with EPMA verses the expected composition based on the feedstock powders.**

| Feedstock Alloys | Composition (wt.%) | | | | | | | |
|---|---|---|---|---|---|---|---|---|
| | Fe | Cr | Ni | Mo | Mn | C | Cu | Si |
| As-built #40HSLA (EPMA) | Bal. | 11.65±0.15 | 9.48±0.15 | 1.83±0.03 | 0.78±0.04 | 0.012±0.01 | 0.36±0.04 | 0.43±0.01 |
| #40HSLA (Expected) | Bal. | 10.82 | 8.95 | 1.76 | 1.07 | 0.033 | 0.49 | 0.43 |

Using an MTS landmark load frame (MTS Systems, USA), the FGM compression cylinder was subjected to a maximum compressive load of 100 kN at an average strain rate of -0.005 m/m/min. The compressive strain was measured using a 3D digital image correlation (Correlated Solutions Inc., USA), and the data was post-processed by VIC-3D version 8 software. Round ASTM-E8 specimen size three tensile bars were manufactured with the loading and build direction parallel to each other. All tensile tests were run with a constant strain rate of 0.015 m/m/min using a Landmark load frame (MTS Systems, USA) equipped with an extensometer running in strain rate control mode. Automated Vicker's microhardness mapping measurements were done using a 100 g force and dwell time of 10 seconds with an AMH55 with LM310AT Microindenter (LECO Corporation, USA).

Location-specific samples for transmission electron microscopy (TEM) were prepared by an FEI Scios DualBeam, using focused ion beam (FIB) milling. Energy dispersive spectroscopy (EDS) was used to verify the composition of the regions of interest. TEM samples were cleaned using a Fischione model 1040 NanoMill (Fischione Instruments, Inc., USA). TEM imaging was carried out using a JEOL JEM2100F TEM (JEOL Ltd., USA) with an accelerating voltage of 200 kV.

Atom probe tomography (APT) samples were prepared using a Thermo Fisher Nova200 (FEI, Thermo Fisher Scientific Inc., USA) FIB using standard lift-out, sharpening, and 2 kV cleaning techniques [125]. The APT experiments were conducted in laser mode using a LEAP4000XHR (CAMECA Instruments Inc., USA) with a 0.5% detection rate, 60K base temperature, 60 pJ laser energy, and a pulse repetition rate set to acquire all ions between pulses.

## 3.3 Results & Discussion

SS316L and HSLA-100 steel were selected as feedstocks based on their printability, complementary properties, and the potential for developing a TRIP and TWIP steel with improved strength and ductility. SS316L is an austenitic stainless steel with an approximate SFE of 32.8 mJ/m$^2$ [126], which is within the range of 20-40 mJ/m$^2$ where TWIP effects are expected during deformation [127]. Previous studies have reported TWIP effects in SS316L fabricated using laser powder bed fusion [126, 128]. In contrast, the typical microstructure of HSLA-100 steel consists of a mixture of martensite and bainite. Thus, HSLA-100 steel does not have TRIP or TWIP effects. The first HSLA (High Strength Low Alloy) steel for AM was developed for the US (United States) Navy through research conducted in the Physical Metallurgy and Materials Design (PMMD) Lab at the University of Pittsburgh [91, 123, 129, 130]. HSLA steel is commonly used in submarines, pipes, offshore structures, and ship hulls for its combination of weldability and strength. The high yield strength of HSLA steel is attributed to the precipitation strengthening from Cu and $M_2C$, making HSLA steel an excellent candidate for structural applications [131].

Considering the SFE range introduced between two dissimilar steels, we hypothesize that mixing martensitic steel (HSLA-100) with austenitic stainless steel (SS316L) using DED will produce an alloy mixture at which austenite becomes metastable, yielding a novel TRIP and TWIP steel. Using a machine learning approach [127], we predicted the SFE of the SS316L and HSLA-100 steel mixtures to be in the range where TRIP and TWIP effects are possible (20-40 mJ/m$^2$) [126]. Additional screening using the Scheil [85] solidification model coupled with the Kou criteria [81-83] for solidification cracking susceptibility gave us insight into the printability of SS316L and HSLA-100 FGMs. The modeling done in this work and its comparison with experimental observations are provided after the presentation of the experimental results.

**Figure 18(a)** shows the print in progress with an inset schematic of the composition gradient making up the FGM. The FGM consists of eleven incremental 10 wt.% composition blocks, building from SS316L on the bottom to HSLA-100 steel on the top. **Figure 18(b)** shows the as-built surface of the dissimilar steel FGM with iron fillings attracted to the ferromagnetic HSLA-100 steel side after magnetization. To verify our ability to control the composition gradient, we compare quantitative wavelength dispersive spectroscopy measurements with the mixing ratio of the original feedstock compositions. The EPMA measurement of the composition profile shows that dilution between composition blocks is minimal, and the composition gradient matches well with the mixing ratio of the feedstock powders, as shown in **Figure 18(c)**.

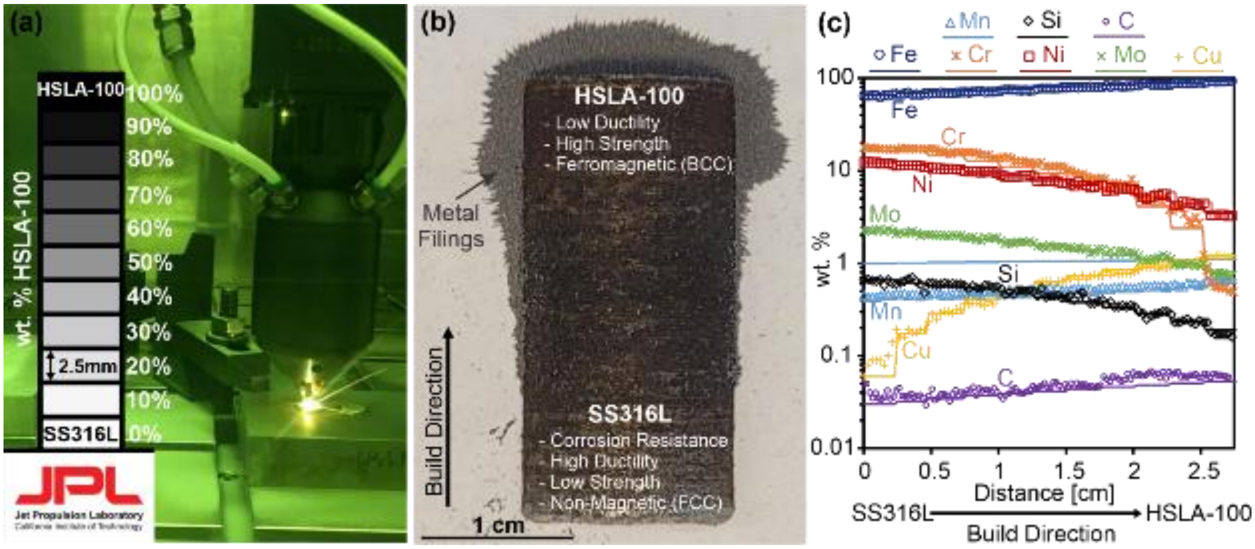

**Figure 18 – Additive manufacturing of a dissimilar steel FGM combining SS316L, and HSLA-100 steel. (a) Image of the DED process with an inset schematic of the SS316L and HSLA-100 steel FGM. (b) Image of the as-built SS316L and HSLA-100 steel FGM showing the gradient in magnetic properties using iron filings. (c) The composition gradient within the FGM measured using EPMA (symbols) compared with the nominal gradient calculated based on the powder feedstock compositions (lines).**

In this study, the use of multi-material AM enables an efficient and streamlined approach for characterizing microstructures and evaluating novel alloy mixtures. The combination of

SS316L, HSLA-100 steel, and their alloy mixtures within the FGM allowed for the efficient collection of microstructural data through high-throughput techniques such as serial EBSD analysis, microhardness mapping, and compression testing. Microhardness mapping, shown in **Figure 19,** was employed to measure the hardness gradient within the FGM. Serial EBSD maps stitched together in **Figure 20** reveal significant changes in microstructural texture. Specifically, the transition from an austenitic FCC solid solution phase on the SS316L side to a martensitic and bainitic BCC dominant structure on the HSLA-100 steel side is observed. Of particular interest is the two-phase FCC and BCC microstructure observed within the 20-60 wt.% HSLA-100 steel region since metastable austenite is a requirement for TRIP and TWIP steel.

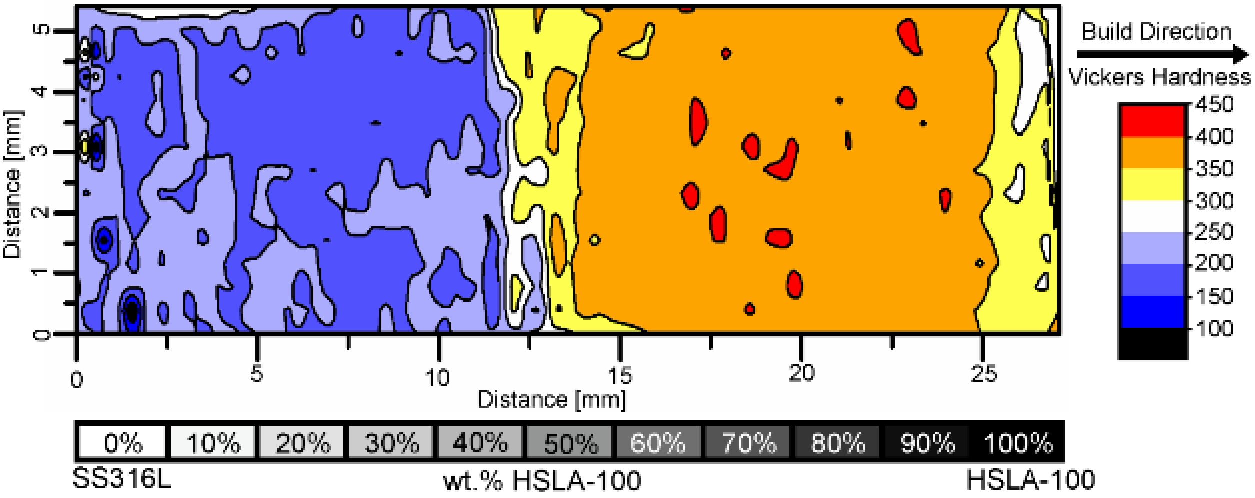

**Figure 19 – Microhardness map showing the change in hardness within the as-built SS316L, and HSLA-100 steel FGM.The change in hardness around 40 wt.% HSLA-100 is caused by the transition from an austenitic to martensitic dominant microstructure.**

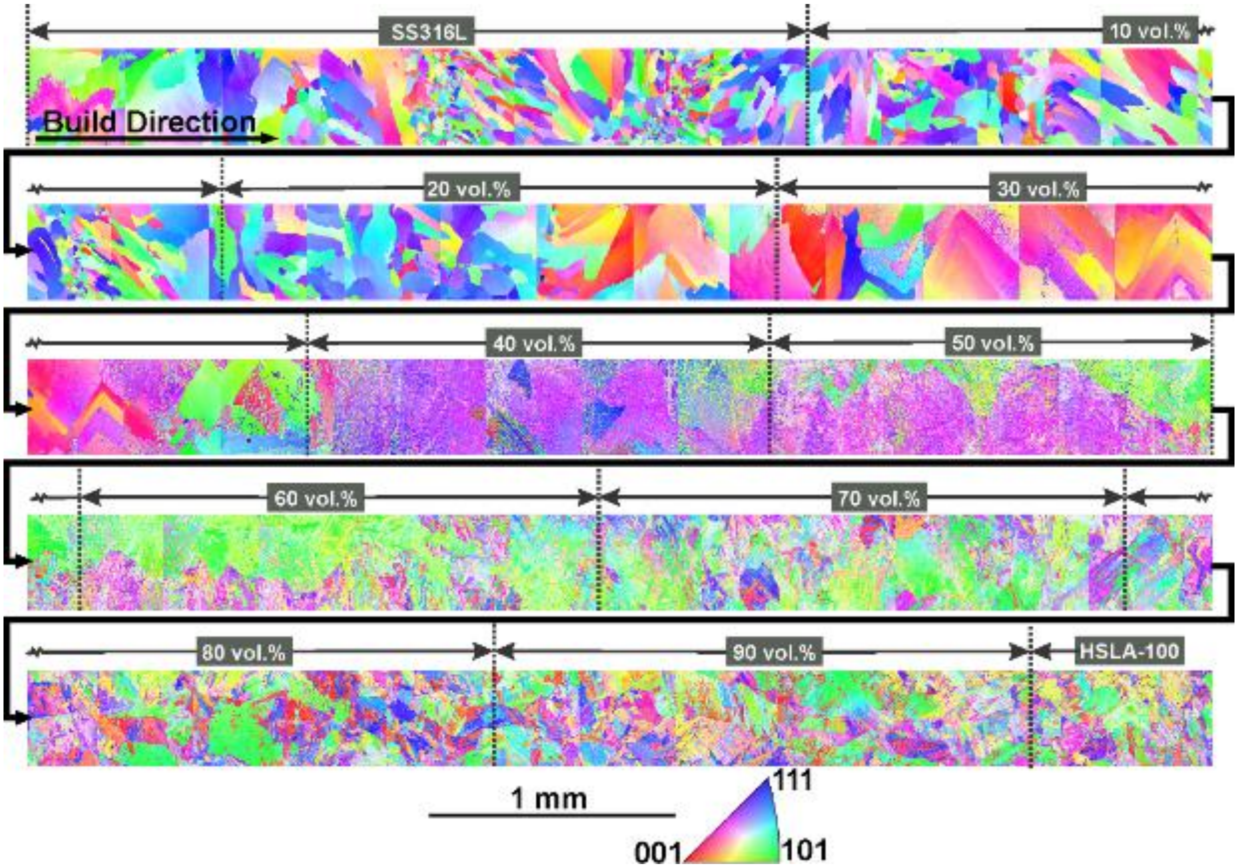

**Figure 20 – Microstructure evolution of the additively manufactured SS316L and HSLA-100 steel FGM shown through an inverse pole figure.The stitched inverse pole figure is separated into rows that end on the right and pick up where they ended on the left one row below. The total length of the serial EBSD scan is more than 25 mm.**

We fabricated a compression cylinder from the FGM to investigate how the active deformation mechanism varies with composition. This allowed for a one-piece sample after deformation that could be efficiently characterized. The resulting engineering stress-strain curve from the compression test is presented in **Figure 21(a)**. Above the yield point, we observe a significant hardening effect until 800 MPa, which is the maximum compressive stress possible using the load frame. To visualize the strength and ductility gradient within the FGM under the maximum compressive stress, we employ 3D digital image correlation to visualize the resulting strain field shown in **Figure 21(b)**. Most of the deformation occurs in the SS316L-rich portion of the FGM. **Figure 21(c)** shows an image of the FGM compression cylinder after compression testing, demonstrating the strength and ductility gradient enabled by multi-material AM.

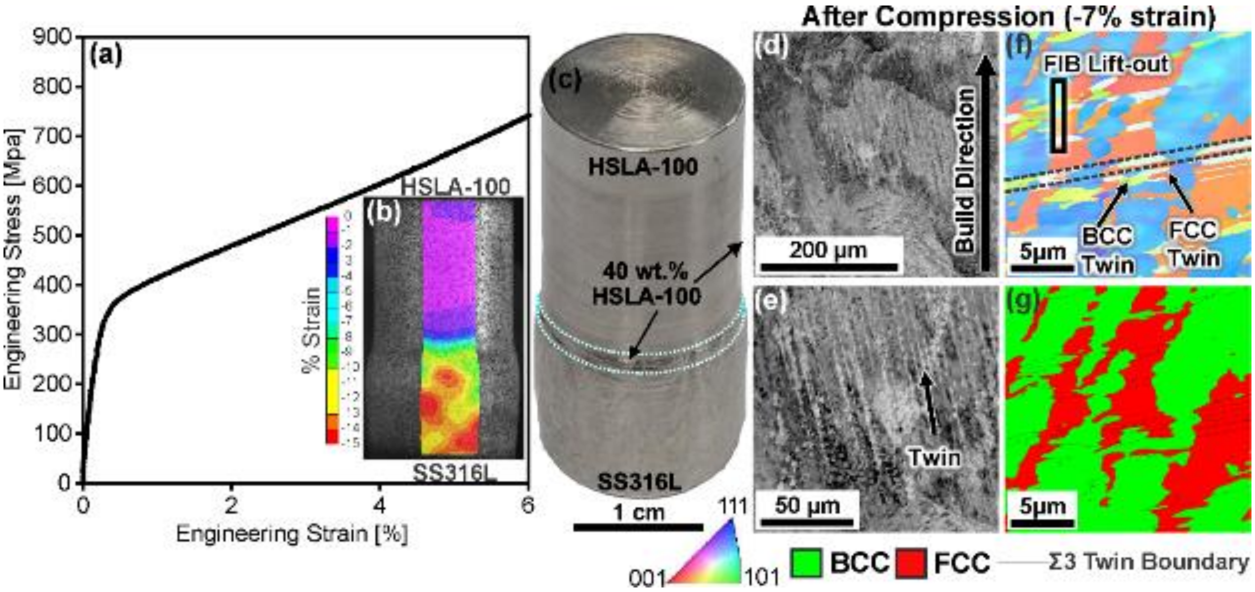

**Figure 21 – Compression testing of the as-built SS316L and HSLA-100 steel FGM. (a) Net engineering stress-strain curve measured using 3D digital image correlation.(b) Engineering strain field in the vertical direction for the SS316L and HSLA-100 steel FGM under the peak compressive stress of 800 MPa. (c) Image of the SS316L and HSLA-100 steel FGM compression cylinder after deformation with the 40 wt.% HSLA-100 steel mixture marked. (d) Backscatter electron image of the 40 wt.% HSLA-100 steel mixture after deformation. (e) Higher magnification image of deformation twins from the region in (d). (f) Inverse pole figure of the 40 wt.% HSLA-100 steel mixture after compression showing deformation twining in both the FCC and BCC phases. The location of a lamella prepared for TEM analysis is marked. (g) Phase map of the 40 wt.% HSLA-100 steel mixture after compression showing Σ3 twin boundaries in both the FCC and BCC regions.**

Following the compression test, we conducted electron microscopy on the two-phase region (20-60 wt.% HSLA-100 steel) to detect TRIP and TWIP effects. Unique deformation twinning behavior is observed in the 40 wt.% HSLA-100 steel mixture, as illustrated by the SEM images in **Figure 21(d-e)**. We identify Σ3 twin boundaries in both the FCC and BCC phases, as shown by the backlines in **Figure 21(g)**. Notably, the inverse pole figure in **Figure 21(f)** and the corresponding phase map in **Figure 21(g)** indicate that the deformation twins cross or bypass the

FCC/BCC phase boundaries within the same prior austenite grain. The BCC twin boundaries are incomplete in some regions, implying detwinning has occurred [132]. According to analysis of the EBSD data, the FCC and BCC phase boundaries conform to the Kurdjumov-Sacks orientation relationship between austenite and martensite/bainite expressed as $\{111\}_{\gamma} \| \{011\}_{\alpha'}$, $\langle\bar{1}01\rangle_{\gamma} \| \langle\bar{1}\bar{1}1\rangle_{\alpha'}$ [133]. For further analysis, we produced location-specific samples for TEM from the region indicated in **Figure 21(f)** using FIB milling.

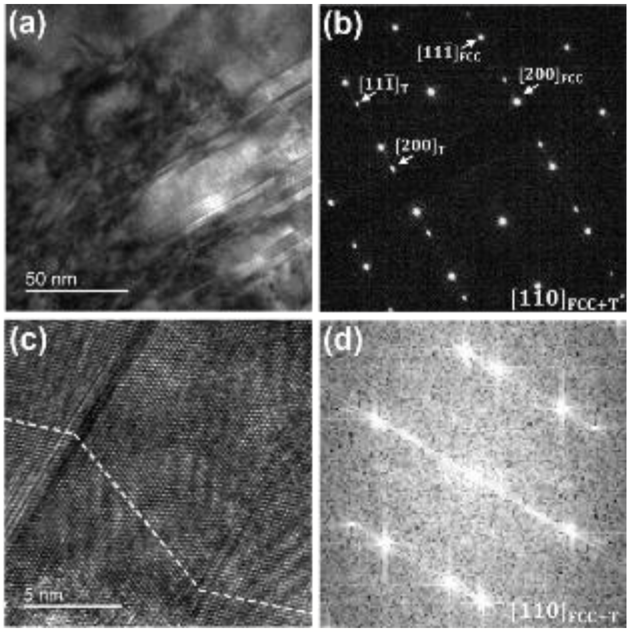

**Figure 22 – TEM analysis of deformation-induced FCC twins within the 40 wt.% HSLA-100 steel mixture after ~7% compressive strain.(a) Bright field TEM image of FCC deformation twins. (b) Selected area electron diffraction pattern from the region shown in (a). (c) High-resolution TEM image of an FCC deformation twin. (d) FFT of the high-resolution TEM image shown in (c).**

**Figure 22(a)** shows FCC deformation twins viewed along the $[110]_{FCC}$ zone axis using TEM. The $[110]_{FCC}$ twin diffraction pattern from the region in **Figure 22(a)** is shown in **Figure 22(b)**. High-resolution TEM imaging on the $[110]_{FCC}$ zone axis is shown in **Figure 22(c)** with the corresponding fast Fourier transform (FFT) in **Figure 22(d)**, confirming the presence of FCC deformation twins at the nanoscale. Imaging the interaction between the twins and FCC/BCC phase boundary was challenging due to magnetic interference from the BCC phase and the natural misalignment of the $[110]_{FCC}$ and $[110]_{BCC}$ zone axis according to the Kurdjumov-Sachs orientation relationship.

TEM analysis of the BCC twins found in the 40 wt.% HSLA-100 steel mixture after compression is presented in **Figure 23**. We identify the BCC phase in the EBSD map **(Figure 21(g-h))** as martensite (α') based on its high dislocation density, lath morphology, and Kurdjumov-Sacks orientation relationship with the retained austenite. Imaging on the $[110]_{\alpha'}$ zone axis confirmed the presence of deformation-induced twinned martensite, as shown by the bright field TEM image in **Figure 23(a)** and the corresponding selected area electron diffraction pattern shown in **Figure 23(b)**. Double diffraction spots, labeled by the white circles, are caused by the twinning plane being off axis from the $[110]_{\alpha'}$ zone axis [134]. The result of an electron diffraction simulation performed using SingleCrystal4 software is shown in **Figure 23(c)** for comparison with the experimental results. We observe double diffraction spots in the experimental diffraction pattern and not in the simulation. More advanced simulations are necessary to reproduce the double diffraction spots observed experimentally and have been simulated by other researchers [135]. High-resolution TEM imaging of the twin interface is shown in **Figure 23(d)**. Binned FFT patterns from different regions in **Figure 23(d)** are shown in **Figure 23(e-h)** to confirm the presence of twinned martensite and show that the extra diffraction spots originate from the overlapping twin interface.

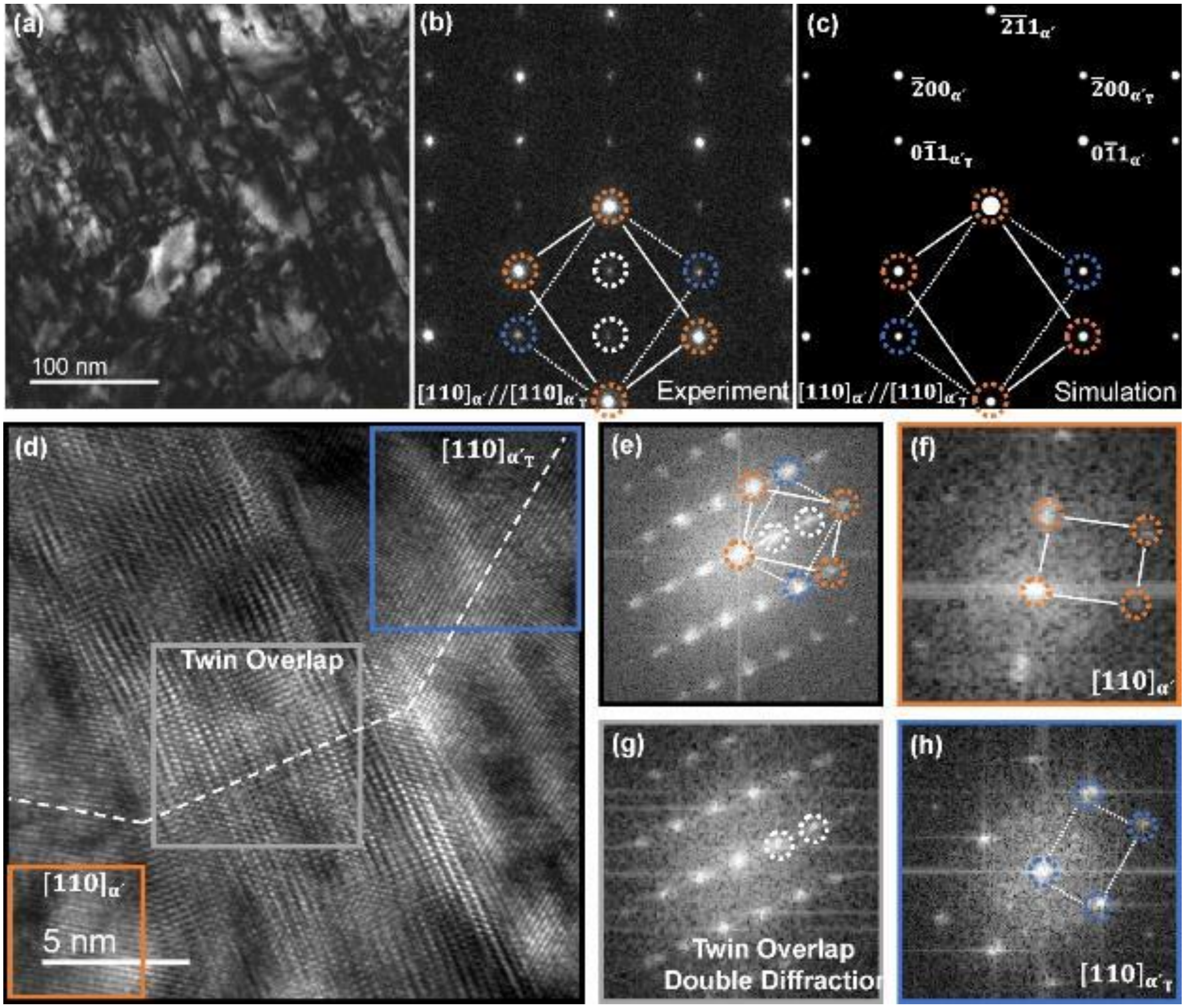

**Figure 23 – TEM analysis of deformation-induced nano twinned martensite ($\alpha'$) within the 40 wt.% HSLA-100 steel mixture after ~7% compressive strain.(a) Bright-field TEM image of nano twinned $\alpha'$ on the $[110]_{\alpha'}$ zone axis. (b) Selected area electron diffraction pattern from the location in (a) with the diffraction spots labeled as the $\alpha'$ matrix (orange), $\alpha'$ twin (blue), and double diffraction spots (white). (c) Simulated electron diffraction pattern of twinned $\alpha'$ on the $[110]_{\alpha'}$ zone axis. (d) High-resolution TEM image of the $\alpha'$ twin interface with the location of the binned FFTs (Fast Fourier Transformation) marked. (e) FFT pattern from the entire high-resolution TEM image shown in (d). (f) Binned FFT pattern of the $\alpha'$ matrix. (g) Binned FFT pattern of the $\alpha'$ twin interface causing double diffraction. (h) Binned FFT pattern of the $\alpha'$ twin.**

In our high-throughput FGM characterization study, we discovered evidence of deformation-induced twinning within the 40 wt.% HSLA-100 steel mixture. This finding motivated us to fabricate monolithic mechanical testing coupons of the 40 wt.% HSLA-100 steel mixture for further analysis. Henceforth, we shall refer to the alloy mixture of 40 wt.% HSLA-100 steel and 60 wt.% SS316L as #40HSLA steel. Tensile specimens of the #40HSLA steel were manufactured under the same processing conditions used for the FGM and then machined into tensile bars. We compare the as-built mechanical properties of #40HSLA steel with those of as-built SS316L, and HSLA-100 steel. The engineering stress-strain curves are shown in **Figure 24(a)**. #40HSLA steel has a yield strength of 415 MPa, an ultimate tensile strength of 960 MPa, and a maximum elongation of 26%. Compared to SS316L and HSLA-100 steel, #40HSLA steel has the highest ultimate tensile strength. #40HSLA steel also exhibits a uniform elongation of 14% engineering strain, more than double that of as-built HSLA-100 steel. The true stress and strain curve for #40HSLA steel, displayed in **Figure 24(b)**, is used to calculate the strain hardening rate shown in **Figure 24(c)** as a function of true stress.

The strain hardening behavior of #40HSLA steel exhibits three distinct deformation regimes, as evidenced by changes in the strain hardening rate. The elastic regime and initial yielding are captured in zone (I). Within zone (II), #40HSLA steel exhibits a remarkable increase in the strain hardening rate between yielding and 0.05 true strain. Subsequently, the strain hardening rate steadily decreases in zone (III) until necking begins. We note that the strain hardening rate of #40HSLA steel differs from the typical behavior of high-manganese TRIP and TWIP steels [136], where the highest strain hardening rate is observed just after yielding, followed by a steady decrease until necking begins. Medium- manganese TRIP steels with 3-10 wt.% manganese has occasionally exhibited similar strain hardening behavior when compared to #40HSLA steel [137]. When rapid grain refinement occurs just after yielding, a rapid strain hardening effect occurs in medium-manganese TRIP steels [138]. However, this strain hardening behavior is not always observed in medium-manganese TRIP steel, as it is dependent on the heat treatment [138]. We postulate that the increase in strain hardening rate after yielding in #40HSLA steel is due to grain refinement from the formation of deformation-induced martensite twins, FCC deformation twins, and the consumption of retained austenite by martensitic transformation. However, a definitive conclusion regarding impact of these dynamic grain refinement mechanisms on the strain hardening behavior of as built #40HSLA steel requires further investigation.

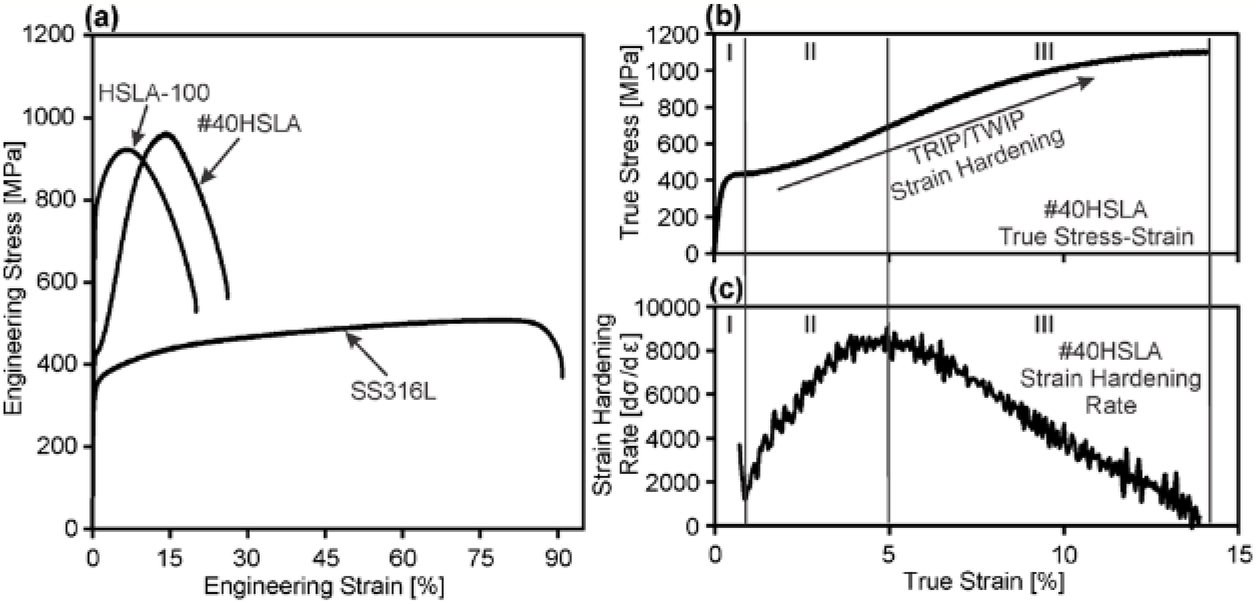

**Figure 24. Tensile testing of the as-built SS316L and HSLA-100 steel compared with as-built #40HSLA steel.(a) Engineering stress-strain relationship from tensile testing of as-built HSLA-100 steel, SS316L, and #40HSLA steel. (b) True stress-strain relationship from tensile testing of #40HSLA steel. (c) Strain hardening rate verses true strain for #40HSLA steel showing a significant increase in the strain hardening rate after yielding.**

The microstructure of as-built #40HSLA steel consists of a dual-phase cellular solidification structure comprised of austenite and martensite stabilized by microsegregation from the printing process. EBSD mapping, presented in **Figure 25(a-c),** shows the microstructure of as-built #40HSLA steel, where austenite (red) occupies the solute-enriched regions between solidification cells. Microsegregation measurements using EPMA line scans were conducted to confirm the phase transformation pathway that resulted in the as-built microstructure. The EPMA measurement **(Figure 25(d-e))** shows that non-equilibrium solidification during the AM process causes microsegregation and leads to a dual-phase cellular solidification structure with a 5 µm cell size in the as-built condition of #40HSLA steel. **Figure 26** compares the as-built microstructure of #40HSLA steel on the x-y and x-z planes.

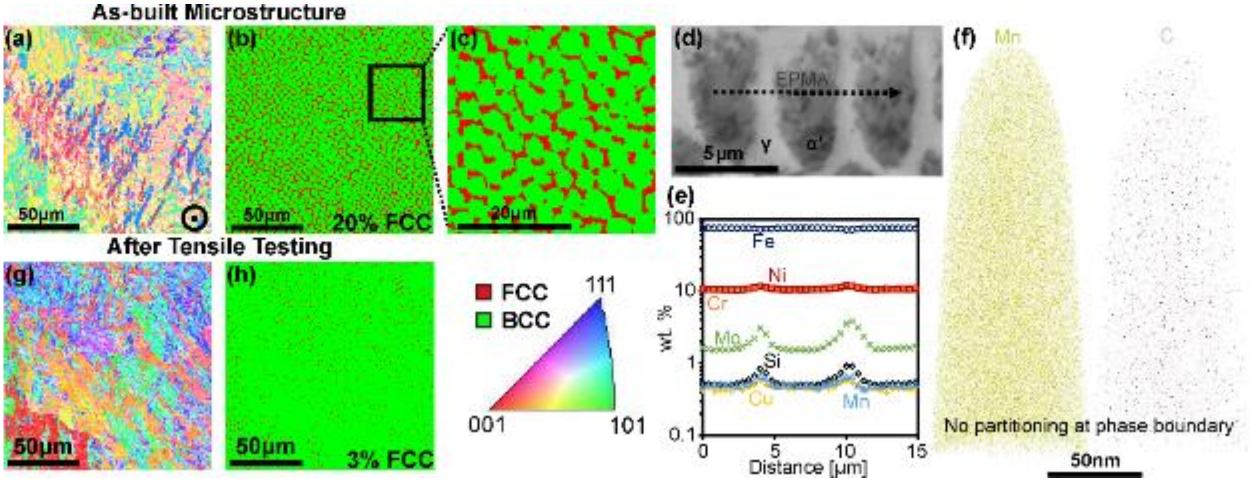

**Figure 25 – Microstructure of #40HSLA steel before and after tensile testing.(a) Inverse pole figure with the build direction marked and (b) phase map of the as-built #40HSLA steel. (c) Magnified phase map of as-built #40HSLA steel. (d) SEM image of the EPMA measurement location. (e) EPMA measurement of microsegregation from non-equilibrium solidification in as-built #40HSLA steel. (f) APT reconstruction of carbon and manganese atoms distributed across the phase boundary between austenite and martensite. (g) Inverse pole figure and (h) phase map of as-built #40HSLA steel after tensile testing.**

Using APT, we investigate carbon and manganese partitioning at the FCC/BCC phase boundary using location-specific FIB lift-outs. Three APT needles were carefully prepared to isolate the FCC/BCC phase boundary. The reconstruction of one of these APT needles is shown in **Figure 25(f)**, revealing that there is no partitioning of manganese or carbon across the FCC/BCC phase boundary. Although there is a heterogeneous distribution of alloying elements from microsegregation, there is no partitioning at the FCC/BCC phase boundary since the BCC phase is martensite formed by diffusionless transformation upon rapid cooling. Medium manganese steels with similar strain hardening behavior use annealing or partial austenization heat treatments to partition manganese into the austenite and lower the stacking fault energy, resulting in TRIP effects [137]. As-built #40HSLA steel does not require heat treatment to yield TRIP and TWIP effects because microsegregation enriches the interdendritic region with solute elements, stabilizing austenite with low stacking fault energy at room temperature. After the tensile test, #40HSLA steel tensile bars were cross-sectioned and compared with the as-built microstructure. EBSD images of the #40HSLA alloy microstructure after tensile testing are presented in **Figure 25(g-h)**, revealing a significant reduction in the fraction of retained austenite after tensile testing due to TRIP effects. The EBSD phase maps in **Figure 25(b&h)** show the FCC phase fraction is reduced from 20% to 3% after tensile testing.

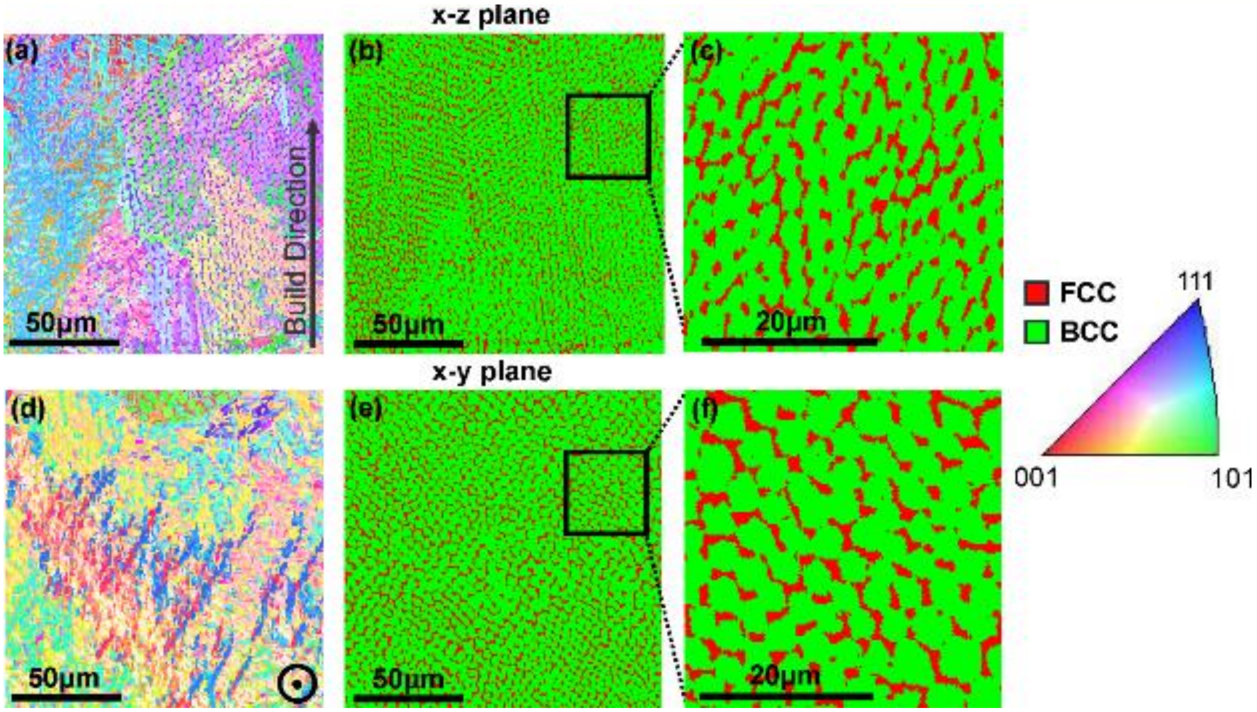

**Figure 26 – EBSD mapping of the as-built microstructure of #40HSLA steel in different orientations.Inverse pole figure (a), phase map (b), and magnified phase map (c) of the x-z plane. Inverse pole figure (d), phase map (e), and magnified phase map (f) of the x-y plane.**

Using a combination of CALPHAD and experiments, we uncover the phase transformations that produce the microstructure of the FGM. We model non-equilibrium solidification, martensitic transformation, and stacking fault energy to predict the as-built microstructure and validate the conclusions drawn from experiments. Using Thermo-Calc software (version 2022b) [76] with the TCFE12 steel database, we performed Scheil solidification modeling [85] for the alloy mixtures between SS316L and HSLA-100 steel with a 10 wt.% step size. The solidification range predicted from the Scheil model is shown in **Figure 27** as a function of composition with increasing content of HSLA-100 steel. Using the Kou criteria for solidification cracking susceptibility [81-83] coupled with the Scheil model, we predict the solidification cracking susceptibility index as shown in **Figure 27** on the secondary y-axis. The solidification cracking susceptibility never exceeds that of the printable feedstocks, indicating that SS316L and HSLA-100 steel are good candidates for manufacturing FGMs. Solidification cracking is not observed in the dissimilar steel FGM which correlates well with the Kou criteria for solidification cracking susceptibility. The Kou criteria for solidification cracking susceptibility and the solidification range often follow a similar trend in alloys that undergo single-phase solidification, as is the case in our calculations. However, the solidification range fails to predict the experimental solidification cracking susceptibility trend in binary eutectic alloy systems such as Al-Cu. Whereas the Kou criteria for solidification cracking susceptibility can capture the experimental trend in solidification cracking observed in binary eutectic alloys [19, 36]. We note that the Kou criteria for solidification cracking susceptibility will have limitations in predicting the behavior of FGMs combining highly dissimilar materials because differences in mechanical strength and thermal expansion are not considered. However, the Kou criteria for solidification cracking susceptibility can qualitatively predict the solidification cracking susceptibility of the dissimilar steel FGM studied in this work.

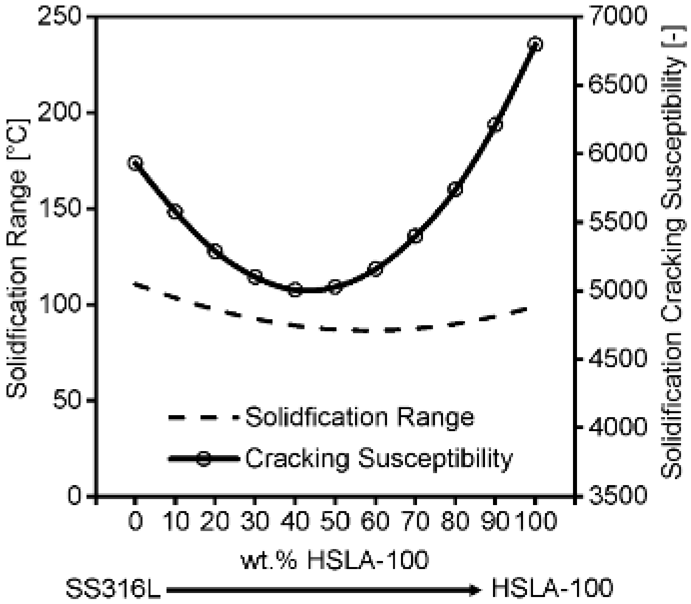

**Figure 27 – Scheil solidification prediction of the solidification range and solidification cracking susceptibility using the Kou criteria for solidification cracking susceptibility in the composition space between SS316L and HSLA-100 steel.**

During AM, non-equilibrium solidification leads to microsegregation in the as-built microstructure of steels [139], influencing their phase stability and SFE. We approximate microsegregation using the classical Scheil model, which calculates the change in solid composition at the solid-liquid interface as a function of solid fraction during solidification. The classical Scheil model does not consider back diffusion, remelting/reheating effects, and deviations from equilibrium at the solid-liquid interface, resulting in a rough approximation of microsegregation in the as-built condition of AM alloys.

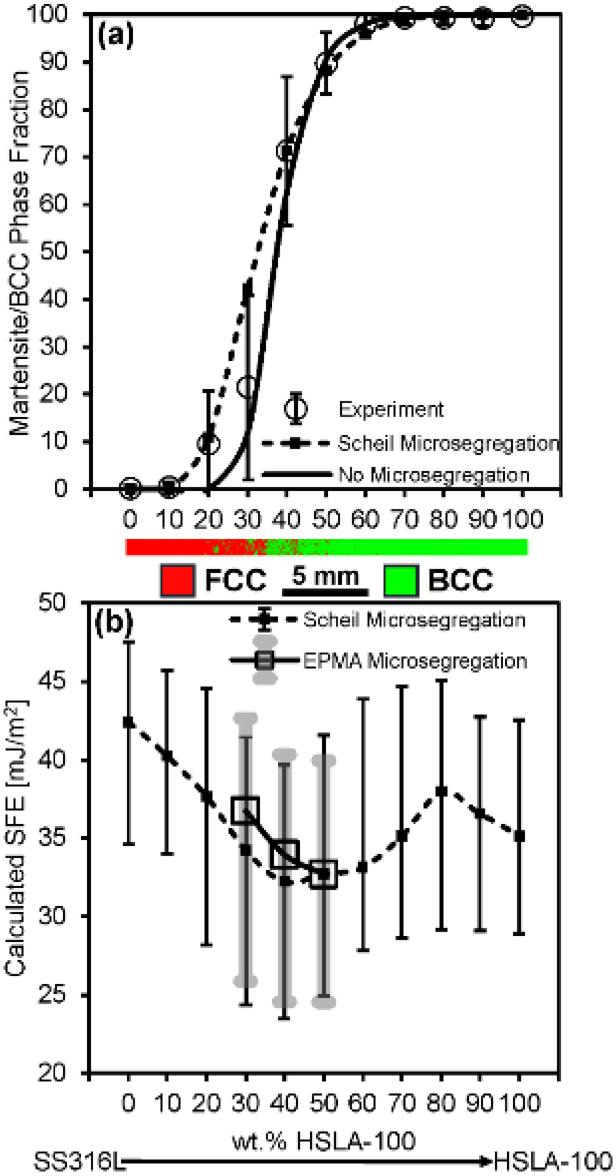

**Figure 28 – Modeling the impact of microsegregation on phase stability and SFE in the as-built SS316L and HSLA-100 steel mixtures.Microsegregation profiles are obtained from Scheil simulations and experimental EPMA measurements. (a) Martensite/BCC phase fraction from EBSD experiments compared to simulations using the nominal alloy composition (No Segregation) and considering microsegregation using the Scheil model (Scheil Segregation). Experimental error bars are provided by splitting up the serial EBSD map (Fig. 2) and taking the standard deviation perpendicular to the build direction. (b) Variation in the calculated SFE caused by microsegregation using segregation composition profiles from Scheil simulations and experimental EPMA measurements. The error bars represent the minimum and maximum SFE values calculated from the Scheil and experimental EPMA segregation profiles.**

To predict the TRIP effect in additively manufactured steels, it is necessary to consider the impact of martensitic transformation on the fraction of retained austenite at room temperature. We utilize the martensite property model available in Thermo-Calc software [76, 140] to predict the martensite phase fraction in the FGM. **Figure 28(a)** displays a comparison of the experimental BCC phase fraction obtained from EBSD with two different modeling approaches. In the first approach (No Microsegregation), we simply input the nominal composition to calculate the martensite phase fraction. In the second approach (Scheil Microsegregation), we consider the effect of microsegregation by calculating the martensite phase fraction at each point along the microsegregation profile predicted by the Scheil model. The average martensite phase fraction is then calculated by taking the weighted average of each point in the Scheil microsegregation profile based on the change in solid fraction. Considering microsegregation using the Scheil model provides a better fit with the experimental data for most of the experimental data points, as shown in **Figure 28(a)**. Although our simulation matches the experimental BCC phase fraction obtained from EBSD, it does not allow for the clear differentiation between bainite and martensite. This deserves more detailed analysis that is not within the scope of this work.

We employ a data-driven machine learning algorithm for predicting the SFE of steels [127] and utilize the microsegregation profile obtained from the Scheil model to predict the fluctuation in SFE energy caused by microsegregation. Experimental microsegregation measurements were conducted for the 30-60 wt.% HSLA-100 alloy mixtures to compare with the Scheil microsegregation prediction. The fluctuation in the calculated SFE caused by microsegregation is shown **Figure 28(b)**. We compare the SFE calculated along the simulated Scheil and experimental EPMA microsegregation profiles. Error bars are added to the mean SFE by taking the minimum and maximum values calculated along the microsegregation profile. We obtained similar values of calculated SFE when using the experimental EPMA and simulated Scheil microsegregation profiles as inputs to the data-driven machine learning algorithm. Both methods predict the SFE for #40HSLA steel to be between 25-40 mJ/m$^2$, indicating that TRIP and TWIP effects are possible. This corresponds well with the experimental observation of TRIP and TWIP effects in as-built #40HSLA steel. As for the other mixtures of SS316L and HSLA-100 steel, we also observed TRIP and TWIP effects in 30 wt.% HSLA-100 steel after compression. TWIP effects are observed in the 0-20% HSLA-100 steel mixtures after compression, corresponding well with the increase in SFE relative to the 30 and 40 wt.% HSLA-100 steel mixtures. Lastly, no TRIP or TWIP effects are observed in the 50-100 wt.% HSLA-100 steel mixtures because little austenite is present in the as-built microstructure.

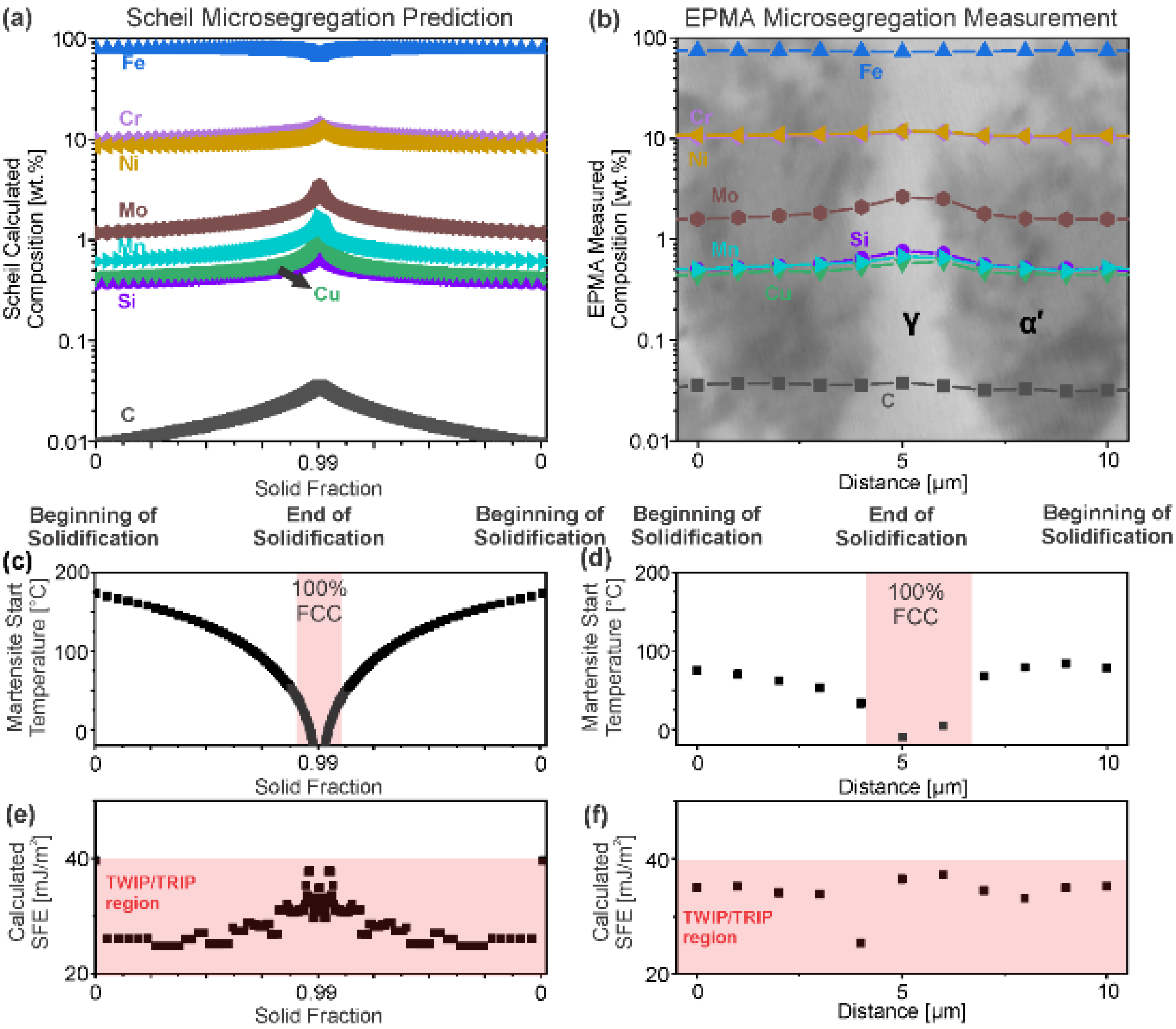

**Figure 29 – Modeling the impact of microsegregation on martensite start temperature and SFE for the #40HSLA steel alloy.(a), (c) and (e) Results based on Scheil simulated segregation profile, which is obtained using Thermo-Calc software [40] with the TCFE12 database. (b), (d) and (f) Results based on EPMA measured segregation profile. The Scheil results are plotted from the start of solidification to the end of solidification. The EPMA scan is taken from the center of the segregation cell to center of another, and an image of the measurement location is included as the background of (b). The martensite start temperature is calculated using Thermo-Calc software based on the work by Stormvinter et al. [140]. The SFE is calculated using the data-driven machine learning model by Wang et al. [127].**

**Figure 29** presents a case study on the impact of microsegregation on phase stability and SFE for as-built #40HSLA steel. The results presented in **Figure 29** provide a detailed look into the modeling approach used to predict the microstructure of the FGM **(Figure 28)**. The Scheil simulation **(Figure 29a)** shows that the solid forming towards the end of solidification is enriched with minor alloying elements (C, Si, Cu, Mn, Mo) as well as Cr and Ni to a lesser extent. The experimentally measured segregation profile obtained from EPMA **(Figure 29b)** shows a fair agreement with the calculated composition profile using the classical Scheil model with some significant differences for carbon. These differences are caused by back diffusion not being considered in the classical Scheil model. We calculated the martensite start temperature of each data point in the segregation profile using the martensite property model in Thermo-Calc software based on the work by Stormvinter et al. [140] to show the effect of microsegregation on the austenite/martensite phase stability. As shown in **Figure 29(c-d)**, solid forming at the beginning of solidification will mostly transform to martensite, while the terminal solid will form a fully austenitic microstructure. The martensite start temperature calculated using the Scheil and EPMA microsegregation profile follows the same trend. However, the magnitude of the martensite start temperature is different due to differences in the predicted and experimental microsegregation profiles. In addition, we predict the SFE for each point along the simulated and experimental microsegregation profile using the data-driven machine learning model by Wang et al. [127], as shown in **Figure 29(e-f)**. Although the resulting trend in the SFE is different when using the simulated and experimental microsegregation profile as the input to the machine learning model, the mean SFE predicted using both methods is below 40 mJ/m$^2$, indicating that the retained austenite in #40HSLA steel should have TRIP and TWIP effects.

### 3.4 Chapter Summary & Conclusion

Using the DED as a tool for alloy development, we have achieved remarkable success in fabricating a functionally graded material (FGM) comprising SS316L and HSLA-100 steels, endowed with location-specific properties such as magnetism, corrosion resistance, strength, and ductility. Leveraging this additively manufactured FGM, we have embarked on a high-throughput experimental endeavor to explore and discover novel steel alloys suitable for AM, incorporating transformation-induced plasticity (TRIP) and twinning-induced plasticity (TWIP) effects. By blending SS316L and HSLA-100 steel mixtures within a single-sample configuration, we have harnessed the power of high-throughput experimental techniques, facilitating the efficient collection of microstructural data.

Compression testing of the FGM has yielded a significant breakthrough, leading to the identification of a promising steel alloy, namely #40HSLA steel. Notably, tensile testing of #40HSLA steel has highlighted the successful development of a low-manganese steel exhibiting TRIP and TWIP effects in the as-built condition, obviating the need for heat treatment. Remarkably, #40HSLA steel has achieved an ultimate tensile strength of 960 MPa, accompanied by a total elongation of 26%. Additionally, it displays a distinctive strain hardening rate that exhibits an increase after yielding up to 0.05 true strain.

To elucidate the microstructural characteristics of #40HSLA steel, as well as the SS316L and HSLA-100 steel FGM, we have adopted a comprehensive approach combining CALPHAD modeling and experimental investigations. Through these combined efforts, we have uncovered the phase transformations that govern the microstructure of #40HSLA steel and the FGM. Notably, non-equilibrium solidification-induced microsegregation has been identified as a significant factor causing fluctuations in phase stability and SFE within the as-built steels, thus enabling the manifestation of unique TRIP and TWIP behaviors even in the absence of heat treatment.

This research presents a significant advancement in AM, showing the potential of tailored FGMs for high-throughput exploration of steel alloys with desirable properties. The successful discovery and characterization of #40HSLA steel demonstrates promising avenues for further advancements in alloy design and fabrication using AM techniques.

# 4.0 Exploring Alloy Design Pathway Through Directed Energy Deposition of Powder Mixtures: A Study of Stainless Steel 316L and Inconel 718

Content from the following open access journal paper is used in this section:

- N. Sargent, Y. Wang, D. Li, Y. Zhao, X. Wang, W. Xiong, Exploring Alloy Design Pathway Through Directed Energy Deposition of Powder Mixtures: A Study of Stainless Steel 316L and Inconel 718, Additive Manufacturing Letters 6 (2023) 100133, doi:https://doi.org/10.1016/j.addlet.2023.100133.

AM is a tool for rapid prototyping with complex geometry. However, the cyclic heating and cooling in laser melting processes often cause large columnar grains that dominate the as-printed microstructure, resulting in a strong texture and anisotropic properties that limit the application of AM. In this work, we apply powder-based directed energy deposition to discover new alloys using mixtures of Inconel 718 (IN718) and Stainless Steel 316L (SS316L). We discovered that the 77 wt.% IN718 alloy mixture, with the highest configurational entropy, demonstrated an intriguingly fine grain structure in the as-built condition and after homogenization at 1180°C. Residual stress from the laser melting process was identified as the primary cause of the observed grain refinement phenomenon. Although, a quantitative analysis of the changes in grain size after homogenization in the alloy mixtures of IN718 and SS316L requires further research. The discovery of this unique microstructural behavior shows how in-situ mixing of commercially available powders can be used to develop next-generation feedstock materials for AM and improve the understanding of fundamental process-microstructure-property relationships.

## 4.1 Chapter Introduction

Laser-based AM is a promising prototyping technique because net shape components with complex geometries can be easily fabricated using sliced 3D models [141, 142]. However, many AM processes introduce anisotropy in microstructure and properties due to the unique cyclic melting process with a high thermal gradient [143]. For example, strong grain texture along the build direction in as-printed Inconel 718 (IN718) requires post-heat treatment to reduce directional differences in mechanical strength [144, 145]. Unlike traditional manufacturing methods, thermomechanical processes, such as forging and cold rolling, are avoided to maintain the geometric integrity of AM components. Therefore, identifying effective post-processing steps that eliminate grain texture, residual stress, and segregation while introducing grain refinement is highly desirable.

Directed energy deposition (DED) can mix multiple feedstock materials together to produce new alloy compositions [146] and composition gradients known as functionally graded materials [2, 4, 5]. This unique manufacturing capability is a useful rapid processing method for high-throughput alloy development [60]. Welk et al. [13] mixed a bulk metallic glass with a high entropy alloy to investigate the glass-forming ability of novel alloy mixtures. Kong et al. [16] used dual feed AM to investigate the effect of Nb concentration on the microstructure and mechanical properties of IN718 by mixing two IN718 feedstocks with different Nb content. Pegues et al. [15] mixed Ta, Nb, and T-6Al-4V with a transition metal HEA (CoCrFeMnNi) to investigate the effect of refractory elements on the properties of high entropy alloys. These works primarily focus on the as-built condition of the alloy mixtures or FGMs and do not investigate the impact of heat treatment on the microstructure and properties of the samples, except for the aging study by Kong et al. [16]. Future studies should extend their investigation of as-built alloy mixtures to include post-processed conditions.

It should be noted that, although starting from pure elemental feedstock is possible, it is challenging to manufacture components with the desired composition, especially when alloying elements are required at extremely low concentration levels [17, 31, 147, 148]. Additionally, purchasing feedstock powder with custom compositions typically costs much more than established off-the-shelf alloys, and minimum order size requirements significantly increase the upfront cost and material waste during materials innovation. Qualification of new feedstock powders also requires significant effort with no guarantee the new alloy composition will be successful. Therefore, in-situ mixing of off-the-shelf feedstock materials using the DED process is a promising tool for discovering fundamental process-microstructure-property relationships and developing next-generation alloys for AM at a significantly reduced cost [15]. This work demonstrates that the DED method can effectively discover new alloy compositions by mixing available feedstock materials with good characteristic microstructure-property relationships. Such a methodology of using AM for materials design will assist in expanding alloy inventory for cost-effective engineering applications with increased sustainability.

In this work, we demonstrate a pathway of alloy design and adaptation for AM through microstructure analysis of a functionally graded alloy from stainless steel 316L (SS316L) to superalloy IN718 manufactured using Laser Engineered Net Shaping (LENS®). IN718 is a widely used Ni-based superalloy with excellent high-temperature mechanical properties. SS316L is austenitic stainless steel that is used extensively in different engineering fields [149, 150]. Although these alloy powders are commercially available and have been studied extensively over the past decade [23, 149-156], both alloys suffer from anisotropic properties caused by the columnar grain texture introduced during laser melting [145].

## 4.2 Experimental Design & Methodology

As the starting point of this investigation, an attempt to manufacture a functionally graded material (FGM) from SS316L to IN718 has been made using the LENS® 450 system (Optomec, Inc., USA) [157, 158]. The as-built condition of the SS316L and IN718 FGM was analyzed with optical microscopy and electron backscatter diffraction as shown in **Figure 30 (a-d)** [157, 158]. High-throughput characterization of the FGM from SS316L to IN718 revealed significant grain refinement within the 75 wt.% IN718 composition block as shown by the inverse pole figure maps in **Figure 30(b) and (d)**. Using CALPHAD modeling, the alloy (total) and configurational entropy were calculated as a function of composition for all the possible mixtures of IN718 and SS316L. The configurational entropy, shown in **Figure 30(e)**, reaches a peak at 77 wt.% IN718 and corresponds well with the observed grain refinement in the 75 wt.% IN718 intermediate block within the FGM.

From this initial study, a correlation was observed between configurational entropy and grain refinement, prompting further investigation. It should be noted that the entropy debate in the high-entropy alloy (HEA) research community drove the model prediction of alloy entropy in this work [159, 160]. From a thermodynamic viewpoint, the total entropy is the intrinsic quality that determines the alloy behavior, while the configurational entropy is just one part of the mixing entropy term and is easy to calculate without using software such as Thermo-Calc [76]. Therefore, both total and configurational entropy are calculated as a function of alloy composition **(Figure**

**30(e))** to guide the experimental design. According to the CALPHAD prediction using the Thermo-Calc TCNI11 database, the alloy with 62 wt.% IN718 has the highest value in total entropy, and the alloy with 77 wt.% IN718 has the highest value of configurational entropy. In addition, the alloy mixture with 47 wt.% IN718 shows the same total entropy as 77 wt.% IN718, although its configurational entropy is lower than 77 wt.% IN718.

Based on this analysis, three monolithic coupons with 47, 62, and 77 wt.% IN718 were manufactured using the Optomec LENS® 450 system to evaluate the impact of total entropy versus configurational entropy. **Figure 30(f)** illustrates the DED process used to manufacture the alloy mixtures studied in this work. Cubes with side lengths of 1 cm for each of the desired compositions were manufactured by calibrating the mass flow rate of two powder feedstocks.

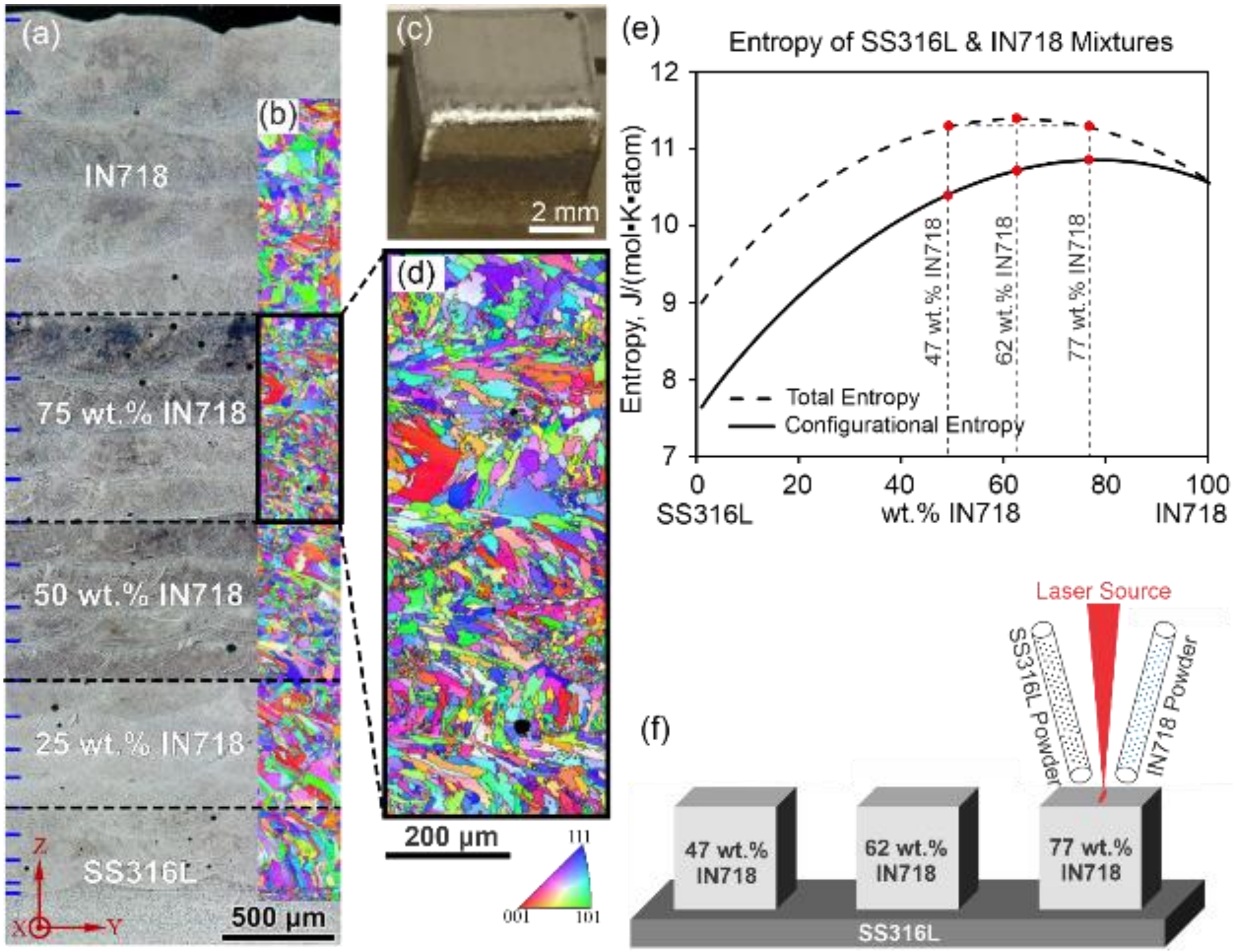

**Figure 30 – FGM manufactured using powder DED for high-throughput experiments [89, 90]. (a) Optical metallography of additively manufactured FGM from SS316L to IN718.(b) Inverse pole figure of grain texture. (c) Image of the IN718 and SS316L FGM before sectioning. (d) Magnified inverse pole figure of 75 wt.% IN718 and 25 wt.% SS316L composition block showing grain refinement. (e) Calculated configurational and total entropy of SS316L and IN718 mixtures. (f) Mixtures of SS316L and IN718 printed to study the effect of entropy on grain refinement.**

All samples printed in this work share the same printing parameters. The printing process optimization was conducted based on the parameters used for pure SS316L and IN718. The optimized parameters are 300W laser power, 50 cm/min scanning speed, 0.381 cm hatch spacing, 0.25 cm layer height, mass flow rate of 6 g/min, 570 µm diameter spot size, and 38 cm/min contour scan speed. The SS316L powder is manufactured by PRAXAIR with the composition of Fe-

0.004C-1Mn-2Mo-17Cr-12Ni (wt.%), and the IN718 powder is from the same company with the composition of: Ni-0.04C-0.01Mn-2.93Mo-0.06Si-18.98Cr-0.41Al-0.94Ti-5.09Nb-18.15Fe (wt.%). The flow rate of the two feedstocks was calibrated using the baggy test method to achieve a constant net flow rate of 6 g/min with the desired mixing ratio. In the baggy test method, a plastic bag is attached to the nozzle of the printing head while the powder feeder operates at a constant rotational speed. After thirty seconds, the feeder is stopped, and the mass of the powder in the bag is measured. This test is then repeated at different powder feeder rotation speeds to determine the linear relationship between the rotations per minute and mass flow rate.

EDS was used to confirm that the composition of the printed alloy mixtures matched the expected ratio of the SS316L and IN718 feedstocks. Large EDS maps were taken from three separate locations within each of the three alloy mixtures studied in this work. **Table 3** summarizes the EDS results and compares the printed composition with the expected values based on the known composition of the SS316L and IN718 feedstocks.

**Table 3 – Measured (EDS) and ideal (expected) compositions of each IN718 and SS316L alloy mixture.**

| Alloy | Composition (wt.%) | | | | | | | |
|---|---|---|---|---|---|---|---|---|
| | Fe | Cr | Ni | Mo | Mn | Nb | Ti | Al |
| 77 wt.% IN718 (EDS) | 29.26±0.29 | 18.58±0.16 | 44.26±0.22 | 2.77±0.02 | 0.42±0.16 | 3.38±0.03 | 0.78±0.06 | 0.24±0.02 |
| 62 wt.% IN718 (EDS) | 37.35±0.09 | 18.22±0.09 | 37.56±0.11 | 2.62±0.05 | 0.57±0.06 | 2.64±0.02 | 0.61±0.06 | 0.14±0.02 |
| 47 wt.% IN718 (EDS) | 43.92±0.64 | 17.96±0.13 | 31.49±0.14 | 2.62±0.12 | 0.78±0.14 | 2.20±0.18 | 0.51±0.06 | 0.11±0.03 |
| 77 wt.% IN718 (Expected) | Bal. | 18.52 | 43.84 | 2.72 | 0.24 | 3.92 | 0.72 | 0.32 |
| 62 wt.% IN718 (Expected) | Bal. | 18.23 | 37.64 | 2.58 | 0.39 | 3.16 | 0.58 | 0.27 |
| 47 wt.% IN718 (Expected) | Bal. | 17.93 | 31.43 | 2.44 | 0.53 | 2.39 | 0.44 | 0.19 |

To evaluate the grain size and phase stability during post-heat treatment after laser melting, both as-built and homogenized samples were studied. After printing, the three alloy mixtures were subjected to high-temperature homogenization at 1180°C for 20 minutes, 1 hour, and 2 hours in an inert atmosphere, followed by ice water quenching. Microstructure analysis was performed using an SEM (FEI Apreo LoVac Analytical) equipped with an EBSD (electron backscatter diffraction) detector at an acceleration voltage of 20 kV and probe current of 13nA. It should be noted that the homogenization temperature is selected according to a comprehensive study performed by Zhao et al. [144] on the IN718 alloy made by AM.

## 4.3 Results & Discussion

To better understand the phase stability and microstructure of the three alloy mixtures, the equilibrium step diagram (phase fraction vs. temperature) and Scheil solidification path have been predicted using the Thermo-Calc software with the TCNI11 database as shown in **Figure 31**. The Scheil modeling indicates that all three samples have two major phases, FCC (γ) and laves, coexisting in the as-built microstructure. Both the Laves and γ phases are observable in backscatter electron images of the as-built microstructures shown in **Figure 32(a-c)**. The Nb-rich Laves phase precipitates along the grain boundaries and in all three alloys. Due to the rapid heating/cooling process, the intermetallic compounds with low phase fractions, such as η and σ, predicted by the Scheil model are not observed. These findings are in good agreement with our previous experimental study on IN718 made by AM [144]. Although MC carbides are not observed in the as-built microstructure, after the dissolution of the Laves phase at 1180°C for 20min, a considerable amount of Nb-rich MC carbide forms inside the grains and along grain boundaries, as shown in **Figure 32(d-l)**. This is consistent with the equilibrium step diagram shown in **Figure 31(d-f)**, where the γ matrix and MC carbides are stable at 1180°C. **Table 4** summarizes the measured volume fraction of MC carbide and Laves phases as measured from the SEM images shown in **Figure 32**. The phase fraction of Nb-rich MC carbide is low in all three alloys, with a slight increase of the MC phase fraction from the alloy with 47 wt.% IN718 to the one with 77 wt.% IN718. The three alloy mixtures of SS316L and IN718 are excellent candidates for investigating the effect of entropy on the grain refinement of additively manufactured metals because they share the same matrix phase, can be processed using the same printing parameters, and contain similar insignificant amounts of secondary phases. CALPAHD modeling was used to estimate the Laves and MC carbide phase fraction in both the as-built and homogenized conditions of the alloys studied in this work, as shown in Fig. 2. These modeling results were used during the experiment's design to ensure the alloys shared similar microstructural characteristics. The similarity of these alloys was confirmed by comparing the area fraction of Laves and MC carbide from SEM images taken of the as-built and homogenized conditions. The area fraction of the Laves phase and MC carbide within each sample is reported in Table S8.

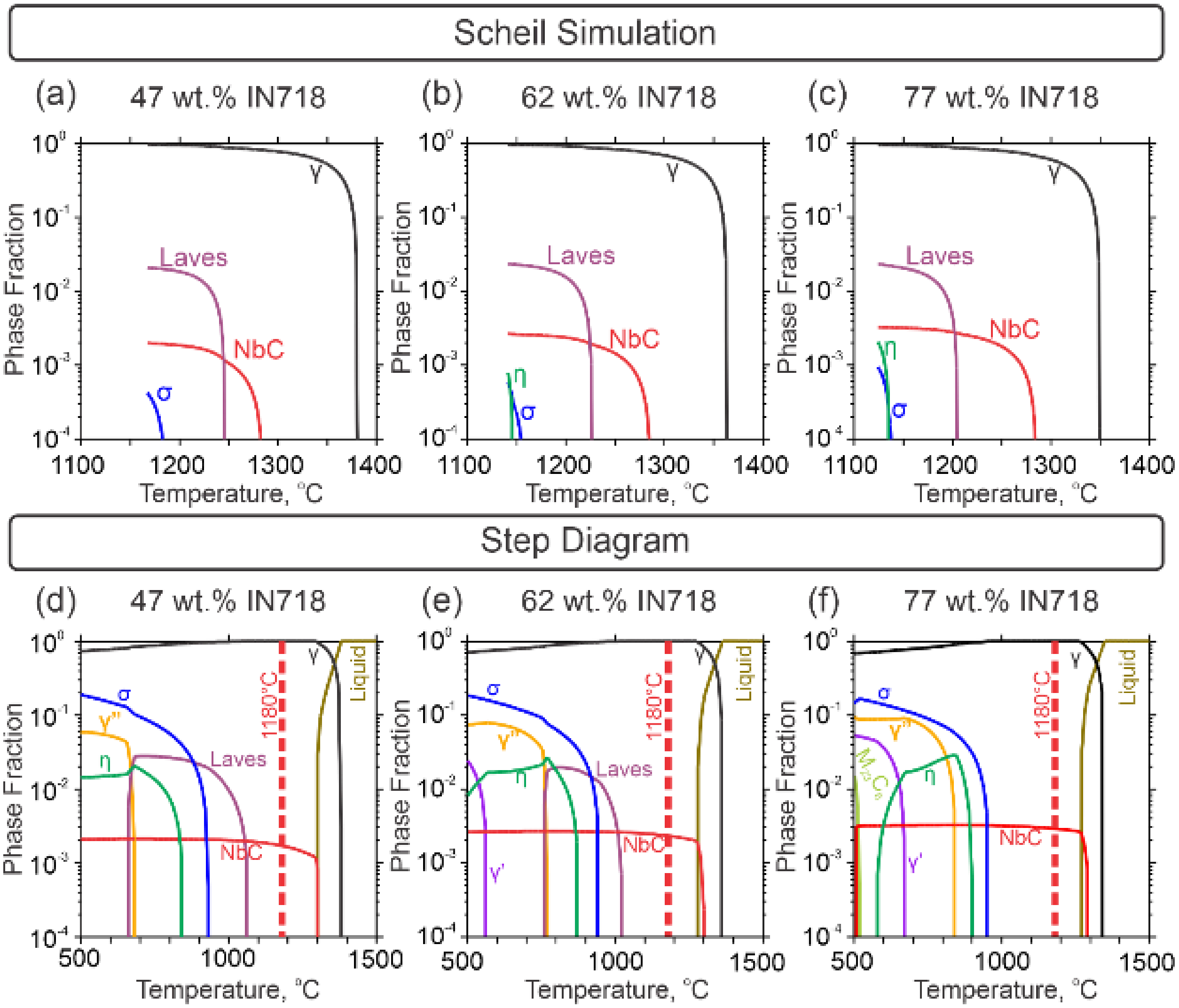

**Figure 31 – Step diagrams and Scheil solidification simulations of the SS316L and IN718 alloy mixtures.(a-c) Eon-equilibrium Scheil solidification modeling of 47, 62, and 77 wt.% IN718, respectively. (d-f) Equilibrium step diagrams of 47, 62, and 77 wt.% IN718, respectively.**

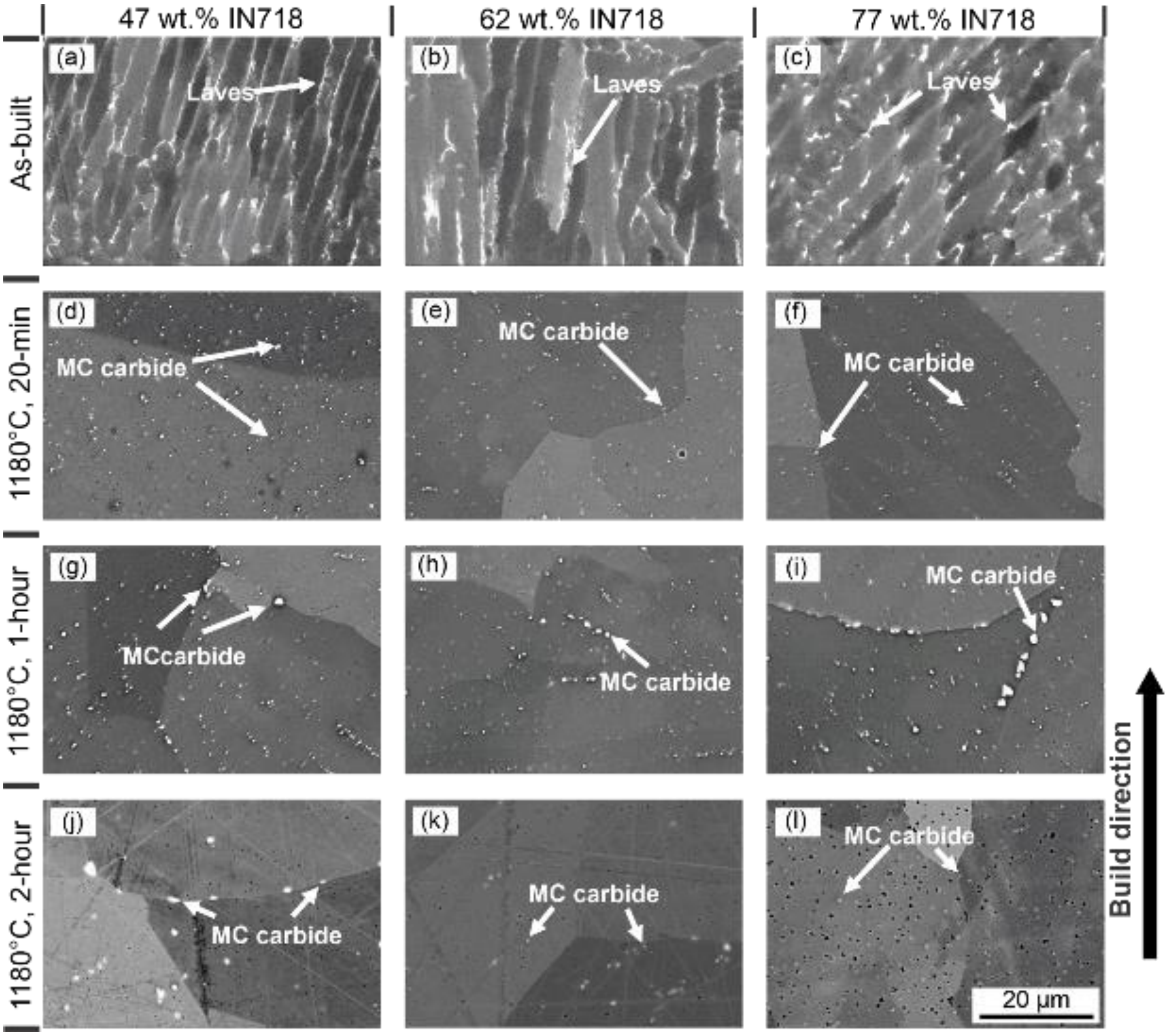

**Figure 32 – Microstructure of SS316L-IN718 alloy mixtures under SEM using backscatter electron imaging. (a-c) show the as-built condition.The samples after homogenization at 1180°C are presented in (d-f) for 20mins, (g-i) for 1 hour, and (j-l) for 2 hours. MC carbides are highly concentrated with Nb and can be considered as NbC. The scale bar shown in (l) can also be used for the other microstructure images.**

**Table 4 – Volume fraction of Laves and MC carbide within each IN718 and SS316L alloy mixture at different conditions.**

| wt.% IN718 (Condition) | Phase | | |
|---|---|---|---|
| | Laves | MC Carbide | FCC (γ) |
| 77% (as-built) | 0.0128 | 0 | Bal. |
| 62% (as-built) | 0.0084 | 0 | Bal. |
| 47% (as-built) | 0.0094 | 0 | Bal. |
| 77% (20-min, 1180°C) | 0 | 0.0007 | Bal. |
| 62% (20-min, 1180°C) | 0 | 0.0008 | Bal. |
| 47% (10-min, 1180°C) | 0 | 0.0007 | Bal. |
| 77% (1-hr, 1180°C) | 0 | 0.0012 | Bal. |
| 62% (1-hr, 1180°C) | 0 | 0.0011 | Bal. |
| 47% (1-hr, 1180°C) | 0 | 0.0009 | Bal. |
| 77% (2-hr, 1180°C) | 0 | 0.0018 | Bal. |
| 62% (2-hr, 1180°C) | 0 | 0.0013 | Bal. |
| 47% (2-hr, 1180°C) | 0 | 0.0011 | Bal. |

IPF (Inverse Pole Figures) with a size of 1200 by 1200 µm were taken to determine the average grain size of the as-built and homogenized samples. **Figure 33** compares the grain size of the as-built and homogenized samples as measured using EBSD. The as-built conditions of all three alloys have a columnar grain structure, and the average grain size is lowest in the alloy with 77 wt.% IN718 (85.5µm) when compared to the other alloys (106.2µm for 47 wt.% IN718 and 141.7µm for 62 wt.% IN718). Using the *TSL OIM* Analysis software developed by EDAX, Inc., the average grain size from each sample and condition is given in **Fig. S1(a)**. The aspect ratio calculated from the EBSD data is shown in **Fig. S1(b)**. Although the aspect ratio remains the same after homogenization, the grain structure in the IPF maps appear less columnar, especially for the 77 wt.% IN718 sample homogenized for 1 hour. One explanation for this discrepancy is that the formation of annealing twins during homogenization counteracts the removal of columnar grain texture and results in a constant aspect ratio.

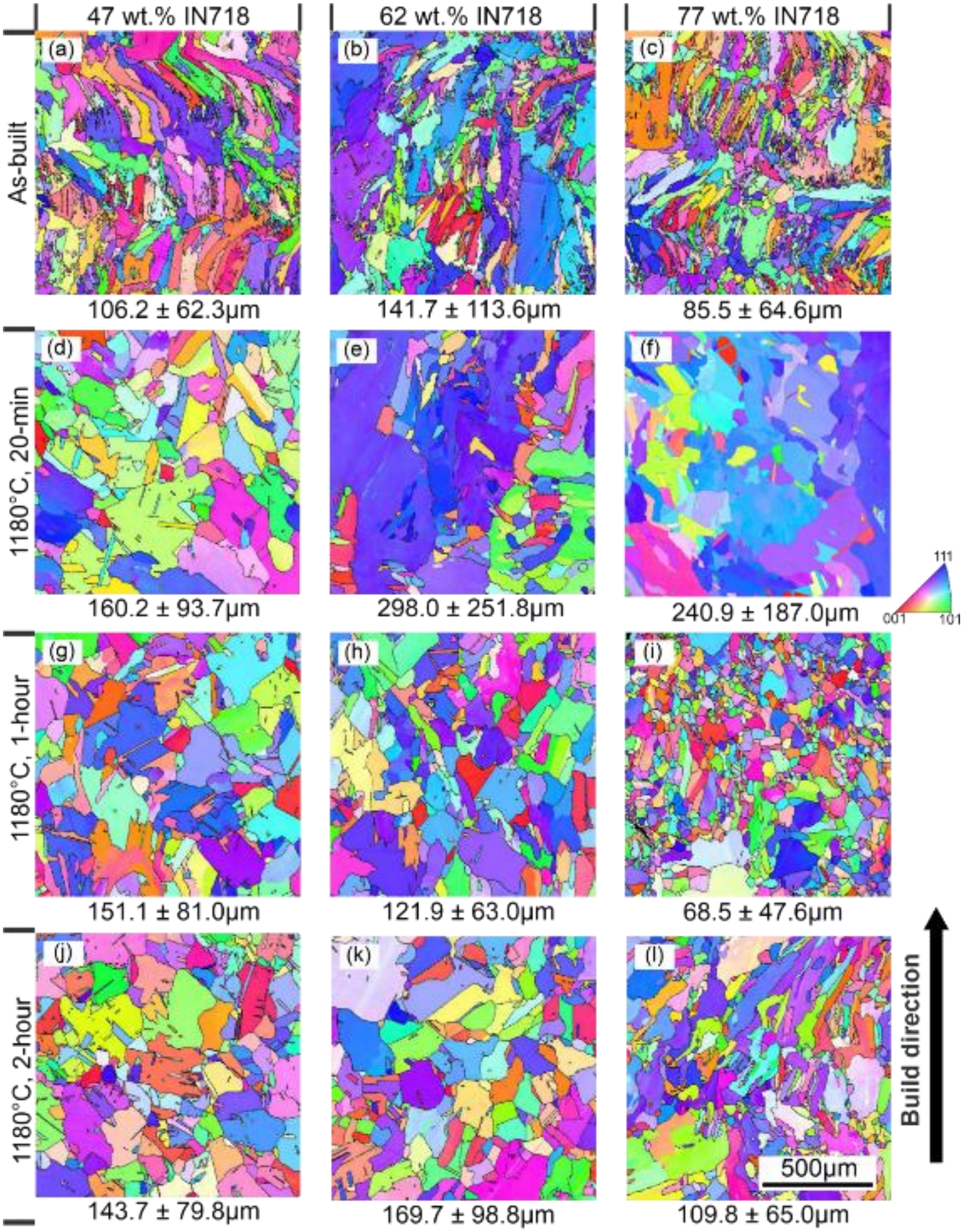

**Figure 33 – Figure 4. IPF maps of SS316L-IN718 mixed alloys.IPF maps of mixed alloys under (a-c) as-built condition, after homogenization at 1180ºC for (d-f) 20 mins, (g-i) 1 hour, and (j-l) 2 hours. The average grain size and standard deviation of each IPF map are shown below the image. The scale bar shown in (l) can also be used for other microstructure images.**

The initial texture of the printed samples and the formation of annealing twins during homogenization causes considerable uncertainty in the standard deviation of the grain size. Therefore, a further dimensional grain size analysis was performed manually on the heat-treated condition according to the intercept procedure of the ASTM standard E112 (Standard Test Methods for Determining Average Grain Size). The horizontal grain size is determined perpendicularly to the build direction, while vertical grain size is along the build direction.

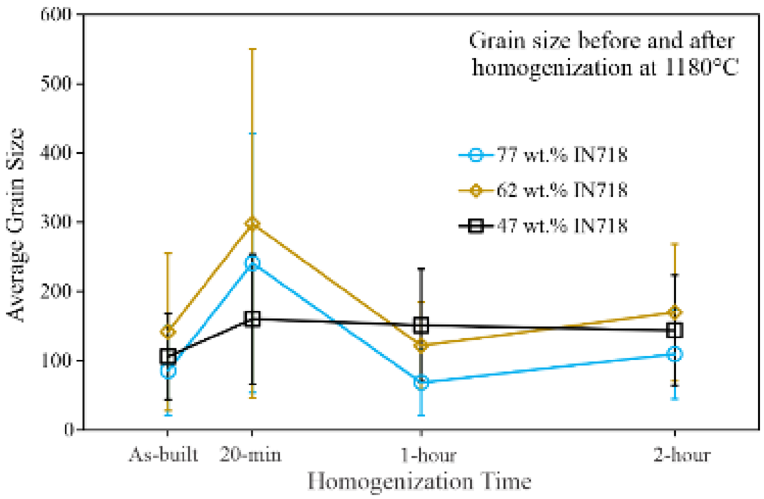

**Figure 34 – Grain size of SS316L-IN718 alloy mixtures at 1180°C as a function of homogenization time.**

The most interesting takeaway from **Figure 33 and Figure 34** is that the grain size of all three alloys reaches a minimum after 1 hour of homogenization, and the alloy with 77 wt.% IN718 still has the smallest grain size. According to the analysis of the average grain size shown in **Figure 34**, the sample with 77 wt.% IN718 after homogenization at 1180°C for 1 hour exhibits the finest average grain size of 68.5 µm. The significant grain refinement seen between the 20 min and 1-hour homogenization steps in all three alloys can be attributed to recrystallization. Such a grain refinement phenomenon is like the observation identified in IN718 superalloy prepared by LPBF (laser powder bed fusion) [144].

Grain orientation spread (GOS) maps were generated from the EBSD data and are shown in **Figure 35**. GOS is considered in this work as a physical quantity to evaluate intergranular distortion and residual stress. Through the combined analysis of grain size and GOS, we gain valuable insights into the recrystallization process. Field et al. [161] pioneered the use of GOS for evaluating residual stress at the microstructural level. A similar comprehensive analysis has been performed by Zhao et al. [144] on IN718 made by LPBF. All three alloy mixtures exhibit the highest GOS values in the as-built condition, as shown in **Figure 35(a-c)**. High GOS levels in the as-built condition imply an elevated level of stored energy in the grains due to the residual stress generated through cyclic heating and cooling. After a 20-min homogenization, recrystallized grains are found in all three alloys, and the overall GOS value is reduced as shown in **Figure 35(d-f)**. In the alloy with 47 wt.% IN718, the GOS value reduces rapidly after only 20-min homogenization, implying the rapid consumption of stored energy. Most grains in the alloy with 47 wt.% IN718, after 20-min of homogenization, have a GOS value near zero. Although some localized areas show higher GOS values due to incomplete recrystallization. Since there is no obvious grain size change, it is reasonable to assume that recrystallization is mostly complete in less than 20-min for the alloy with 47 wt.% IN718. In the alloys with 62 and 77 wt.% IN718, there are several columnar grains with a high GOS value after 20-min homogenization, suggesting that the recrystallization process has not been completed. After 1-hour homogenization, both the 62 and 77 wt.% IN718 alloys undergo further grain refinement, particularly in the vicinity of grains with a high GOS value as shown in **Figure 35(i)**. Recrystallization is finished after 2-hour homogenization at 1180°C, and grain begins to grow further. Overall, the GOS in all three alloys steadily decreases with increasing homogenization time, indicating that the stored energy due to the residual stress from the printing process has been dissipated. Among the three alloys, the GOS of the alloy with 77 wt.% IN718, shown in **Figure 35(l)**, is still higher after 2-hour homogenization than the other two alloys.

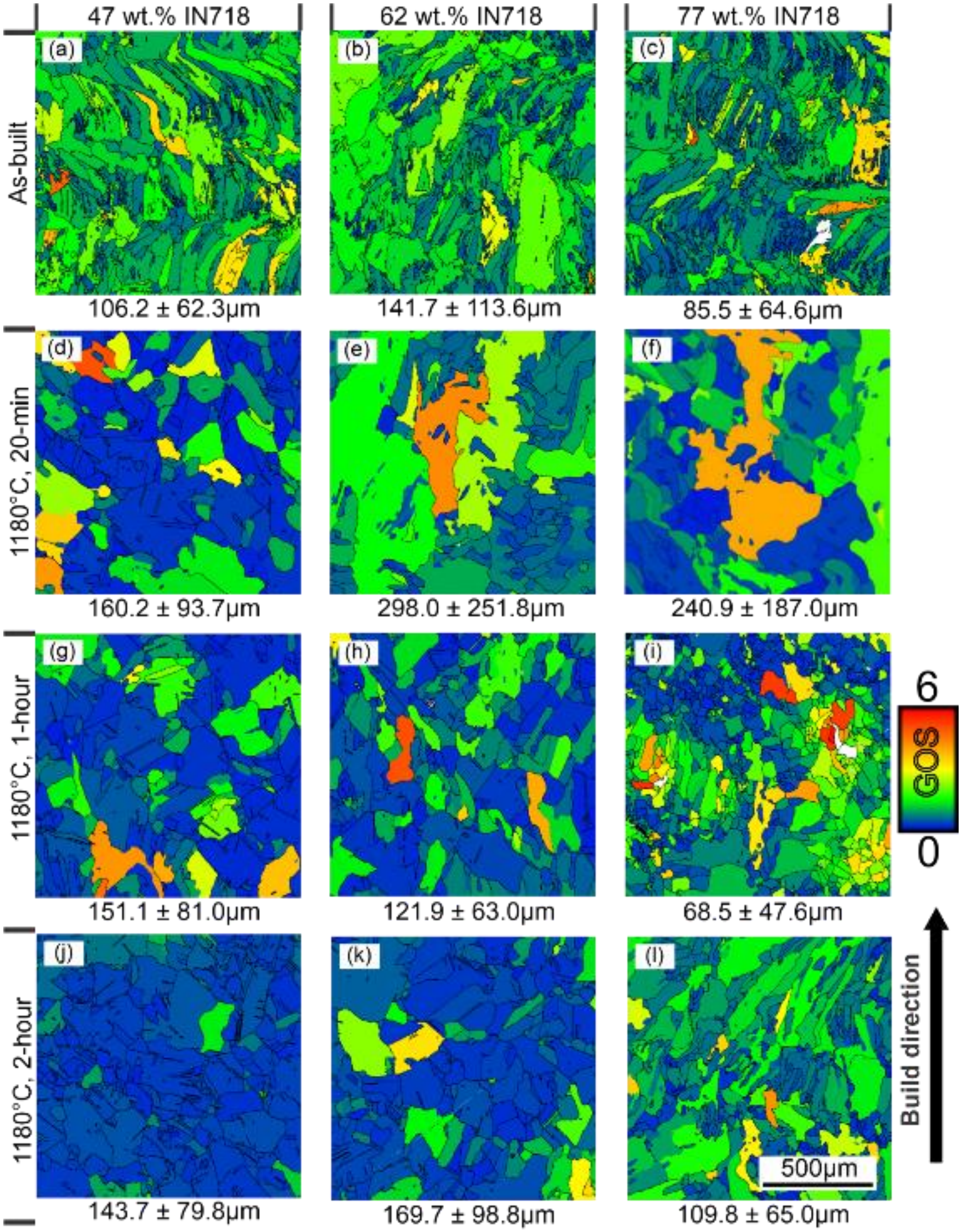

**Figure 35 – Grain orientation spread (GOS) maps of as-built and homogenized SS316-IN718 mixed alloys. GOS maps of mixed alloys under (a-c) as-built condition, after homogenization at 1180oC for (d-f) 20 mins, (g-i) 1 hour, and (j-l) 2 hours. The average grain size and standard deviation of each GOS map is shown below the image. The scale bar shown in (l) can also be used for the other microstructure images.**

The entropy effects are intrinsic since they vary as a function of alloy composition. These three alloys are good candidates for deducing the effect of entropy on microstructure evolution because they all have similar phase stability, e.g., the same FCC matrix phase, similar amounts of the Laves phase in the as-built microstructure, and a similar small fraction of MC carbides. Additionally, all three alloys share a similar processing window. As shown in **Figure 30(e)**, these alloys exhibit different entropies. To evaluate the entropic impact on diffusion kinetics, Thermo-Calc software based on the thermodynamic TCNI11 database coupled with the mobility MOBNI5 database were used to estimate the diffusivities in each of the three alloy mixtures by calculating the diffusion matrix. The diffusion matrix for the three alloy mixtures of SS316L and IN718 are presented in **Table 6-11** within the appendix. Close inspection of the diffusion matrix shows that most diffusivities decrease with increasing configurational entropy. However, if we assume that the diffusion process will be driven by the slowest diffusion, the alloy with 47 wt.% IN718 exhibits the slowest diffusion instead of 77 wt.% IN718, although the difference among these smallest diffusivities is negligible. Overall, the experimental observation and modeling above cannot provide convincing evidence for a definitive relationship between grain kinetics and entropy. Although the initial experimental design was intended to reveal such a relationship, the debate regarding the influence of entropy on the diffusion kinetics in high-entropy alloy systems continues [159, 160].

One possibility is that the grain refinement from recrystallization is too strong, hiding the impact of entropy. Therefore, further work is required to quantitatively describe the effect of entropy on grain refinement and recrystallization in AM alloys. Consequently, it is more conclusive that in the alloy mixtures of SS316L and IN718, grain refinement observed during homogenization at 1180°C can be attributed to recrystallization, which is primarily influenced by residual stress due to the complex heating and cooling cycles during the laser melting process. Even though such a strong influence of the residual stress and its dissipation through recrystallization could be the main cause for such a grain refinement, it is challenging to perform a quantitative analysis without reliable numerical simulations. Analysis of the grain size within each of the three alloys using EBSD reveals that the alloy mixture with the highest configurational entropy, 77 wt.% IN718 has the smallest grain size in the as-built condition and after homogenization for 1 hour at 1180°C.

## 4.4 Chapter Summary & Conclusion

- The capability of DED to fabricate alloys with different compositions by easily manipulating feedstock materials can accelerate alloy discovery and facilitate efficient studies of fundamental process-microstructure-property relationships.
- By adding 77 wt.% IN718 to SS316L, a new alloy with a refined as-built microstructure is discovered. This fine grain structure exists even after high-temperature homogenization, and it was less pronounced in the other alloy mixtures with 47 and 62 wt.% IN718.
- There are three factors contributing to the grain refinement identified in this alloy: grain boundary pinning particles due to MC carbide formation, residual stress induced stored energy due to the unique laser melting process, and entropic influence on diffusion kinetics. More work is required to quantitatively identify these three factors and their role in grain structure evolution.
- It is reasonable to believe that high stored energy due to residual stress from the AM process plays a vital role in grain refinement by promoting recrystallization. Both entropy and grain

boundary pinning effects may also contribute to the grain refinement observed in the studied samples. However, a more detailed mechanistic investigation is required.

- This work demonstrates a successful case study developing a new alloy by in-situ mixing of commercial feedstock powder, SS316L and IN718. The unique grain refinement observed during high-temperature homogenization indicates that the microstructure engineering of new alloys for AM requires a comprehensive design and analysis in both as-printed and heat-treated conditions.

# 5.0 Heat Treatment and Microstructure Degradation of Stainless Steel 316L and Inconel 718 Functionally Graded Materials Exposed to Cyclic Oxidation

FGMs can revolutionize the design of components operating in extreme environments by capitalizing on location-specific material properties to enhance performance and reduce cost. Although multi-material manufacturing shows promise, unforeseen consequences, such as detrimental phase formation, solidification cracking, and compromised mechanical properties at material interfaces limit the application of FGMs. The existing literature lacks comprehensive investigations into the effects of processing, heat treatment, and high-temperature exposure on FGMs, which this chapter aims to rectify. This chapter presents the development of a successful manufacturing and heat treatment strategy for SS316L and IN718 FGMs. Fracture elongations exceeding 60% in both as-built and heat-treated conditions for SS316L and IN718 FGMs are reported. Furthermore, a rigorous study on the microstructural stability and oxidation performance of SS316L and IN718 FGMs under cyclic oxidation at 800°C for 500 hours is conducted. This work represents an advancement in the fabrication of advanced multi-material components for extreme environments. By unraveling the effects of heat treatment and high-temperature exposure on SS316L and IN718 FGMs, this work paves the way for the application of FGMs in extreme environments.

## 5.1 Chapter Introduction

FGMs are manufactured using the DED process by varying the ratio of two or more feedstock alloys during printing to produce location-specific material properties [4, 29, 30]. FGMs also enable the efficient exploration of multicomponent composition space by combining the mixtures of two or more alloys together within the sample. Researchers have increasingly relied on FGMs made with AM to speed up the alloy development process, resulting in significant cost savings [60]. Although FGMs have been applied broadly in advanced engineering applications and alloy development, the effects of heat treatment and high-temperature exposure on the microstructure of FGMs remain relatively unstudied.

Advanced high-temperature materials, such as Nickel-based superalloys, usually require multi-step heat treatments to achieve their optimal high-temperature material properties [154, 162, 163]. For example, IN718 processed by AM requires homogenization to remove microsegregation and aging to facilitate the precipitation of $\gamma'$ and $\gamma''$ to yield the desired high-temperature mechanical properties [144, 145, 162]. Post-processing requirements for superalloys may not always align with those of other materials they are joined with. For example, post-processing of additively manufactured SS316L typically involves homogenization to remove residual stress and microsegregation but does not require aging. Therefore, careful analysis is required to assess the heat treatability of FGMs combining dissimilar materials such as SS316L and IN718.

Several articles have been published on manufacturing of SS316L and IN718 FGMs using DED. Shah et al. [61] investigated the impact of processing parameters on the mechanical performance of SS316L and IN718 FGMs and was able to achieve acceptable tensile strengths but with low ductility. Kim et al. [155] investigated the printability of SS316L and IN718 FGMs and found that alloy mixtures of 20-30% IN718 are prone to cracking. Yang et al. [164] evaluated the mechanical performance of several different joint designs using sharp and graded transitions, all of which demonstrated significantly less ductility when compared to the typical properties of monolithic SS316L and IN718. Ghanavati et al. [151] evaluated the ability to manufacture thin walled SS316L and IN718 FGMs. Lu et al. [165] showed that the mechanical properties of SS316L and IN718 FGMs could be improved after heat treatment but was unable to achieve ductility comparable to monolithic SS316L after aging. Although these existing studies provide useful information on the manufacturability and potential post-processing routes for SS316L and IN718 FGMs, none of them have reported mechanical properties that are comparable or exceeds that of monolithic SS316L and IN718. Furthermore, the existing literature has not investigated the microstructure degradation and oxidation performance of SS316L and IN718 FGMs after high-temperature exposure.

This work aims to address the gaps in the existing literature by demonstrating a ductile SS316L and IN718 FGM in both the as-built and heat-treated condition for the first time. Additionally, this work reports on the oxidation performance and microstructure stability of IN718 and SS316L FGMs exposed to high-temperature.

## 5.2 Experimental Design & Methodology

SS316L and IN718 FGMs were fabricated using a 222XR DED (RPM Innovations Inc., USA) system in an argon purged environment with an oxygen level below 5 parts per million (ppm). Careful control of the manufacturing environment is essential to producing ductile SS316L and IN718 FGMs as previous works have reported premature failure originating from internal oxides [155]. All samples were printed using a consistent laser power of 650 W with a 1 mm laser spot size. The contour scan speed was set at 7.62 cm/min, and the hatch scan speed at 10.16 cm/min, resulting in an energy density of 37.8 J/mm$^2$. Additionally, a hatch spacing of 0.635 mm, layer height of 0.254 mm, and a hatch rotation of 45° were employed.

Two different SS316L and IN718 FGMs were investigated in this study. The first FGM (Sharp) was manufactured with a sharp composition gradient where IN718 was deposited directly on top of SS316L. The second FGM (graded) consisted of eleven composition blocks incrementally increasing by 10 wt.% of IN718, creating a stepped composition gradient. Each composition block had a height of about 2.4 mm, yielding a stepped composition gradient of about 22 mm between SS316L and IN718. A 30-second wait time was included between the deposition of different composition blocks to ensure powder feeder stabilization. The volumetric flow rate of SS316L and IN718 powders was calibrated to maintain a constant total volumetric flow rate of 1.24 cm$^3$/min, with the volumetric ratio of the feedstocks varying along the build direction. Printed coupons were removed from the substrate using wire electrical discharge machining. **Figure 36(a)** depicts the two different FGMs studied in this work (Sharp & Graded).

Both types of SS316L and IN718 FGMs were subjected to the same two step heat treatment followed by cyclic oxidation as shown by the heat treatment schedule depicted in **Figure 36(b)**. Control samples of additively manufactured SS316L and IN718 were also subjected to the same heat treatment schedule depicted in **Figure 36(b)** for comparison with the FGMs. During the two-step heat treatment, all samples were encapsulated in a quartz tube with inert Argon gas and then water quenched following the completion of the heat treatment. Both the as-built and heat-treated samples were cross sectioned, hot mounted, and polished using standard metallographic techniques.

The first heat treatment step consisted of homogenization at 1180°C for 1 hour. Homogenization at 1180°C for 1 hour was chosen based on previous published studies on the effect of homogenization on IN718 made by AM [144, 145, 162, 166]. The phase equilibria of the SS316L and IN718 FGMs during homogenization was evaluated by calculating the phase fraction at 1180°C as a function of the fraction of IN718 using Thermo-Calc software version 2022b [76] and the TCNI12 database as shown in **Figure 36(c)**. Based on the results of the thermodynamic equilibrium calculation in **Figure 36(c),** FCC and NbC are predicted to be the only stable phases during homogenization. Since there are no detrimental phases predicted to form, 1180°C is a suitable homogenization temperature for both SS316L and IN718.

The second heat treatment step consisted of aging at 718°C for 10 hours. The choice of single step aging at 718°C for 10 hours was made to simplify the heat treatment process while also facilitating the precipitation of gamma prime ($\gamma'$) and gamma double prime ($\gamma''$). **Figure 36(d)** presents the phase equilibria during aging within the SS316L and IN718 FGMs when suspending delta (δ) phase in the calculations. δ phase was suspended to represent the metastable nature of $\gamma'$/ $\gamma''$ in this alloy system during aging. Sigma (σ), Laves, and eta (η) phase are predicted to be thermodynamically stable at 718°C. However, the kinetics controlling the formation of topologically close-packed phases are slow at temperatures below 800°C and therefore are not expected to precipitate during aging.

Round ASTM-E8 specimen size three tensile bars were manufactured with the loading and build direction parallel to each other. All tensile tests were conducted with a constant strain rate of 0.015 m/m/min using a Landmark load frame (MTS Systems, USA) equipped with an extensometer operating in displacement control mode. Automated Vicker's microhardness mapping measurements were carried out using a 100 g force and a dwell time of 10 seconds with an AMH55 with LM310AT Microindenter (LECO Corporation, USA).

Cyclic oxidation at 800°C for 500 hours was conducted on the two additively manufactured SS316L and IN718 FGMs along with regular SS316L and IN718 control samples for comparison. Although 800°C is well above the typical maximum operating temperature of IN718 (650-700°C) [167], it was chosen for the oxidation study to accelerate the rate of oxidation and detrimental phase formation. **Figure 36(e)** shows the thermodynamic equilibrium phase fraction at 800°C as a function of the fraction of IN718. σ phase is predicted to be stable throughout the SS316L and IN718 FGM and is likely to form after 500 hours of exposure at 800°C with a volume fraction of 10%. δ phase is predicted to be thermodynamically stable at 800°C in the alloy mixtures containing more than 50% IN718 and is expected to form at the expense of $\gamma''$. Laves and η are also predicted to be thermodynamically stable, but with volume fractions of less than 3% and 1% respectively.

The composition gradient within the FGMs in the as-built, heat treated, and oxidized conditions were quantitatively analyzed with a JEOL JXA-8530F (JEOL Ltd., USA) field emission electron probe microanalyzer (EPMA) using wavelength dispersive spectroscopy. Compositionally similar steels were employed as standard composition references. Bulk composition measurements were performed with a probe size of 20 µm, an accelerating voltage of 20 kV, and a probe current of 50 nA. Composition measurements of the oxide layer and underlying alloy were performed using the same voltage and current but with a smaller probe size of 200 nm and step size of 500 nm. EDS mapping was used to evaluate the oxide scale and subsurface alloy for all the alloy mixtures of SS316L and IN718 in increments of 10 wt.%. Scanning electron microscopy (SEM) imaging was performed using a Scios DualBeam scanning electron microscope (FEI, Thermo Fisher Scientific Inc., USA) operating at 20 kV.

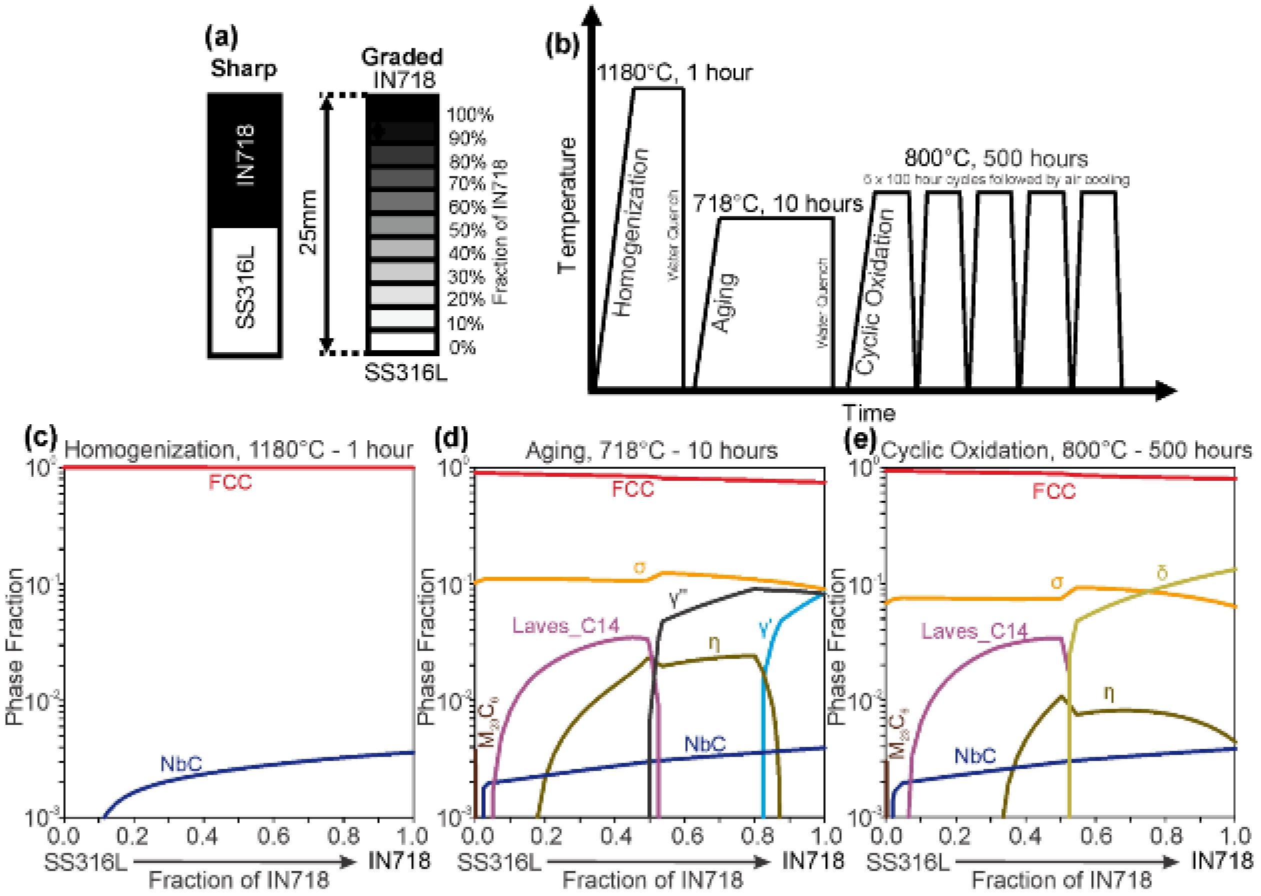

**Figure 36 – Experimental design and thermodynamic modeling of SS316L and IN718 FGMs exposed to cyclic oxidation.(a) Schematic of the sharp and graded SS316L and IN718 FGMs manufactured in this work. (b) Heat treatment schedule applied to the SS316L and IN718 FGMs. (c-e) Phase equilibria between SS316L and IN718 during homogenization at 1180°C, aging at 718°C, and cyclic oxidation 800°C. The δ phase is rejected in the calculation presented in (d) so that the γ'' could form, representing the metastable nature of the aged condition.**

**Figure 37(a)** shows the initial setup used for the cyclic oxidations study and **Figure 37(b)** shows the alumina crucibles containing the samples within the open-air tube furnace operating at 800°C. The samples were removed from the furnace every hundred hours and allowed to cool before measuring the mass gain and then promptly returned to the furnace. After completing cyclic oxidation, the samples were cold mounted, vacuum impregnated, cross sectioned, and then cold mounted again with the cross section normal to the mounting surface. **Figure 37(c)** shows the mass gain normalized for surface area as a function of time up to 500 hours. The graded FGM sample demonstrated the smallest mass gain while the sharp FGM exhibits an intermediate mass gain lying between that of the control samples of SS316L and IN718. Significant amounts of spalled oxide were found in the crucible holding the graded FGM. Based on this observation, the slower mass gain of the graded FGM may be artificially lower because some spalled oxide may have fallen outside of the crucible.

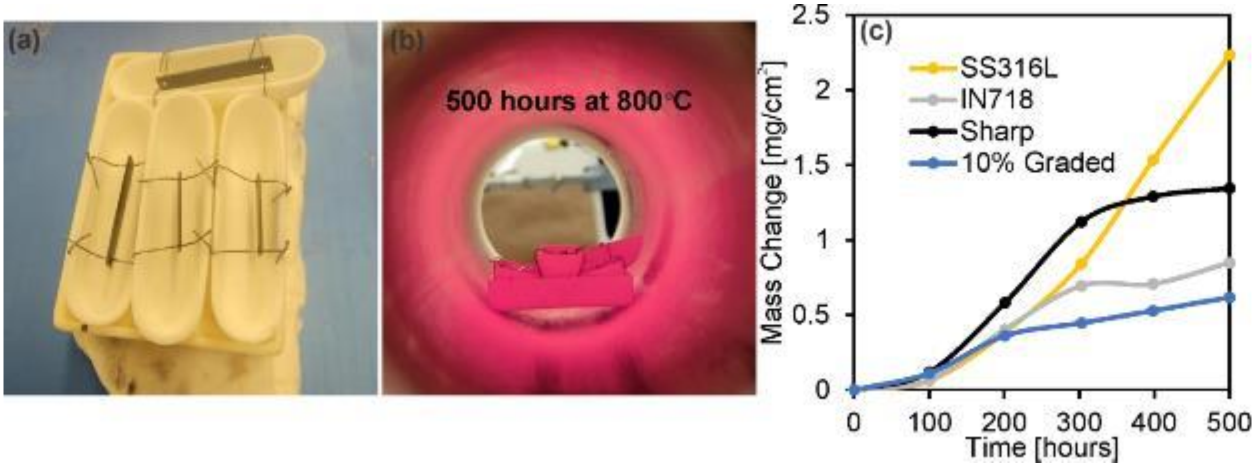

**Figure 37 – Cyclic oxidation experimental setup for the SS316L and IN718 FGMs. (a) Alumina crucibles holding the FGMs, and control samples suspended in lab air by Nickel wire. (b) Image of the experimental setup in the tube furnace operating at 800°C. (c) Normalized mass gain during the cyclic oxidation experiment.**

### 5.3 Results & Discussion

The mechanical performance of the SS316L and IN718 FGMs was evaluated before and after heat treatment using tensile testing and compared with monolithic SS316L and IN718 control samples. All the samples studied in this work were processed by DED with the same processing parameters. **Figure 38** shows the mechanical properties of the additively manufactured SS316L and IN718 FGMs and control samples before and after heat treatment. The sharp FGM in the as-built condition achieved a total elongation of 68% with a yield strength of 365 MPa and ultimate strength of 529 MPa. The mechanical performance of the sharp FGM in the as-built condition is like as-built SS316L but with less total elongation due to half the gauge length being IN718. A ductile fracture occurred within the SS316L side of the sharp FGM in the as-built condition. Necking was observed within the SS316L side of the FGM. After applying the two-step heat treatment, the sharp FGM achieved a total elongation of 67% with a yield strength of 290 MPa and ultimate strength of 544 MPa. **Figure 38(c)** shows an image of the sharp FGM in the heat-treated condition during tensile testing. Ductile failure occurred within the SS316L side of the sharp FGM after heat treatment. In both the as-built and heat-treated conditions, the sharp FGM failed in the SS316L half of the gauge length.

Although previous works have attempted a sharp transition between SS316L and IN718, they were not able to reach the >60% fracture elongation reported in this work for the as-built and heat-treated condition. These results significantly exceed the maximum previously reported fracture elongation was 20% [165]. The ductility of sharp FGM in the as-built and heat-treated conditions equals the weighted average of the fracture elongation for the SS316L and IN718 control samples tested in this work (64.5% for as-built and 54.5% for heat treated). Therefore, the mechanical performance of the sharp FGM represents the upper performance limit of a defect free SS316L and IN718 joint.

The graded FGM failed to achieve the same success as the sharp FGM. In the as-built condition, the sharp FGM reached a total elongation of just 8% with a yield strength of 341 MPa and ultimate strength of 443 MPa. The mechanical performance of the graded FGM after heat treatment was not evaluated because visible cracks could be seen on the surface of the tensile samples after machining. Although the graded FGM failed prematurely during tensile testing, it is still useful for evaluating the microstructure and oxidation resistance of the possible alloy mixtures of SS316L. The mechanical properties of the SS316L and IN718 FGMs and control samples are summarized in **Table 5** for comparison.

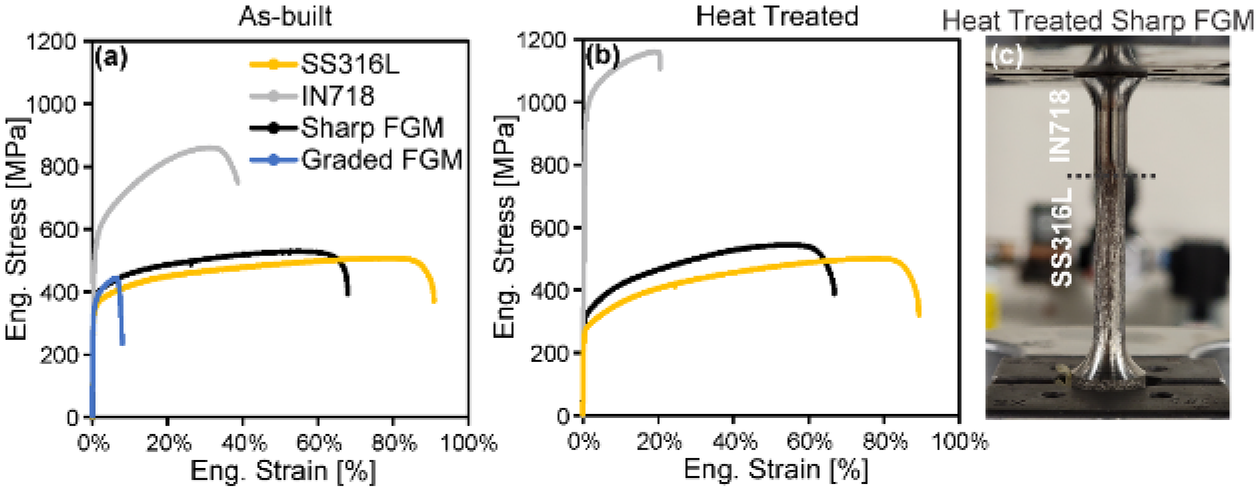

**Figure 38 – Mechanical testing of the SS316L and IN718 FGMs before and after heat treatment compared to control samples. (a) Tensile testing results for the as-built condition. (b) Tensile testing results for heat-treated conditions. (c) Image of the sharp FGM in the heat-treated condition during tensile testing.**

**Table 5 – Tensile mechanical properties of the SS316L and IN718 FGMs and control samples.**

| Sample (condition) | Tensile Properties | | |
|---|---|---|---|
| | Yield Strength [MPa] | Tensile Strength [MPa] | Fracture Elongation [%] |
| SS316L (as-built) | 322 | 509 | 90 |
| IN718 (as-built) | 490 | 860 | 39 |
| Sharp FGM (as-built) | 365 | 529 | 68 |
| Graded FGM (as-built) | 341 | 443 | 8 |
| SS316L (heat treated) | 248 | 502 | 89 |
| IN718 (heat treated) | 901 | 1162 | 20 |
| Sharp FGM (heat treated) | 290 | 544 | 67 |

**Figure 39** shows the microstructure evolution of the graded SS316L and IN718 FGM in the as-built **(a)**, heat treated **(b)**, and oxidized **(c)** conditions. Backscatter electron images of each

10 wt.% alloy mixture are provided to visualize the changing phase equilibria as a function of composition and processing. In the as-built condition **(Figure 39 (a))**, segregation from non-equilibrium solidification is observed within all the alloy mixtures. Laves phase occupies the interdendritic regions of the alloy mixtures ranging from 100-20% IN718 with the larger fractions of laves phase present in the IN718 rich mixtures. Carbides are present throughout all the alloy mixtures in the as-built condition and are likely NbC carbides. Although it is possible a small portion of the carbides in the SS316L rich alloy mixtures are $M_{23}C_6$. The as-built microstructure shown in **Figure 39 (a)** is consistent previous observations of IN718 [168] and SS316L [149, 150, 153] made with AM. Large cracks propagating along the build direction between grain boundaries are observed in the 10 wt.% IN718 alloy mixture, indicating that this composition is prone to solidification cracking. Solidification cracking within the 10 wt.% IN718 alloy mixture is responsible for the poor tensile ductility of the graded FGM.

**Figure 39(b)** shows backscatter electron images of the graded FGM after the two step (homogenization and aging) heat treatment. After heat treatment, microsegregation left over from printing is completely removed. Laves phase has also been removed from the microstructure after heat treatment because 1180°C is above the laves solvus temperature and the kinetics of laves phase formation during aging at 718°C for 10 hours are slow in the homogenized microstructure. The fraction of carbide in the heat-treated microstructure has also increased relative to the as-built condition. Lastly, large solidification cracks are still present in the 10 wt.% IN718 mixture after heat treatment.

Following heat treatment, both the FGMs and monolithic SS316L and IN718 control samples were subjected to cyclic oxidation in lab air at 800°C for 500 hours in 100 hours cycles. **Figure 37(a-b)** shows the experimental setup used to conduct the oxidation experiment and **Figure**

**37(c)** shows the normalized mass gain of each sample during oxidation. Back scatter electron images of each 10 wt.% alloy mixture after cyclic oxidation are shown in **Figure 39(c).** Following oxidation, δ phase is found in the microstructure of the alloy mixtures with 100-80 wt.% IN718 and the fraction of δ phase decreases as the amount of IN718 in the mixture decreases. Between the δ phase precipitates, areas with small γ'/γ'' can be found in the alloy mixtures with 100-80 wt.% IN718. Large coarsened γ'' particles can also be found in the alloy mixtures between 100-50 wt.% IN718. Coarsened carbines are found throughout the microstructure of all the alloy mixtures and are concentrated along the grain boundaries. Tiny amounts of σ phase with a generous size are observed throughout all the alloy mixtures. Several large σ phase precipitates are labeled in **Figure 39(c)** and are typically found along grain boundaries next to the carbides. Increased atomic mobility along grain boundaries is the most probable reason for the location of the large σ phase precipitates. The observation σ and δ formation in IN718 after long term exposure at 800°C is consistent with previous studies [169] and the behavior of the alloy mixtures with SS316L agrees well with the thermodynamic equilibrium prediction in **Figure 36(e)**.

**Figure 40** shows stitched backscatter electron images of the microstructure at the interface between SS316L and IN718 within the sharp FGM in the as-built **(a)**, heat treated **(b)**, and oxidized **(c)** conditions. Cracks are not observed within the sharp FGM in any of the conditions and the microstructure is similar in appearance to that of the graded FGM with 10 wt.% steps, just with a smooth transition over the distance of 0.75-1 mm. The sharp FGM avoids the cracking encountered within the graded FGM by deposition IN718 directly on top of SS316L without an interlayer. We attribute the successful defect free sharp FGM to careful control of the processing environment and allowing the build to cool for 30 seconds while the powder feeders switch between feedstock materials.

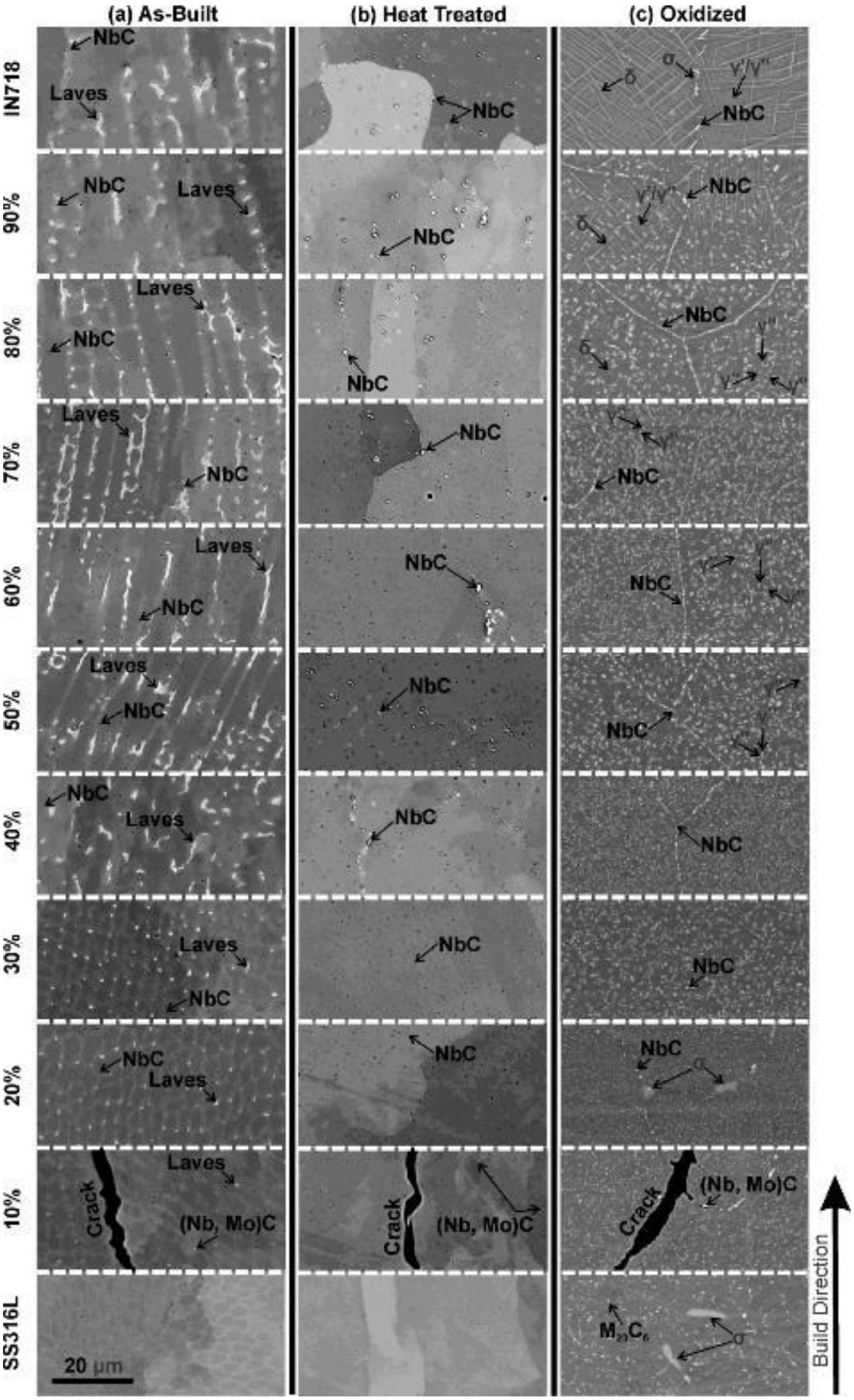

**Figure 39 – Backscatter electron SEM images of the graded SS316L and IN718 FGM in the as-built (a), heat treated (b), and oxidized (c) conditions in increments of 10 wt.% IN718.**

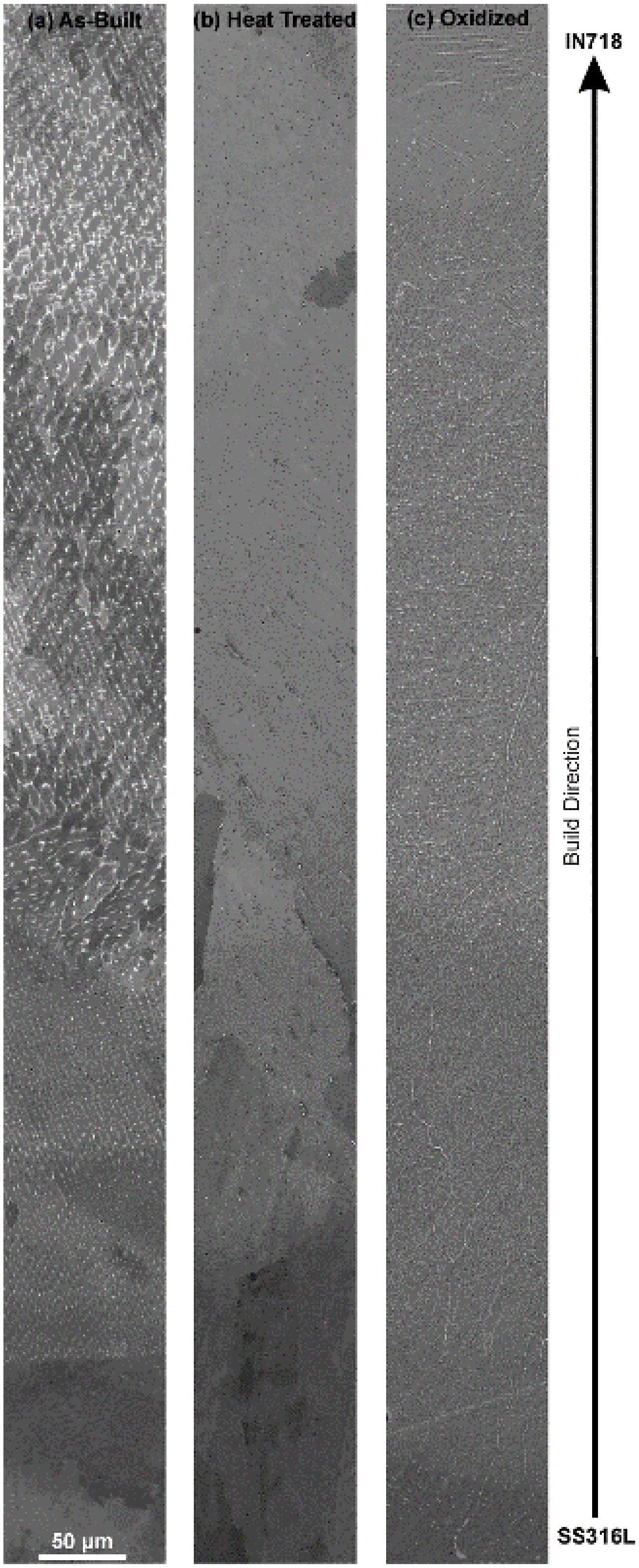

**Figure 40 – Backscatter electron SEM images of the sharp SS316L and IN718 FGM in the as-built (a), heat treated (b), and oxidized (c) conditions.**

EPMA measurements of the composition gradient within the sharp and graded FGMs was done to evaluate the as-built condition and investigate changes in the composition gradient after heat treatment and cyclic oxidation. The measured compostion gradient in the as-built, heat treated, and oxidized condition for the sharp FGM is shown in **Figure 41(a)** and for the graded FGM in **Figure 41(b)**. The diultion zone between SS316L and IN718 within the sharp FGM covers a distance of 0.75-1 mm and did not significantly change during heat treatment or cyclic oxidation. Based on the layer height used for printing (0.254 mm) and the EPMA measurement in **Figure 41(b)**, SS316L was remelted and mixed with the IN718, creating a dilution effect over 3-4 layers. Since the graded FGM streched out the compostion gradient into steps of 10 wt.%, no significant changes to the bulk composition gradient or dilution effects were observed in any of the condtions.

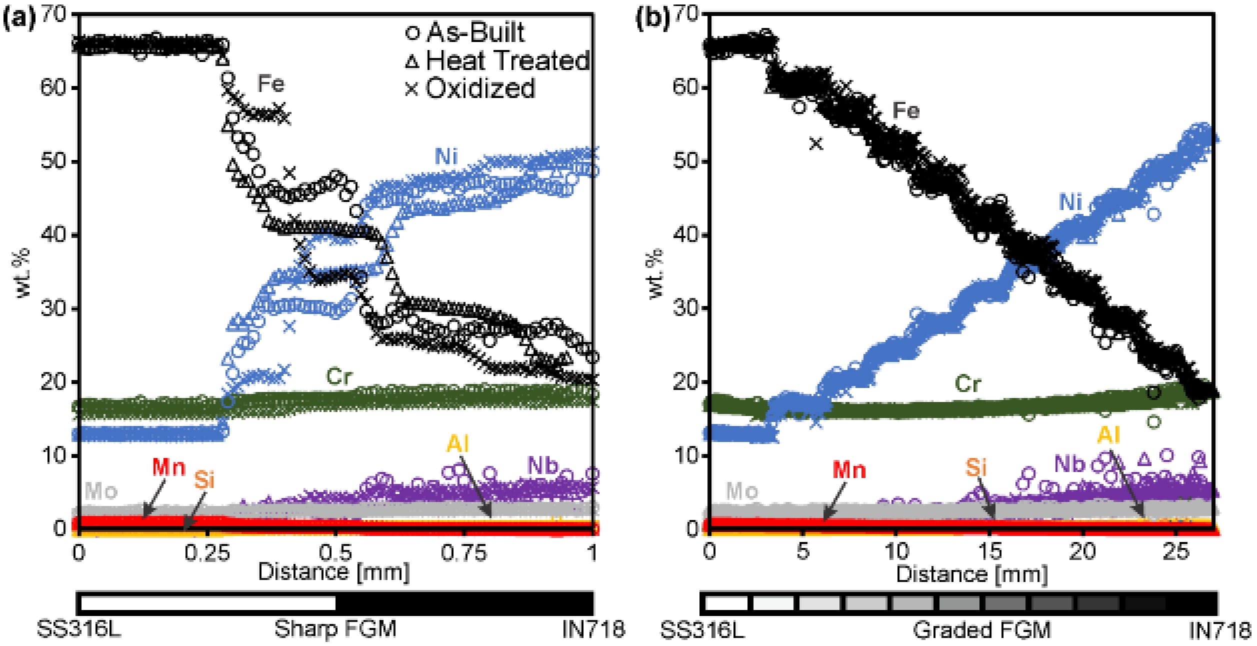

**Figure 41 – EPMA measurement of composition gradient within the SS316L and IN718 FGMs (a) the sharp transition and (b) the functionally graded transition.**

**Figure 42(a)** shows the microhardness in the as-built, heat treated, and oxidized conditions for the graded FGM in the as-built, heat treated, and oxidized conditions. After heat treatment, the microhardness of IN718 nearly doubles from 282 HV (as-built IN718) to 450HV (heat treated

IN718) due to the precipitation of γ'/γ" during aging. The microhardness of SS316L is slightly reduced from 202 HV (as-built SS316L) to 190HV (heat treated SS316L) after heat treatment due to relief of residual stress and grain coarsening during heat treatment. In the oxidized condition, the microhardness of IN718 is 328 HV (oxidized IN718), significantly lower than the heat-treated condition but still higher than the as-built condition. Coarsening of γ'/γ" during oxidation and precipitation of δ phase are responsible for the reduced hardness of IN718 after cyclic oxidation. The hardness of SS316L after cyclic oxidation is 182 HV (oxidized SS316L), which is slightly higher than after heat treatment as a result carbide and σ phase precipitation but still lower than the as build condition. At the interface between SS316L and IN718 within the sharp FGM, a smooth transition in microhardness is observed in all three conditions.

The microhardness gradient of the graded FGM is shown in **Figure 42(b)** for the as-built, oxidized, and heat-treated condition. In all three conditions, the microhardness gradient gradually increases with increasing content of IN718. After heat treatment, the hardness of the IN718 rich mixtures (60-100 wt.% IN718) increases significantly compared to the as-built condition due to the precipitation of γ'/ γ" during aging. This observation is in good agreement with the predicted thermodynamic equilibria shown **Figure 36(d)** for aging at 718°C where the predicted stability range of γ' and γ" is between 80-100 wt.% IN718 and 50-100 wt.% IN718, respectively. After oxidation, the microhardness of the IN718 rich mixtures decreases significantly due to coarsening of γ'/ γ" and precipitation of δ phase. On the other hand, the microhardness of the SS316L rich mixtures (0-60 wt.% IN718) remains about the same after heat treatment and cyclic oxidation.

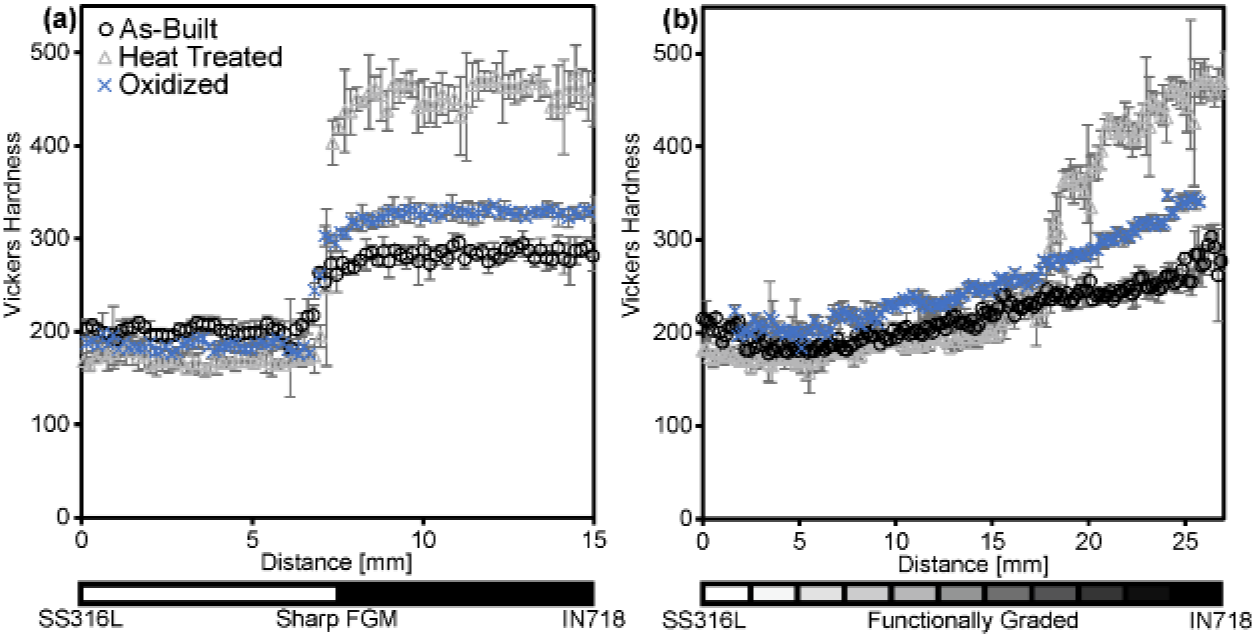

**Figure 42 – Vickers microhardness mapping of the SS316L and IN718 FGMs in the as-built, heat treated, and oxidized condition for (a) the sharp transition and (b) the functionally graded transition.**

Following cyclic oxidation, the oxide layer formed on each 10 wt.% IN718 composition blocks in the graded FGM was analyzed using EDS mapping. **Figure 43** shows the EDS maps of the oxide layer and subsurface alloy within each composition block. All the intensity maps presented in **Figure 43** are normalized so that they can be compared directly to each other. Spinel, formed during the initial stages of oxidation, was still attached to the SS316L but was not observed on any other alloy mixtures. Careful analysis of the SEM images and EDS maps shows that IN718 and SS316L maintained the integrity of their external $Cr_2O_3$ oxide better than the other alloy mixtures. Internal oxides ($Al_2O_3$ and $TiO_2$) are observed in the IN718 rich mixtures because the concentration of Al and Ti is higher in IN718 than SS316L. Carbides are observed throughout all the alloy mixtures with some forming in the depletion zone beneath the oxide scale. The Chromium rich sigma phase can be identified in the EDS maps for both SS316L and IN718. Internal attack along grain boundaries can be found throughout the graded FGM as shown in the EDS maps for SS316L and 90 wt.% IN718.

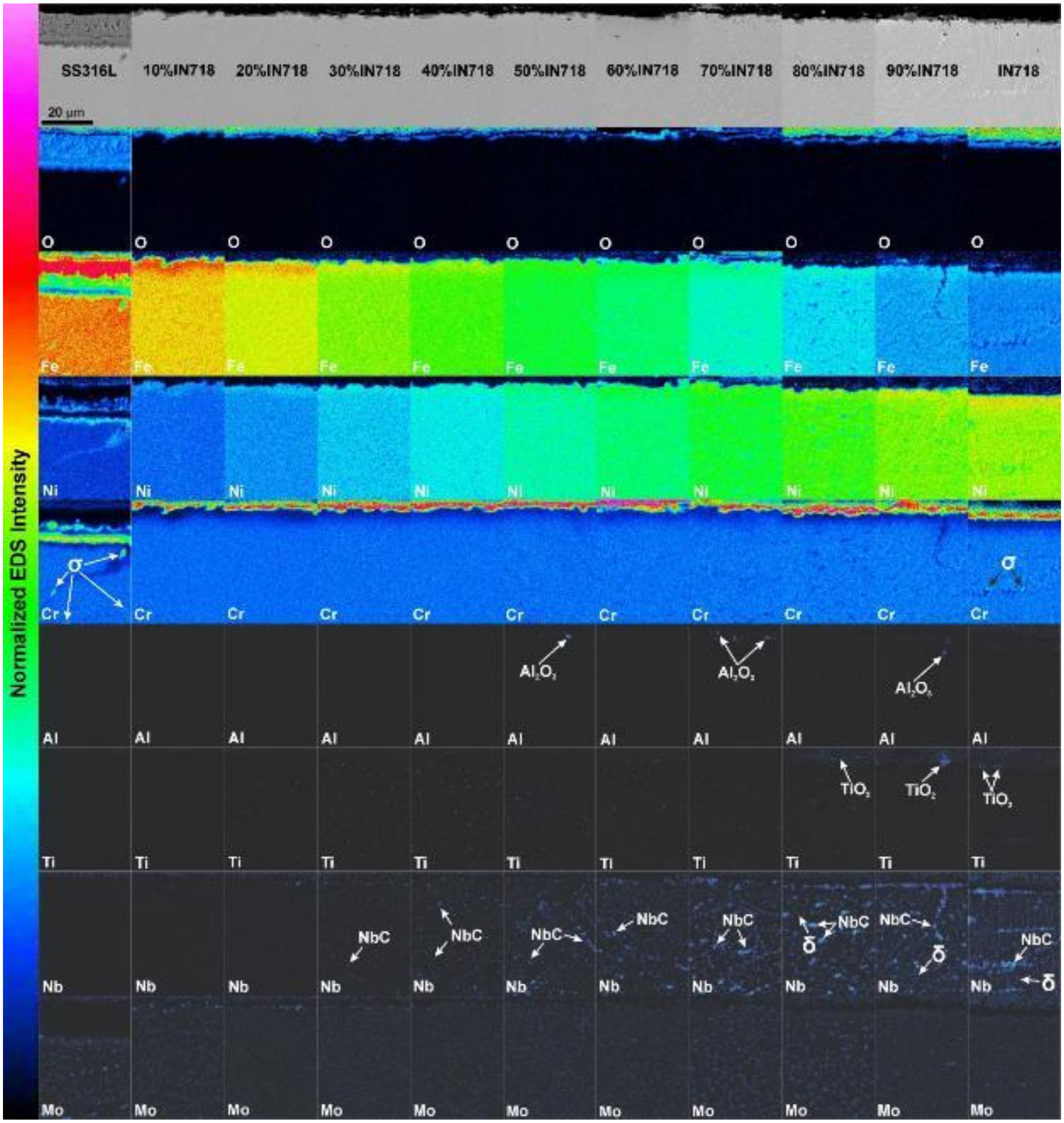

**Figure 43 – EDS mapping of the oxide scale on the SS316L and IN718 mixtures after cyclic oxidation at 800°C for 500 hours.The EDS intensity scale is normalized so that maps can be compared relative to one another.**

EPMA line measurements of the external oxide and subsurface alloy were done to quantitatively analyze the internal oxidation and depletion of chromium beneath the oxide scale.

**Figure 44** presents the results of the EPMA measurement for each of the alloy mixtures. Three separate line scans using a probe size of 200 nm with a 500 nm step size were averaged to generate the average concentration profiles presented in **Figure 44**. The concentration profiles are separated into plots for each individual element so that the elemental concentration profiles for each alloy mixture can be easily compared to each other. Several interesting observations can be drawn from the elemental concentration profiles presented in **Figure 44**. First, the severity of depletion of chromium beneath the oxide scale is consistent across all the alloy mixtures. Second, manganese is concentrated within the $Cr_2O_3$ oxide. Beneath the $Cr_2O_3$ oxide scale, there is a consistent sequence in which internal oxides form throughout the alloy mixtures. $TiO_2$ and $SiO_2$ are found just below the external $Cr_2O_3$ oxide, followed by $Al_2O_3$. Lastly, enrichment of Niobium and Molybdenum, caused by the formation of carbides and delta phase, is found in the depletion zone beneath the oxide scale.

The elemental concentration profiles presented in **Figure 44** show that the alloy mixtures of the SS316L and IN718 are consistent. Since the chromium concentration in SS316L and IN718 is within the same range (16.5-21 wt.%), external $Cr_2O_3$ oxide is formed by all the alloy mixtures. Poorer external oxide integrity is observed in the alloy mixtures compared with SS316L and IN718. One explanation for this is increased thermal stresses brought on by changes in thermal expansion. The biggest difference in the oxidation behavior among the alloy mixtures is the tendency to for more internal $Al_2O_3$ and $TiO_2$ oxides as the content of IN718 increases.

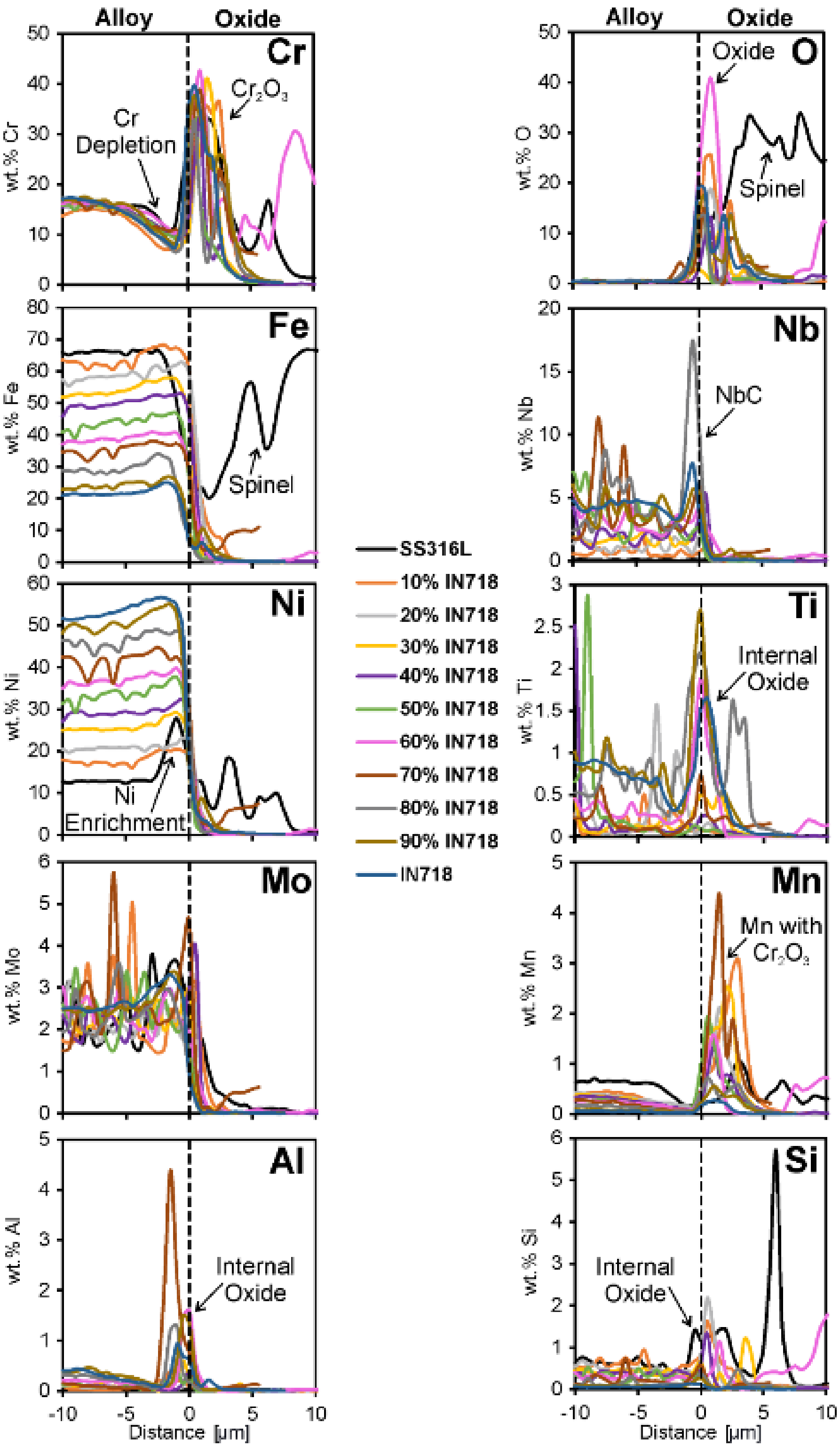

**Figure 44 – Wavelength dispersive spectroscopy EPMA measurements of the oxide layer and subsurface alloy for each of the 10% IN718 and SS316L alloy mixtures. The results for each element are plotted on top of each other to easily compare the oxide layers formed on the different alloy**

To further analyze the oxidation behavior within the SS316L and IN718 FGMs, the Gibbs free energy of oxide formation was calculated for several elemental oxides that were observed in the experimental results. The oxide formation energy of $Al_2O_3$, $TiO_2$, and $Cr_2O_3$ with reference to the pure elements under 1 atm pressure is shown in **Figure 45(a)** as a function of temperature. Using the approach for calculating the modified Ellingham diagrams for alloys described by Epifano et al. [170], the alloying effect on the Gibbs free energy of oxide formation was calculated for the alloy mixtures of SS316L and IN718 at 800°C according the following equation:

$$RTln(pO_2) = \Delta G^0 - RTln\left(a^{\frac{2c}{b}}\right) \tag{5-1}$$

where $\Delta G^0$ is the Gibbs free energy of oxide formation for the pure element, $a$ is the activity of the element in the alloy and $\frac{2c}{b}$ comes from the reaction coefficients. Coefficients $b$ and $c$ can be found from the generalized form of the oxidation reaction normalized for 1 mole of $O_2$:

$$\frac{2c}{b}Me + O_2 \rightleftharpoons \frac{2}{b}\, Me_cO_b \tag{5-2}$$

Where $Me$ is the element and $b$ and $c$ are the coefficients needed to balance the reaction. The elemental activity at 800°C in each alloy was calculated using a material to material calculation in Thermo-Calc software [76]. The stable phase of each element at the given temperature of interest must be set as the reference state to calculate the elemental activity in the alloy. **Figure 45(b)** shows the elemental activity at 800°C within each alloy mixture of SS316L and IN718. Using the elemental activity within each alloy, the modified the Gibbs free energy of oxide formation (RT*ln*(*p*$O_2$)) of $Al_2O_3$, $TiO_2$, and $Cr_2O_3$ at 800°C was calculated for each alloy mixture, as shown in **Figure 45(c)**. The results of this calculation show that the driving force for oxidation, or in other words the energy released during oxidation is reduced for $Al_2O_3$, $TiO_2$, and $Cr_2O_3$ when considering the alloying effects.

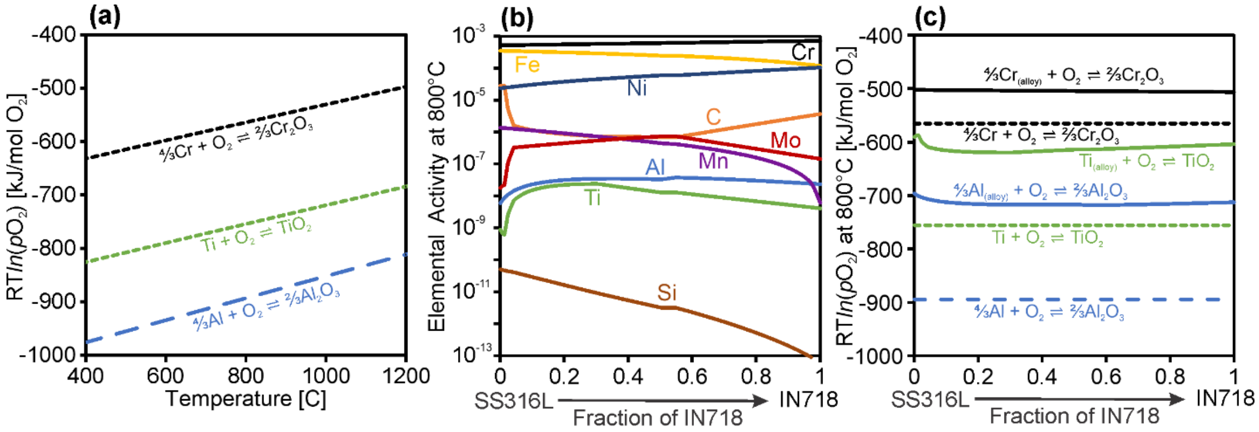

**Figure 45 – Prediction of the free energy of oxide formation in IN718 and SS316L. (a) Gibbs gree energy of oxide formation form elements as a function of temperature. (b) Elemental activity at 800°C within the alloy mixtures of SS316L and IN718. (c) Gibbs free energy of oxide formation at 800 °C in the alloy in comparison to the pure element.**

From the EPMA measurements shown in **Figure 44**, we know that the sequence of the dominate oxides is $Cr_2O_3$, $TiO_2$, and the $Al_2O_3$ going from the external to internal oxide scale. This sequence corresponds to the lowest to highest oxygen partial pressures which, matched with the predicted Gibbs free energy of oxide formation shown in **Figure 45**. Although considering the alloys impact on the Gibbs free energy of oxide formation does not change the predicted sequence of the oxides, this is not always the case for all alloy systems [170]. Overall, the predicted Gibbs free energy of oxide formation matches well with the experimental result that the oxidation behavior of the alloy mixtures is consistent. The thermodynamic model for oxidation shown in **Figure 45** is useful for predicting changes in the oxidation behavior withing the mixtures of dissimilar alloys and could be used to guide the design of FGMs operating in high-temperature oxidizing environments. Although kinetic factors are not considered in this model, this methodology can be applied to analyze the thermodynamic impact on oxidation within FGMs.

### 5.4 Chapter Summary & Conclusion

The results presented here represent the first instance of an SS316L and IN718 FGM achieving a fracture elongation greater than 60% in both the as-built and heat-treated conditions. These findings demonstrate the feasibility of applying a typical homogenization and aging heat treatment for IN718 without compromising the mechanical performance of the SS316L within the same joint. The sharp SS316L and IN718 FGM represents the upper limit of mechanical performance, surpassing the performance based on the rule of mixtures. The improvement in mechanical properties observed in the sharp SS316L and IN718 FGM can be attributed to three key factors: stringent control of oxygen levels (<5 ppm) during printing, calibration of processing parameters, and effective minimization of dilution effects at the material transition.

This chapter delves into unfamiliar territory by investigating the effects of cyclic oxidation on SS316L and IN718 FGMs exposed to lab air at 800°C for 500 hours. Over this prolonged high-temperature exposure, the optimal microstructure achieved after heat treatment was compromised as detrimental phases ($\delta$ and $\sigma$) precipitated at the expense of desirable metastable $\gamma'/\gamma''$ strengthening precipitates. The experimental results align well with predicted thermodynamic phase equilibria. For evaluating the oxidation performance of SS316L and IN718, EDS mapping and EPMA measurements were employed. While all the alloy mixtures of SS316L and IN718 formed an external $Cr_2O_3$ oxide scale, the integrity of the external oxide proved inferior when compared to the SS316L and IN718 control samples.

By shedding light on the oxidation performance of the SS316L and IN718 mixtures for the first time, this study fills an important gap in the existing literature. Furthermore, our research reports a notable improvement in the mechanical performance of SS316L and IN718 FGMs. The findings and insights gained from this work contribute to the field of FGMs operating in extreme environments, highlighting their considerable potential.

The outcomes of this study provide novel experimental data and pave the way for future developments in the design and application of functionally graded materials composed of SS316L and IN718. As researchers continue to explore the capabilities of FGMs, their potential in various demanding settings will be further realized.

# 6.0 Executive Summary: Advances in Additively Manufactured Functionally Graded Materials: Microstructure Modeling, Alloy Development, and Performance in Extreme Environments

This Ph.D. dissertation presents novel research in additive manufacturing (AM) focusing on functionally graded materials (FGMs) and alloy development. The dissertation comprises of four main chapters, each contributing essential insights to the development and understanding of the process-structure-property relationships that govern the behavior of FGMs made with AM. The key conclusions from each chapter are summarized below.

Chapter 2.0 discusses advances in modeling the microstructure of AM materials and the application to FGMs. Three significant contributions are highlighted: A coupled processing and microstructure model that predicts solidification cracking susceptibility based on processing parameters and composition variations. An integrated experimental and computational approach to predict location-specific changes in solidification cracking susceptibility due to temperature history and composition variations. A framework for predicting the kinetic behavior of FGMs during heat treatment and high-temperature operation.

Chapter 3.0 reports on the successful fabrication of an FGM comprising SS316L and HSLA-100 steels with location-specific properties such as magnetism, corrosion resistance, strength, and ductility. Then using high-throughput experimental techniques, a new steel alloy, #40HSLA steel, is discovered, exhibiting microsegregation-aided transformation-induced plasticity (TRIP) and twinning-induced plasticity (TWIP) effects in the as-built condition. This alloy design pathway eliminates the need for heat treatment and presents promising avenues for further AM-based alloy design.

Chapter 4.0 demonstrates the capability of DED to rapidly fabricate alloys with different compositions, leading to the discovery of a new alloy with a refined as-built microstructure by adding 77 wt.% IN718 to SS316L. The factors contributing to grain refinement in this alloy are identified, highlighting the importance of microstructure engineering in AM alloy development.

Chapter 5.0 investigates the mechanical performance and oxidation behavior of SS316L and IN718 FGMs. The research highlights an advancement in manufacturing and post-processing of SS316L and IN718 FGMs by achieving fracture elongation greater than 60% in both as-built and heat-treated conditions, surpassing the expected mechanical performance based on the rule of mixtures. This study also explores the effects of cyclic oxidation on SS316L and IN718 FGMs, revealing valuable insights for FGMs operating in extreme environments.

The overall impact of this dissertation centers on its contributions to the design and analysis of FGMs made with AM. The development of novel modeling techniques, successful alloy discoveries, and comprehensive microstructural analyses demonstrate the potential of FGMs. This research marks an advancement in the field of FGMs, opening doors to further innovations in alloy design and advanced manufacturing.

## 6.1 Future Work

- Integration of processing and microstructure models are necessary for the development of FGMs. Although chapter 2.1 makes a significant advance by predicting the impact of AM processing parameters and composition on solidification cracking susceptibility. This work represents the limit of what is possible using current models. Further improvement of models (Scheil & DICTRA) for non-equilibrium solidification is necessary to realize the full potential of this approach.

- Chapter 2.3 discusses an innovative approach called diffusion coupled FGMs for modeling the diffusion in complex composition gradients during heat treatment and high-temperature operation. Although this chapter demonstrates this approach's potential, further research, and review of the existing literature on diffusion couples is required to realize its vision.

- The discovery of microsegregation-aided transformation and twining induced plasticity (TRIP and TWIP) in low-manganese steel processed by directed energy deposition is presented in chapter 3.0. This chapter presents one of the significant contributions of this dissertation, by revealing a new pathway for designing innovative next-generation alloys for AM that take advantage of microsegregation to improve material properties without heat treatment. Future work should aim to use computational tools to design new alloys that take advantage of microsegregation in the as-built microstructure of AM alloys.

- Chapter 4.0 reports on an interesting grain refinement phenomenon observed during homogenization of SS316L and IN718 FGMs. Potential explanations such as residual stress induced recrystallization and alloy entropy are investigated using directed energy deposition of different alloy mixtures. Although a definitive explanation of the observed grain refinement is not provided, future research will aim to reveal the underlying mechanisms.

- Chapter 5.0 demonstrates an advance in the field of FGMs by achieving a defect free SS316L and IN718 FGM with a fracture elongation of greater than 60% in both the as-built and heat-treated conditions. Additional investigation of the microstructural stability and oxidation performance of SS316L and IN718 yielded valuable data. Future work in this area should focus on FGMs combining high-temperature Ni-based superalloys alloys with high conductivity precipitations strengthened copper alloys. NASA has provided follow on funding to the Physical Metallurgy and Materials Design Laboratory at the University of Pittsburgh to investigate the manufacturability and process optimization of FGMs combining Ni-based superalloys and precipitation strengthened copper alloys with potential applications in rocket engines.

# Appendix A Appendices and Supplemental Content

Increased entropy can result in sluggish diffusion. However, this rule of thumb does not always apply and should be analyzed on a case-by-case basis. To investigate the possibility that sluggish diffusion caused the grain refinement phenomenon observed in this work, the diffusion matrix was calculated with Themo-Calc software version 2021b using the TCNI11 and MOBNI5 databases. Tables S1-3 show the diffusion matrices calculated for the three different alloy mixtures investigated in this work at the homogenization temperature of 1180°C with Fe as the dependent element. Tables S4-6 show the diffusion matrices calculated for the three different alloy mixtures investigated in this work at the homogenization temperature of 1180°C with Ni as the dependent element. Careful analysis of the tables reveals that there is a slight difference in the bulk diffusivity of the three alloys studied in this work. Therefore, the grain refinement phenomenon discovered in this work cannot be explained by sluggish diffusion caused by increased entropy. However, a higher level of grain refinement was observed in the alloy with 77 wt.% IN718 after homogenization. This may be related to increased solute concentration during recrystallization. More research is needed to investigate the cause of grain refinement during the homogenization of additively manufactured materials.

## Table 6 – Fe-dependent diffusion matrix calculated for alloy with 77 wt.% IN718 showing diffusivity in m$^2$/s.

| k / j | Al | C | Cr | Fe | Mn | Mo | Nb | Ni | Si | Ti |
|---|---|---|---|---|---|---|---|---|---|---|
| **Al** | 4.445E-14 | -5.937E-16 | 4.969E-16 | — | 2.302E-16 | 4.218E-16 | 5.021E-16 | -5.197E-16 | 2.720E-15 | 6.349E-16 |
| **C** | -1.268E-13 | 7.917E-11 | -1.360E-13 | — | -5.591E-14 | -2.135E-13 | -5.405E-13 | 1.022E-13 | 3.944E-13 | -3.211E-13 |
| **Cr** | 8.093E-15 | -1.104E-14 | 2.007E-14 | — | 1.560E-15 | -7.462E-16 | 7.932E-15 | 2.225E-15 | -4.550E-15 | 1.357E-14 |
| **Fe** | -2.603E-14 | 1.314E-14 | -1.922E-14 | — | -1.904E-14 | -1.105E-14 | -2.235E-14 | -9.203E-15 | -1.894E-14 | -2.533E-14 |
| **Mn** | 4.420E-17 | -5.763E-17 | 3.031E-17 | — | 2.764E-14 | 2.595E-17 | 1.231E-16 | -8.649E-17 | -1.075E-16 | 1.969E-16 |
| **Mo** | -4.001E-16 | -1.260E-15 | -6.628E-16 | — | -5.516E-16 | 9.812E-15 | -1.091E-15 | 2.614E-16 | 1.257E-15 | -6.403E-16 |
| **Nb** | 4.143E-15 | -2.982E-14 | 4.096E-15 | — | 3.068E-15 | -8.413E-17 | 4.407E-14 | -6.670E-15 | 2.536E-14 | 7.500E-15 |
| **Ni** | -3.190E-14 | 3.342E-14 | -6.427E-15 | — | -1.402E-14 | 6.328E-16 | -3.122E-14 | 1.652E-14 | -4.658E-14 | -4.504E-14 |
| **Si** | 2.802E-16 | 2.644E-16 | -2.673E-17 | — | -4.266E-17 | 1.208E-16 | 2.545E-16 | -1.418E-16 | 3.499E-14 | 2.503E-16 |
| **Ti** | 1.322E-15 | -4.055E-15 | 1.643E-15 | — | 1.156E-15 | 8.654E-16 | 1.787E-15 | -2.385E-15 | 5.854E-15 | 4.886E-14 |

## Table 7 – Fe-dependent diffusion matrix calculated for alloy with 62 wt.% IN718 showing diffusivity in m2/s.

| k / j | Al | C | Cr | Fe | Mn | Mo | Nb | Ni | Si | Ti |
|---|---|---|---|---|---|---|---|---|---|---|
| **Al** | 4.664E-14 | -4.557E-16 | 4.306E-16 | — | 1.849E-16 | 2.952E-16 | 3.695E-16 | -4.807E-16 | 2.337E-15 | 4.910E-16 |
| **C** | -9.943E-14 | 8.702E-11 | -1.255E-13 | — | -4.713E-14 | -1.892E-13 | -5.028E-13 | 1.028E-13 | 3.622E-13 | -3.231E-13 |
| **Cr** | 6.820E-15 | -1.143E-14 | 1.873E-14 | — | 1.605E-15 | -6.394E-16 | 6.353E-15 | 1.432E-15 | -3.071E-15 | 1.125E-14 |
| **Fe** | -2.798E-14 | 1.432E-14 | -1.776E-14 | — | -1.685E-14 | -1.062E-14 | -2.365E-14 | -7.193E-15 | -2.053E-14 | -2.803E-14 |
| **Mn** | 6.988E-19 | -5.928E-17 | 2.740E-17 | — | 2.309E-14 | 1.890E-17 | 1.125E-16 | -1.320E-16 | -1.929E-16 | 1.911E-16 |
| **Mo** | -4.423E-16 | -1.390E-15 | -5.082E-16 | — | -3.608E-16 | 1.015E-14 | -9.885E-16 | 2.641E-16 | 1.446E-15 | -5.187E-16 |
| **Nb** | 2.983E-15 | -2.559E-14 | 3.382E-15 | — | 2.557E-15 | -2.843E-16 | 4.311E-14 | -5.425E-15 | 2.065E-14 | 5.675E-15 |
| **Ni** | -2.928E-14 | 2.813E-14 | -5.635E-15 | — | -1.114E-14 | 3.296E-16 | -2.686E-14 | 1.348E-14 | -3.837E-14 | -3.794E-14 |
| **Si** | 2.194E-16 | 2.007E-16 | -1.146E-17 | — | -2.871E-17 | 9.220E-17 | 1.916E-16 | -1.036E-16 | 3.298E-14 | 1.894E-16 |
| **Ti** | 1.036E-15 | -3.733E-15 | 1.342E-15 | — | 9.438E-16 | 6.666E-16 | 1.369E-15 | -1.841E-15 | 4.749E-15 | 4.870E-14 |

## Table 8 – Fe-dependent diffusion matrix calculated for alloy with 47 wt.% IN718 showing diffusivity in m2/s.

| k / j | Al | C | Cr | Fe | Mn | Mo | Nb | Ni | Si | Ti |
|---|---|---|---|---|---|---|---|---|---|---|
| **Al** | 4.868E-14 | -3.231E-16 | 3.509E-16 | — | 1.341E-16 | 1.952E-16 | 2.484E-16 | -4.058E-16 | 1.873E-15 | 3.514E-16 |
| **C** | -7.378E-14 | 9.519E-11 | -1.115E-13 | — | -3.890E-14 | -1.601E-13 | -4.466E-13 | 9.521E-14 | 3.129E-13 | -3.079E-13 |
| **Cr** | 4.910E-15 | -1.112E-14 | 1.675E-14 | — | 1.369E-15 | -4.181E-16 | 4.389E-15 | 7.635E-16 | -2.235E-15 | 8.336E-15 |
| **Fe** | -3.041E-14 | 1.462E-14 | -1.594E-14 | — | -1.458E-14 | -1.051E-14 | -2.519E-14 | -5.789E-15 | -2.123E-14 | -3.064E-14 |
| **Mn** | -8.077E-17 | -5.374E-17 | 1.772E-17 | — | 1.924E-14 | 5.948E-18 | 6.371E-17 | -1.733E-16 | -2.797E-16 | 1.313E-16 |
| **Mo** | -4.805E-16 | -1.517E-15 | -3.450E-16 | — | -2.072E-16 | 1.054E-14 | -9.049E-16 | 2.623E-16 | 1.565E-15 | -4.287E-16 |
| **Nb** | 1.929E-15 | -2.063E-14 | 2.643E-15 | — | 1.969E-15 | -3.256E-16 | 4.246E-14 | -4.145E-15 | 1.573E-14 | 3.999E-15 |
| **Ni** | -2.546E-14 | 2.207E-14 | -4.508E-15 | — | -8.616E-15 | -4.589E-17 | -2.217E-14 | 1.089E-14 | -3.010E-14 | -3.051E-14 |
| **Si** | 1.589E-16 | 1.417E-16 | -3.819E-18 | — | -2.018E-17 | 6.458E-17 | 1.336E-16 | -7.249E-17 | 3.108E-14 | 1.328E-16 |
| **Ti** | 7.454E-16 | -3.188E-15 | 1.028E-15 | — | 7.120E-16 | 4.893E-16 | 9.769E-16 | -1.330E-15 | 3.600E-15 | 4.863E-14 |

**Table 9 – Ni-dependent diffusion matrix calculated for alloy with 77 wt.% IN718 showing diffusivity in m2/s.**

| k / j | Al | C | Cr | Fe | Mn | Mo | Nb | Ni | Si | Ti |
|---|---|---|---|---|---|---|---|---|---|---|
| **Al** | 4.494E-14 | -5.944E-16 | 1.016E-15 | 5.191E-16 | 7.493E-16 | 9.416E-16 | 1.022E-15 | — | 3.237E-15 | 1.154E-15 |
| **C** | -2.288E-13 | 7.911E-11 | -2.379E-13 | -1.020E-13 | -1.579E-13 | -3.154E-13 | -6.420E-13 | — | 2.921E-13 | -4.225E-13 |
| **Cr** | 5.877E-15 | -1.105E-14 | 1.786E-14 | -2.227E-15 | -6.679E-16 | -2.975E-15 | 5.718E-15 | — | -6.779E-15 | 1.137E-14 |
| **Fe** | -1.678E-14 | 1.311E-14 | -1.000E-14 | 9.228E-15 | -9.823E-15 | -1.823E-15 | -1.311E-14 | — | -9.672E-15 | -1.607E-14 |
| **Mn** | 1.313E-16 | -5.806E-17 | 1.171E-16 | 8.660E-17 | 2.776E-14 | 1.127E-16 | 2.104E-16 | — | -2.055E-17 | 2.843E-16 |
| **Mo** | -6.596E-16 | -1.260E-15 | -9.245E-16 | -2.607E-16 | -8.138E-16 | 9.548E-15 | -1.352E-15 | — | 9.954E-16 | -9.014E-16 |
| **Nb** | 1.082E-14 | -2.982E-14 | 1.077E-14 | 6.674E-15 | 9.742E-15 | 6.592E-15 | 5.075E-14 | — | 3.204E-14 | 1.418E-14 |
| **Ni** | -4.847E-14 | 3.345E-14 | -2.298E-14 | -1.655E-14 | -3.059E-14 | -1.591E-14 | -4.782E-14 | — | -6.319E-14 | -6.165E-14 |
| **Si** | 4.223E-16 | 2.645E-16 | 1.151E-16 | 1.420E-16 | 9.923E-17 | 2.628E-16 | 3.966E-16 | — | 3.514E-14 | 3.924E-16 |
| **Ti** | 3.710E-15 | -4.051E-15 | 4.030E-15 | 2.387E-15 | 3.543E-15 | 3.253E-15 | 4.176E-15 | — | 8.243E-15 | 5.125E-14 |

**Table 10 – Ni-dependent diffusion matrix calculated for alloy with 62 wt.% IN718 showing diffusivity in m2/s.**

| k / j | Al | C | Cr | Fe | Mn | Mo | Nb | Ni | Si | Ti |
|---|---|---|---|---|---|---|---|---|---|---|
| **Al** | 4.710E-14 | -4.562E-16 | 9.108E-16 | 4.803E-16 | 6.653E-16 | 7.759E-16 | 8.503E-16 | — | 2.817E-15 | 9.716E-16 |
| **C** | -2.022E-13 | 8.696E-11 | -2.281E-13 | -1.027E-13 | -1.498E-13 | -2.918E-13 | -6.050E-13 | — | 2.593E-13 | -4.254E-13 |
| **Cr** | 5.401E-15 | -1.144E-14 | 1.731E-14 | -1.434E-15 | 1.733E-16 | -2.076E-15 | 4.934E-15 | — | -4.503E-15 | 9.836E-15 |
| **Fe** | -2.075E-14 | 1.430E-14 | -1.056E-14 | 7.211E-15 | -9.653E-15 | -3.414E-15 | -1.643E-14 | — | -1.329E-14 | -2.080E-14 |
| **Mn** | 1.334E-16 | -5.974E-17 | 1.597E-16 | 1.321E-16 | 2.325E-14 | 1.511E-16 | 2.453E-16 | — | -6.044E-17 | 3.241E-16 |
| **Mo** | -7.050E-16 | -1.390E-15 | -7.727E-16 | -2.637E-16 | -6.255E-16 | 9.880E-15 | -1.252E-15 | — | 1.182E-15 | -7.826E-16 |
| **Nb** | 8.416E-15 | -2.559E-14 | 8.810E-15 | 5.427E-15 | 7.985E-15 | 5.144E-15 | 4.854E-14 | — | 2.609E-14 | 1.111E-14 |
| **Ni** | -4.280E-14 | 2.816E-14 | -1.914E-14 | -1.350E-14 | -2.466E-14 | -1.317E-14 | -4.040E-14 | — | -5.192E-14 | -5.150E-14 |
| **Si** | 3.231E-16 | 2.008E-16 | 9.217E-17 | 1.037E-16 | 7.495E-17 | 1.959E-16 | 2.954E-16 | — | 3.310E-14 | 2.932E-16 |
| **Ti** | 2.879E-15 | -3.731E-15 | 3.185E-15 | 1.842E-15 | 2.786E-15 | 2.509E-15 | 3.212E-15 | — | 6.593E-15 | 5.055E-14 |

**Table 11 – Ni-dependent diffusion matrix calculated for alloy with 47 wt.% IN718 showing diffusivity in m2/s.**

| k / j | Al | C | Cr | Fe | Mn | Mo | Nb | Ni | Si | Ti |
|---|---|---|---|---|---|---|---|---|---|---|
| **Al** | 4.907E-14 | -3.235E-16 | 7.565E-16 | 4.057E-16 | 5.399E-16 | 6.011E-16 | 6.544E-16 | — | 2.278E-15 | 7.573E-16 |
| **C** | -1.690E-13 | 9.514E-11 | -2.066E-13 | -9.513E-14 | -1.340E-13 | -2.552E-13 | -5.415E-13 | — | 2.176E-13 | -4.028E-13 |
| **Cr** | 4.162E-15 | -1.113E-14 | 1.600E-14 | -7.642E-16 | 6.077E-16 | -1.185E-15 | 3.638E-15 | — | -2.993E-15 | 7.591E-15 |
| **Fe** | -2.459E-14 | 1.460E-14 | -1.015E-14 | 5.800E-15 | -8.788E-15 | -4.709E-15 | -1.938E-14 | — | -1.541E-14 | -2.482E-14 |
| **Mn** | 9.314E-17 | -5.414E-17 | 1.912E-16 | 1.734E-16 | 1.943E-14 | 1.794E-16 | 2.376E-16 | — | -1.060E-16 | 3.054E-16 |
| **Mo** | -7.416E-16 | -1.517E-15 | -6.077E-16 | -2.619E-16 | -4.697E-16 | 1.028E-14 | -1.167E-15 | — | 1.303E-15 | -6.907E-16 |
| **Nb** | 6.079E-15 | -2.063E-14 | 6.790E-15 | 4.147E-15 | 6.117E-15 | 3.821E-15 | 4.661E-14 | — | 1.988E-14 | 8.149E-15 |
| **Ni** | -3.639E-14 | 2.210E-14 | -1.542E-14 | -1.090E-14 | -1.953E-14 | -1.095E-14 | -3.310E-14 | — | -4.104E-14 | -4.146E-14 |
| **Si** | 2.315E-16 | 1.418E-16 | 6.869E-17 | 7.253E-17 | 5.234E-17 | 1.371E-16 | 2.062E-16 | — | 3.116E-14 | 2.054E-16 |
| **Ti** | 2.077E-15 | -3.187E-15 | 2.359E-15 | 1.331E-15 | 2.043E-15 | 1.820E-15 | 2.308E-15 | — | 4.932E-15 | 4.996E-14 |

# Bibliography

[1] R. Otis, Software architecture for CALPHAD modeling of phase stability and transformations in alloy additive manufacturing processes, The Pennsylvania State University, United States -- Pennsylvania, 2016, p. 126.

[2] A. Reichardt, Additive Manufacturing of Metal-Based Functionally Graded Materials, University of California, Berkeley, Ann Arbor, 2017, p. 237.

[3] B. Bocklund, Computational Design of Additively Manufactured Functionally Graded Materials by Thermodynamic Modeling with Uncertainty Quantification, The Pennsylvania State University, United States -- Pennsylvania, 2021, p. 163.

[4] A. Reichardt, A.A. Shapiro, R. Otis, R.P. Dillon, J.P. Borgonia, B.W. McEnerney, P. Hosemann, A.M. Beese, Advances in additive manufacturing of metal-based functionally graded materials, International Materials Reviews 66(1) (2020) 1-29.

[5] D.C. Hofmann, J. Kolodziejska, S. Roberts, R. Otis, R.P. Dillon, J.-O. Suh, Z.-K. Liu, J.-P. Borgonia, Compositionally graded metals: A new frontier of additive manufacturing, Journal of Materials Research 29(17) (2014) 1899-1910.

[6] G. Pardal, S. Ganguly, S. Williams, J. Vaja, Dissimilar metal joining of stainless steel and titanium using copper as transition metal, The International Journal of Advanced Manufacturing Technology 86(5) (2016) 1139-1150.

[7] N. Kahraman, B. Gülenç, F. Findik, Joining of titanium/stainless steel by explosive welding and effect on interface, Journal of Materials Processing Technology 169(2) (2005) 127-133.

[8] S. Chen, M. Zhang, J. Huang, C. Cui, H. Zhang, X. Zhao, Microstructures and mechanical property of laser butt welding of titanium alloy to stainless steel, Materials & Design 53 (2014) 504-511.

[9] L.H. Shah, M. Ishak, Review of Research Progress on Aluminum–Steel Dissimilar Welding, Materials and Manufacturing Processes 29(8) (2014) 928-933.

[10] J.C. Zhao, CHAPTER SEVEN - PHASE DIAGRAM DETERMINATION USING DIFFUSION MULTIPLES, in: J.C. Zhao (Ed.), Methods for Phase Diagram Determination, Elsevier Science Ltd, Oxford, 2007, pp. 246-272.

[11] J.C. Zhao, Reliability of the diffusion-multiple approach for phase diagram mapping, Journal of Materials Science 39(12) (2004) 3913-3925.

[12] J.F. Groves, H.N.G. Wadley, Functionally graded materials synthesis via low vacuum directed vapor deposition, Composites Part B: Engineering 28(1) (1997) 57-69.

[13] B.A. Welk, M.A. Gibson, H.L. Fraser, A combinatorial approach to the investigation of metal systems that form both bulk metallic glasses and high entropy alloys, JOM 68(3) (2016) 1021-1026.

[14] H. Dobbelstein, E.L. Gurevich, E.P. George, A. Ostendorf, G. Laplanche, Laser metal deposition of compositionally graded TiZrNbTa refractory high-entropy alloys using elemental powder blends, Additive Manufacturing 25 (2019) 252-262.

[15] J.W. Pegues, M.A. Melia, R. Puckett, S.R. Whetten, N. Argibay, A.B. Kustas, Exploring additive manufacturing as a high-throughput screening tool for multiphase high entropy alloys, Additive Manufacturing 37 (2021) 101598.

[16] D. Kong, C. Dong, X. Ni, L. Zhang, C. Man, J. Yao, Y. Ji, Y. Ying, K. Xiao, X. Cheng, X. Li, High-throughput fabrication of nickel-based alloys with different Nb contents via a dual-feed additive manufacturing system: Effect of Nb content on microstructural and mechanical properties, Journal of Alloys and Compounds 785 (2019) 826-837.

[17] M. Moorehead, K. Bertsch, M. Niezgoda, C. Parkin, M. Elbakhshwan, K. Sridharan, C. Zhang, D. Thoma, A. Couet, High-throughput synthesis of Mo-Nb-Ta-W high-entropy alloys via additive manufacturing, Materials & Design 187 (2020) 108358.

[18] W. Xiong, G.B. Olson, Cybermaterials: materials by design and accelerated insertion of materials, npj Computational Materials 2(1) (2016).

[19] W. Xiong, G.B. Olson, Integrated computational materials design for high-performance alloys, MRS Bulletin 40(12) (2015) 1035-1044.

[20] J. Smith, W. Xiong, W. Yan, S. Lin, P. Cheng, O.L. Kafka, G.J. Wagner, J. Cao, W.K. Liu, Linking process, structure, property, and performance for metal-based additive manufacturing:

computational approaches with experimental support, Computational Mechanics 57(4) (2016) 583-610.

[21] A.R. Moustafa, A. Durga, G. Lindwall, Z.C. Cordero, Scheil ternary projection (STeP) diagrams for designing additively manufactured functionally graded metals, Additive Manufacturing 32 (2020) 101008.

[22] B. Bocklund, L.D. Bobbio, R.A. Otis, A.M. Beese, Z.-K. Liu, Experimental validation of Scheil–Gulliver simulations for gradient path planning in additively manufactured functionally graded materials, Materialia 11 (2020).

[23] N. Sargent, M. Jones, R. Otis, A.A. Shapiro, J.-P. Delplanque, W. Xiong, Integration of Processing and Microstructure Models for Non-Equilibrium Solidification in Additive Manufacturing, Metals 11(4) (2021) 570.

[24] H. Lasi, P. Fettke, H.-G. Kemper, T. Feld, M. Hoffmann, Industry 4.0, Business & Information Systems Engineering 6(4) (2014) 239-242.

[25] K.V. Wong, A. Hernandez, A Review of Additive Manufacturing, ISRN Mechanical Engineering 2012 (2012) 208760.

[26] P. Kurnsteiner, M.B. Wilms, A. Weisheit, B. Gault, E.A. Jagle, D. Raabe, High-strength Damascus steel by additive manufacturing, Nature 582(7813) (2020) 515-519.

[27] D.C. Hofmann, S. Roberts, R. Otis, J. Kolodziejska, R.P. Dillon, J.O. Suh, A.A. Shapiro, Z.K. Liu, J.P. Borgonia, Developing gradient metal alloys through radial deposition additive manufacturing, Sci Rep 4 (2014) 5357.

[28] R. Clinton, T. Prater, N. Werkheiser, K. Morgan, F.E. Ledbetter, NASA Additive Manufacturing Initiatives for Deep Space Human Exploration, (2018).

[29] C. Zhang, F. Chen, Z. Huang, M. Jia, G. Chen, Y. Ye, Y. Lin, W. Liu, B. Chen, Q. Shen, L. Zhang, E.J. Lavernia, Additive manufacturing of functionally graded materials: A review, Materials Science and Engineering: A 764 (2019) 138209.

[30] Y. Li, Z. Feng, L. Hao, L. Huang, C. Xin, Y. Wang, E. Bilotti, K. Essa, H. Zhang, Z. Li, A review on functionally graded materials and structures via additive manufacturing: from multi-scale design to versatile functional properties, Advanced Materials Technologies 5(6) (2020) 1900981.

[31] Y. Chen, X. Zhang, M.M. Parvez, F. Liou, A Review on Metallic Alloys Fabrication Using Elemental Powder Blends by Laser Powder Directed Energy Deposition Process, Materials (Basel) 13(16) (2020) 3562.

[32] D. Svetlizky, M. Das, B. Zheng, A.L. Vyatskikh, S. Bose, A. Bandyopadhyay, J.M. Schoenung, E.J. Lavernia, N. Eliaz, Directed energy deposition (DED) additive manufacturing: Physical characteristics, defects, challenges and applications, Materials Today 49 (2021) 271-295.

[33] A. Dass, A. Moridi, State of the Art in Directed Energy Deposition: From Additive Manufacturing to Materials Design, Coatings, 2019.

[34] Z.-j. Tang, W.-w. Liu, Y.-w. Wang, K.M. Saleheen, Z.-c. Liu, S.-t. Peng, Z. Zhang, H.-c. Zhang, A review on in situ monitoring technology for directed energy deposition of metals, The International Journal of Advanced Manufacturing Technology 108(11) (2020) 3437-3463.

[35] C.J. Todaro, M.A. Easton, D. Qiu, M. Brandt, D.H. StJohn, M. Qian, Grain refinement of stainless steel in ultrasound-assisted additive manufacturing, Additive Manufacturing 37 (2021) 101632.

[36] Z. Wang, T.A. Palmer, A.M. Beese, Effect of processing parameters on microstructure and tensile properties of austenitic stainless steel 304L made by directed energy deposition additive manufacturing, Acta Materialia 110 (2016) 226-235.

[37] M. Koizumi, M. Niino, Overview of FGM Research in Japan, MRS Bulletin 20(1) (1995) 19-21.

[38] C. Lundin, Dissimilar metal welds-transition joints literature review, Welding Journal 61(2) (1982) 58-63.

[39] D.V. Dunford, A. Wisbey, Diffusion Bonding of Advanced Aerospace Metallics, MRS Online Proceedings Library (OPL) 314 (1993) 39.

[40] F. Findik, Recent developments in explosive welding, Materials & Design 32(3) (2011) 1081-1093.

[41] K.P. Mehta, V.J. Badheka, A review on dissimilar friction stir welding of copper to aluminum: process, properties, and variants, Materials and Manufacturing Processes 31(3) (2016) 233-254.

[42] S. Sridar, N. Sargent, X. Wang, M.A. Klecka, W. Xiong, Determination of Location-Specific Solidification Cracking Susceptibility for a Mixed Dissimilar Alloy Processed by Wire-Arc Additive Manufacturing, Metals 12(2) (2022).

[43] S. Sridar, M.A. Klecka, W. Xiong, Interfacial characteristics of P91 steel - Inconel 740H bimetallic structure fabricated using wire-arc additive manufacturing, Journal of Materials Processing Technology 300 (2022) 117396.

[44] R. Ghanavati, E. Lannunziata, E. Norouzi, S. Bagherifard, L. Iuliano, A. Saboori, Design and development of SS316L-IN718 functionally graded materials via laser powder bed fusion, Materials Letters 349 (2023) 134793.

[45] L.D. Bobbio, B. Bocklund, A. Reichardt, R. Otis, J.P. Borgonia, R.P. Dillon, A.A. Shapiro, B.W. McEnerney, P. Hosemann, Z.-K. Liu, A.M. Beese, Analysis of formation and growth of the σ phase in additively manufactured functionally graded materials, Journal of Alloys and Compounds 814 (2020).

[46] L.D. Bobbio, B. Bocklund, R. Otis, J.P. Borgonia, R.P. Dillon, A.A. Shapiro, B. McEnerney, Z.-K. Liu, A.M. Beese, Characterization of a functionally graded material of Ti-6Al-4V to 304L stainless steel with an intermediate V section, Journal of Alloys and Compounds 742 (2018) 1031-1036.

[47] L.D. Bobbio, B. Bocklund, R. Otis, J.P. Borgonia, R.P. Dillon, A.A. Shapiro, B. McEnerney, Z.-K. Liu, A.M. Beese, Experimental analysis and thermodynamic calculations of an additively manufactured functionally graded material of V to Invar 36, Journal of Materials Research 33(11) (2018) 1642-1649.

[48] B.E. Carroll, R.A. Otis, J.P. Borgonia, J.-o. Suh, R.P. Dillon, A.A. Shapiro, D.C. Hofmann, Z.-K. Liu, A.M. Beese, Functionally graded material of 304L stainless steel and inconel 625 fabricated by directed energy deposition: Characterization and thermodynamic modeling, Acta Materialia 108 (2016) 46-54.

[49] T. Weber, J. Aktaa, Numerical assessment of functionally graded tungsten/steel joints for divertor applications, Fusion Engineering and Design 86(2) (2011) 220-226.

[50] P.R. Gradl, C. Protz, S.E. Greene, D. Ellis, B. Lerch, I. Locci, Development and hot-fire testing of additively manufactured copper combustion chambers for liquid rocket engine applications, 53rd AIAA/SAE/ASEE joint propulsion conference, 2017, p. 4670.

[51] P.R. Gradl, C.S. Protz, D.L. Ellis, S.E. Greene, Progress in additively manufactured copper-alloy GRCop-84, GRCop-42, and bimetallic combustion chambers for liquid rocket engines, International Astronautical Congress (IAC), 2019.

[52] M. Rieth, S.L. Dudarev, S.M. Gonzalez de Vicente, J. Aktaa, T. Ahlgren, S. Antusch, D.E.J. Armstrong, M. Balden, N. Baluc, M.F. Barthe, W.W. Basuki, M. Battabyal, C.S. Becquart, D. Blagoeva, H. Boldyryeva, J. Brinkmann, M. Celino, L. Ciupinski, J.B. Correia, A. De Backer, C. Domain, E. Gaganidze, C. García-Rosales, J. Gibson, M.R. Gilbert, S. Giusepponi, B. Gludovatz, H. Greuner, K. Heinola, T. Höschen, A. Hoffmann, N. Holstein, F. Koch, W. Krauss, H. Li, S. Lindig, J. Linke, C. Linsmeier, P. López-Ruiz, H. Maier, J. Matejicek, T.P. Mishra, M. Muhammed, A. Muñoz, M. Muzyk, K. Nordlund, D. Nguyen-Manh, J. Opschoor, N. Ordás, T. Palacios, G. Pintsuk, R. Pippan, J. Reiser, J. Riesch, S.G. Roberts, L. Romaner, M. Rosiński, M. Sanchez, W. Schulmeyer, H. Traxler, A. Ureña, J.G. van der Laan, L. Veleva, S. Wahlberg, M. Walter, T. Weber, T. Weitkamp, S. Wurster, M.A. Yar, J.H. You, A. Zivelonghi, Recent progress in research on tungsten materials for nuclear fusion applications in Europe, Journal of Nuclear Materials 432(1) (2013) 482-500.

[53] J. Zhang, D. Xie, Q. Li, C. Jiang, Q. Li, Effect of holding time on the microstructure and strength of tungsten/steel joints by HIP diffusion bonded using a Cu interlayer, Materials Letters 261 (2020) 126875.

[54] Y. Wang, S. Chen, X. Lei, J. Yang, J. Huang, S. Chen, Z. Ye, Y. Zhao, Interfacial structure and formation mechanism of tungsten/steel HIP diffusion bonding joints using Ni interlayer, Journal of Manufacturing Processes 52 (2020) 235-246.

[55] W. Liu, Z. Wang, Y. Ma, Q. Cai, Investigation of tungsten/steel brazing using Ta and Cu interlayer, Fusion Engineering and Design 113 (2016) 102-108.

[56] D. Bachurina, V. Vorkel, A. Suchkov, J. Gurova, A. Ivannikov, M. Penyaz, I. Fedotov, O. Sevryukov, B. Kalin, Overview of the mechanical properties of tungsten/steel brazed joints for the demo fusion reactor, Metals 11(2) (2021) 209.

[57] G. Mauer, K.-H. Rauwald, Y.J. Sohn, Tungsten-Steel Functionally Graded Coatings for Nuclear Fusion Applications Manufactured by Cold Gas Spraying, Journal of Thermal Spray Technology 32(2-3) (2023) 375-387.

[58] A.D. Iams, T.J. Lienert, D.A. Otazu, M. Ramoni, Effects of deposition sequence on microstructural evolution in additively manufactured Cu-Cr-Nb alloy / superalloy bimetallic structures, Additive Manufacturing Letters 6 (2023) 100151.

[59] D.L. Ellis, GRCop-84: a high-temperature copper alloy for high-heat-flux applications, (2005).

[60] W. Xiong, Additive manufacturing as a tool for high-throughput experimentation, Journal of Materials Informatics 2(3) (2022) 12.

[61] K. Shah, I.u. Haq, A. Khan, S.A. Shah, M. Khan, A.J. Pinkerton, Parametric study of development of Inconel-steel functionally graded materials by laser direct metal deposition, Materials & Design (1980-2015) 54 (2014) 531-538.

[62] J.S. Zuback, T.A. Palmer, T. DebRoy, Additive manufacturing of functionally graded transition joints between ferritic and austenitic alloys, Journal of Alloys and Compounds 770 (2019) 995-1003.

[63] L.D. Bobbio, B. Bocklund, E. Simsek, R.T. Ott, M.J. Kramer, Z.-K. Liu, A.M. Beese, Design of an additively manufactured functionally graded material of 316 stainless steel and Ti-6Al-4V with Ni-20Cr, Cr, and V intermediate compositions, Additive Manufacturing 51 (2022).

[64] A. van de Walle, H. Chen, H. Liu, C. Nataraj, S. Samanta, S. Zhu, R. Arroyave, Interactive Exploration of High-Dimensional Phase Diagrams, JOM 74(9) (2022) 3478-3486.

[65] W.D. Klopp, Review of ductilizing of group VIA elements by rhenium and other solutes, National Aeronautics and Space Administration1968.

[66] H.K.D.H. Bhadeshia, A Commentary on: "Diffusion of Carbon in Austenite with a Discontinuity in Composition", Metallurgical and Materials Transactions A 41(7) (2010) 1605-1615.

[67] J. Zuback, Additive Manufacturing of Functionally Graded Materials between Ferritic and Austenitic Alloys, The Pennsylvania State University2019.

[68] J.E. Morral, Diffusion Path Theorems for Ternary Diffusion Couples, Metallurgical and Materials Transactions A 43(10) (2012) 3462-3470.

[69] J.E. Morral, C. Jin, A. Engstr, J. Ågren, Three types of planar boundaries in multiphase diffusion couples, Scripta Materialia 34(11) (1996) 1661-1666.

[70] A.D. Smigelskas, Zinc diffusion in alpha brass, 1947.

[71] D. Kim, J.-h. Chang, J. Park, J.J. Pak, Formation and behavior of Kirkendall voids within intermetallic layers of solder joints, Journal of Materials Science: Materials in Electronics 22(7) (2011) 703-716.

[72] K. Zeng, R. Stierman, T.-C. Chiu, D. Edwards, K. Ano, K.N. Tu, Kirkendall void formation in eutectic SnPb solder joints on bare Cu and its effect on joint reliability, Journal of Applied Physics 97(2) (2004) 024508.

[73] A. Paul, M.J.H. van Dal, A.A. Kodentsov, F.J.J. van Loo, The Kirkendall effect in multiphase diffusion, Acta Materialia 52(3) (2004) 623-630.

[74] N. Ury, R. Neuberger, N. Sargent, W. Xiong, R. Arróyave, R. Otis, Kawin: An open source Kampmann–Wagner Numerical (KWN) phase precipitation and coarsening model, Acta Materialia 255 (2023) 118988.

[75] A. Borgenstam, L. Höglund, J. Ågren, A. Engström, DICTRA, a tool for simulation of diffusional transformations in alloys, Journal of Phase Equilibria 21(3) (2000) 269-280.

[76] J.O. Andersson, T. Helander, L. Höglund, P. Shi, B. Sundman, Thermo-Calc & DICTRA, computational tools for materials science, Calphad 26(2) (2002) 273-312.

[77] L. Höglund, J. Ågren, Analysis of the Kirkendall effect, marker migration and pore formation, Acta Materialia 49(8) (2001) 1311-1317.

[78] K. Yuan, R. Eriksson, R. Lin Peng, X.-H. Li, S. Johansson, Y.-D. Wang, Modeling of microstructural evolution and lifetime prediction of MCrAlY coatings on nickel based superalloys during high temperature oxidation, Surface and Coatings Technology 232 (2013) 204-215.

[79] T. Böllinghaus, H. Herold, C.E. Cross, J.C. Lippold, Hot cracking phenomena in welds II, Hot cracking phenomena in welds II2008, pp. 1-18.

[80] T. Clyne, G. Davies, A New Hot-Tearing Criterion, Br. Foundrym 74 (1981) 65-73.

[81] S. Kou, A criterion for cracking during solidification, Acta Materialia 88 (2015) 366-374.

[82] J. Liu, S. Kou, Crack susceptibility of binary aluminum alloys during solidification, Acta Materialia 110 (2016) 84-94.

[83] S. Kou, Solidification and liquation cracking issues in welding, Jom 55(6) (2003) 37-42.

[84] R. Otis, Z.-K. Liu, pycalphad: CALPHAD-based Computational Thermodynamics in Python, Journal of Open Research Software (2017).

[85] Q. Chen, B. Sundman, Computation of Partial Equilibrium Solidification with Complete Interstitial and Negligible Substitutional Solute Back Diffusion, MATERIALS TRANSACTIONS 43(3) (2002) 551-559.

[86] T. Kirk, E. Galvan, R. Malak, R. Arroyave, Computational design of gradient paths in additively manufactured functionally graded materials, Journal of Mechanical Design 140(11) (2018) 111410.

[87] O. Eliseeva, T. Kirk, P. Samimi, R. Malak, R. Arróyave, A. Elwany, I. Karaman, Functionally Graded Materials through robotics-inspired path planning, Materials & Design 182 (2019) 107975.

[88] W. Xiong, G.B. Olson, Cybermaterials: materials by design and accelerated insertion of materials, npj Computational Materials 2(1) (2016) 15009.

[89] T. Keller, G. Lindwall, S. Ghosh, L. Ma, B.M. Lane, F. Zhang, U.R. Kattner, E.A. Lass, J.C. Heigel, Y. Idell, M.E. Williams, A.J. Allen, J.E. Guyer, L.E. Levine, Application of Finite Element, Phase-field, and CALPHAD-based Methods to Additive Manufacturing of Ni-based Superalloys, Acta Materialia 139 (2017) 244-253.

[90] H.E. Lippard, C.E. Campbell, V.P. Dravid, G.B. Olson, T. Björklind, U. Borggren, P. Kellgren, Microsegregation behavior during solidification and homogenization of AerMet100 steel, Metallurgical and Materials Transactions B 29(1) (1998) 205-210.

[91] X. Wang, S. Sridar, W. Xiong, Thermodynamic Investigation of New High-Strength Low-Alloy Steels with Heusler Phase Strengthening for Welding and Additive Manufacturing: High-Throughput CALPHAD Calculations and Key Experiments for Database Verification, Journal of Phase Equilibria and Diffusion 41(6) (2020) 804-818.

[92] H. Hyer, L. Zhou, A. Mehta, Y. Sohn, Effects of Alloy Composition and Solid-State Diffusion Kinetics on Powder Bed Fusion Cracking Susceptibility, Journal of Phase Equilibria and Diffusion (2020).

[93] W.J. Sames, F.A. List, S. Pannala, R.R. Dehoff, S.S. Babu, The metallurgy and processing science of metal additive manufacturing, International Materials Reviews 61(5) (2016) 315-360.

[94] X. Yan, J.C. Lin, Prediction of hot tearing tendency for multicomponent aluminum alloys, Metallurgical and Materials Transactions B 37(6) (2006) 913-918.

[95] L. Zhang, Y. Du, I. Steinbach, Q. Chen, B. Huang, Diffusivities of an Al–Fe–Ni melt and their effects on the microstructure during solidification, Acta Materialia 58(10) (2010) 3664-3675.

[96] M.A. Valiente Bermejo, S. Wessman, Computational thermodynamics in ferrite content prediction of austenitic stainless steel weldments, Welding in the World 63(3) (2018) 627-635.

[97] G. Lindwall, C.E. Campbell, E.A. Lass, F. Zhang, M.R. Stoudt, A.J. Allen, L.E. Levine, Simulation of TTT Curves for Additively Manufactured Inconel 625, Metallurgical and Materials Transactions A 50(1) (2018) 457-467.

[98] A.J. Wolfer, J. Aires, K. Wheeler, J.-P. Delplanque, A. Rubenchik, A. Anderson, S. Khairallah, Fast solution strategy for transient heat conduction for arbitrary scan paths in additive manufacturing, Additive Manufacturing 30 (2019).

[99] A. Gilat, V. Subramaniam, Numerical Methods for Engineers and Scientists, Wiley2013.

[100] A.J. Wolfer, Physics-based Surrogate Modeling of Laser Powder Bed Fusion Additive Manufacturing, [Doctoral Dissertation] University of California Davis, 2021.

[101] J. Allison, B. Cowles, J. DeLoach, T. Pollock, G. Spanos, Integrated Computational Materials Engineering (ICME): implementing ICME in the aerospace, automotive, and maritime industries, A Study Organized by the Minerals, Metals & Materials Society. The Minerals, Metals & Materials Society, Warrendale, PA 15086 (2013) 9-10.

[102] I.I. Novikov, Hot-Shortness of Nonferrous Metals and Alloys, FOREIGN TECHNOLOGY DIV WRIGHT-PATTERSON AFB OHIO, 1968.

[103] W. Pumphrey, ‘The Aluminum Development Association Report No. 27, Aluminum Development Association, London (1955).

[104] S.A. Khairallah, A. Anderson, Mesoscopic simulation model of selective laser melting of stainless steel powder, Journal of Materials Processing Technology 214(11) (2014) 2627-2636.

[105] F. Yan, W. Xiong, E. Faierson, G.B. Olson, Characterization of nano-scale oxides in austenitic stainless steel processed by powder bed fusion, Scripta Materialia 155 (2018) 104-108.

[106] M.A. Dayananda, A Direct Derivation of Fick's Law from Continuity Equation for Interdiffusion in Multicomponent Systems, Scripta Materialia 210 (2022) 114430.

[107] J.C. Zhao, X. Zheng, D.G. Cahill, High-throughput diffusion multiples, Materials Today 8(10) (2005) 28-37.

[108] W.-M. Choi, Y.H. Jo, D.G. Kim, S.S. Sohn, S. Lee, B.-J. Lee, A thermodynamic description of the Co-Cr-Fe-Ni-V system for high-entropy alloy design, Calphad 66 (2019) 101624.

[109] G. Lindwall, K. Frisk, Assessment and Evaluation of Mobilities for Diffusion in the bcc Cr-V-Fe System, Journal of Phase Equilibria and Diffusion 30(4) (2009) 323-333.

[110] S. Wen, Y. Du, Y. Liu, C. Du, Z. Zheng, P. Zhou, S. Zhang, M. Chu, Atomic mobilities and diffusivities in fcc_A1 Ni–Cr–V system: Modeling and application, Calphad 70 (2020) 101808.

[111] F. Wang, Y. Du, Q. Min, C. Du, S. Wen, H. Liu, L. Zhong, S. Zhang, M. Chu, Y. Liu, Interdiffusion and atomic mobilities in bcc V–X (X = Mn, Sn and Ni) alloys: Measurement and modeling, Calphad 74 (2021) 102316.

[112] G. Ghosh, Thermodynamic and kinetic modeling of the Cr-Ti-V system, Journal of Phase Equilibria 23(4) (2002) 310.

[113] ouml, B. nsson, ouml, rn, Assessment of the Mobilities of Cr, Fe and Ni in bcc Cr-Fe-Ni Alloys, ISIJ International 35(11) (1995) 1415-1421.

[114] H. Larsson, L. Höglund, Multiphase diffusion simulations in 1D using the DICTRA homogenization model, Calphad 33(3) (2009) 495-501.

[115] J.R. Stephens, W.D. Klopp, Ductility mechanisms and superplasticity in chromium alloys, National Aeronautics and Space Administration1968.

[116] J.P. Galler, J.N. DuPont, S.S. Babu, M. Subramanian, Design of Graded Transition Joints Through Thermodynamic and Kinetic Modeling, Metallurgical and Materials Transactions A 50(6) (2019) 2765-2783.

[117] B. Bocklund, L.D. Bobbio, R.A. Otis, A.M. Beese, Z.-K. Liu, Experimental validation of Scheil–Gulliver simulations for gradient path planning in additively manufactured functionally graded materials, Materialia 11 (2020) 100689.

[118] L.D. Bobbio, B. Bocklund, A. Reichardt, R. Otis, J.P. Borgonia, R.P. Dillon, A.A. Shapiro, B.W. McEnerney, P. Hosemann, Z.-K. Liu, A.M. Beese, Analysis of formation and growth of the σ phase in additively manufactured functionally graded materials, Journal of Alloys and Compounds 814 (2020) 151729.

[119] Z. Sun, Y. Ma, D. Ponge, S. Zaefferer, E.A. Jagle, B. Gault, A.D. Rollett, D. Raabe, Thermodynamics-guided alloy and process design for additive manufacturing, Nat Commun 13(1) (2022) 4361.

[120] N. Sargent, Y. Wang, D. Li, Y. Zhao, X. Wang, W. Xiong, Exploring Alloy Design Pathway Through Directed Energy Deposition of Powder Mixtures: A Study of Stainless Steel 316L and Inconel 718, Additive Manufacturing Letters 6 (2023) 100133.

[121] Y. Kok, X.P. Tan, P. Wang, M.L.S. Nai, N.H. Loh, E. Liu, S.B. Tor, Anisotropy and heterogeneity of microstructure and mechanical properties in metal additive manufacturing: A critical review, Materials & Design 139 (2018) 565-586.

[122] J. Li, T. Cheng, Y. Liu, Y. Yang, W. Li, Q. Wei, Simultaneously enhanced strength and ductility of Cu-15Ni-8Sn alloy with periodic heterogeneous microstructures fabricated by laser powder bed fusion, Additive Manufacturing 54 (2022) 102726.

[123] X. Wang, W. Xiong, Uncertainty quantification and composition optimization for alloy additive manufacturing through a CALPHAD-based ICME framework, npj Computational Materials 6(1) (2020).

[124] T. Yamashita, Y. Tanaka, M. Yagoshi, K. Ishida, Novel technique to suppress hydrocarbon contamination for high accuracy determination of carbon content in steel by FE-EPMA, Sci Rep 6 (2016) 29825.

[125] K. Thompson, D. Lawrence, D.J. Larson, J.D. Olson, T.F. Kelly, B. Gorman, In situ site-specific specimen preparation for atom probe tomography, Ultramicroscopy 107(2) (2007) 131-139.

[126] W. Woo, J.S. Jeong, D.K. Kim, C.M. Lee, S.H. Choi, J.Y. Suh, S.Y. Lee, S. Harjo, T. Kawasaki, Stacking Fault Energy Analyses of Additively Manufactured Stainless Steel 316L and CrCoNi Medium Entropy Alloy Using In Situ Neutron Diffraction, Scientific Reports 10(1) (2020) 1350.

[127] X. Wang, W. Xiong, Stacking fault energy prediction for austenitic steels: thermodynamic modeling vs. machine learning, Science and Technology of Advanced Materials 21(1) (2020) 626-634.

[128] M.S. Pham, B. Dovgyy, P.A. Hooper, Twinning induced plasticity in austenitic stainless steel 316L made by additive manufacturing, Materials Science and Engineering: A 704 (2017) 102-111.

[129] S. Sridar, Y. Zhao, W. Xiong, Cyclic re-austenitization of copper-bearing high-strength low-alloy steels fabricated by laser powder bed fusion, Materials Characterization 166 (2020) 110437.

[130] S. Sridar, Y. Zhao, K. Li, X. Wang, W. Xiong, Post-heat treatment design for high-strength low-alloy steels processed by laser powder bed fusion, Materials Science and Engineering: A 788 (2020) 139531.

[131] A.N. Bhagat, S.K. Pabi, S. Ranganathan, O.N. Mohanty, Aging Behaviour in Copper Bearing High Strength Low Alloy Steels, ISIJ International 44(1) (2004) 115-122.

[132] X. Wang, J. Wang, Y. He, C. Wang, L. Zhong, S.X. Mao, Unstable twin in body-centered cubic tungsten nanocrystals, Nature Communications 11(1) (2020) 2497.

[133] G. Kurdjumow, G. Sachs, Über den Mechanismus der Stahlhärtung, Zeitschrift für Physik 64(5) (1930) 325-343.

[134] Y. Kim, T.-H. Ahn, D.-W. Suh, H.N. Han, Variant selection during mechanically induced martensitic transformation of metastable austenite by nanoindentation, Scripta Materialia 104 (2015) 13-16.

[135] G. Casillas, W. Song, A.A. Gazder, Twins or the omega phase: Which is it in high carbon steels?, Scripta Materialia 186 (2020) 293-297.

[136] T.T. Huang, W.J. Dan, W.G. Zhang, Study on the Strain Hardening Behaviors of TWIP/TRIP Steels, Metallurgical and Materials Transactions A 48(10) (2017) 4553-4564.

[137] Y. Zhang, H. Ding, H. Zhu, X. Zhou, Y. Zhang, N. Jia, Superior strength-ductility combination achieved via double heterogeneities of microstructure and composition: An example of medium manganese steel, Materials Science and Engineering: A 834 (2022) 142443.

[138] N. Saeidi, M. Jafari, J.G. Kim, F. Ashrafizadeh, H.S. Kim, Development of an Advanced Ultrahigh Strength TRIP Steel and Evaluation of Its Unique Strain Hardening Behavior, Metals and Materials International 26(2) (2020) 168-178.

[139] C.-Y. Chou, N.H. Pettersson, A. Durga, F. Zhang, C. Oikonomou, A. Borgenstam, J. Odqvist, G. Lindwall, Influence of solidification structure on austenite to martensite transformation in additively manufactured hot-work tool steels, Acta Materialia 215 (2021).

[140] A. Stormvinter, A. Borgenstam, J. Ågren, Thermodynamically Based Prediction of the Martensite Start Temperature for Commercial Steels, Metallurgical and Materials Transactions A 43(10) (2012) 3870-3879.

[141] D. Herzog, V. Seyda, E. Wycisk, C. Emmelmann, Additive manufacturing of metals, Acta Materialia 117 (2016) 371-392.

[142] T. DebRoy, H.L. Wei, J.S. Zuback, T. Mukherjee, J.W. Elmer, J.O. Milewski, A.M. Beese, A. Wilson-Heid, A. De, W. Zhang, Additive manufacturing of metallic components – Process, structure and properties, Progress in Materials Science 92 (2018) 112-224.

[143] A. Ramakrishnan, G.P. Dinda, Microstructure and mechanical properties of direct laser metal deposited Haynes 282 superalloy, Materials Science and Engineering: A 748 (2019) 347-356.

[144] Y. Zhao, K. Li, M. Gargani, W. Xiong, A comparative analysis of Inconel 718 made by additive manufacturing and suction casting: Microstructure evolution in homogenization, Additive Manufacturing 36 (2020) 101404.

[145] Y. Zhao, F. Meng, C. Liu, S. Tan, W. Xiong, Impact of homogenization on microstructure-property relationships of Inconel 718 alloy prepared by laser powder bed fusion, Materials Science and Engineering: A 826 (2021) 141973.

[146] A. Singh, S. Kapil, M. Das, A comprehensive review of the methods and mechanisms for powder feedstock handling in directed energy deposition, Additive Manufacturing 35 (2020) 101388.

[147] J.A. Glerum, C. Kenel, T. Sun, D.C. Dunand, Synthesis of precipitation-strengthened Al-Sc, Al-Zr and Al-Sc-Zr alloys via selective laser melting of elemental powder blends, Additive Manufacturing 36 (2020) 101461.

[148] C. Wang, X.P. Tan, Z. Du, S. Chandra, Z. Sun, C.W.J. Lim, S.B. Tor, C.S. Lim, C.H. Wong, Additive manufacturing of NiTi shape memory alloys using pre-mixed powders, Journal of Materials Processing Technology 271 (2019) 152-161.

[149] A. Aversa, G. Marchese, E. Bassini, Directed Energy Deposition of AISI 316L Stainless Steel Powder: Effect of Process Parameters, Metals 11(6) (2021) 932.

[150] J. Wanni, J.G. Michopoulos, A. Achuthan, Influence of cellular subgrain feature on mechanical deformation and properties of directed energy deposited stainless steel 316 L, Additive Manufacturing 51 (2022) 102603.

[151] R. Ghanavati, H. Naffakh-Moosavy, M. Moradi, Additive manufacturing of thin-walled SS316L-IN718 functionally graded materials by direct laser metal deposition, Journal of Materials Research and Technology 15 (2021) 2673-2685.

[152] X. Ni, D. Kong, W. Wu, L. Zhang, C. Dong, Deformation-induced martensitic transformation in 316L stainless steels fabricated by laser powder bed fusion, Materials Letters 302 (2021) 130377.

[153] W.-S. Shin, B. Son, W. Song, H. Sohn, H. Jang, Y.-J. Kim, C. Park, Heat treatment effect on the microstructure, mechanical properties, and wear behaviors of stainless steel 316L prepared via selective laser melting, Materials Science and Engineering: A 806 (2021) 140805.

[154] X. Wang, X. Gong, K. Chou, Review on powder-bed laser additive manufacturing of Inconel 718 parts, Proceedings of the Institution of Mechanical Engineers, Part B: Journal of Engineering Manufacture 231(11) (2016) 1890-1903.

[155] S.H. Kim, H. Lee, S.M. Yeon, C. Aranas, K. Choi, J. Yoon, S.W. Yang, H. Lee, Selective compositional range exclusion via directed energy deposition to produce a defect-free Inconel 718/SS 316L functionally graded material, Additive Manufacturing 47 (2021) 102288.

[156] E. Chikarakara, S. Naher, D. Brabazon, Spinodal decomposition in AISI 316L stainless steel via high-speed laser remelting, Applied Surface Science 302 (2014) 318-321.

[157] K. Li, J. Zhan, P. Jin, Q. Tang, D.Z. Zhang, W. Xiong, H. Cao, Functionally Graded Alloys from 316 Stainless Steel to Inconel 718 by Powder-Based Laser Direct Energy Deposition, TMS 2022 151st Annual Meeting & Exhibition Supplemental Proceedings, Springer International Publishing, Cham, 2022, pp. 304-312.

[158] K. Li, X. Wang, W. Xiong, Functionally Graded Material Fabricated by Powder-based Laser Directed Energy Deposition: From Conventional to Complex Concentrated Alloys, Preprints 2022040139 (2022).

[159] T. Koyama, Y. Tsukada, T. Abe, Simple Approach for Evaluating the Possibility of Sluggish Diffusion in High-Entropy Alloys, Journal of Phase Equilibria and Diffusion 210 (2022) 68–77.

[160] K. Biswas, J.-W. Yeh, P.P. Bhattacharjee, J.T.M. DeHosson, High entropy alloys: Key issues under passionate debate, Scripta Materialia 188 (2020) 54-58.

[161] D. Field, L. Bradford, M. Nowell, T. Lillo, The role of annealing twins during recrystallization of Cu, Acta Materialia 55 (2007) 4233-4241.

[162] Y. Zhao, W. Xiong, Influence of Homogenization on Phase Transformations during Isothermal Aging of Inconel 718 Superalloys Fabricated by Additive Manufacturing and Suction Casting, Materials, 2023.

[163] E.F. Bradley, Superalloys: a technical guide, ASM International,Metals Park, OH, United States, 1988.

[164] S.W. Yang, J. Yoon, H. Lee, D.S. Shim, Defect of functionally graded material of inconel 718 and STS 316L fabricated by directed energy deposition and its effect on mechanical properties, Journal of Materials Research and Technology 17 (2022) 478-497.

[165] J. Lu, W. Li, Improvement of tensile properties of laser directed energy deposited IN718/316L functionally graded material via different heat treatments, Materials Science and Engineering: A 866 (2023) 144694.

[166] S. Sridar, Y. Zhao, W. Xiong, Phase Transformations During Homogenization of Inconel 718 Alloy Fabricated by Suction Casting and Laser Powder Bed Fusion: A CALPHAD Case Study Evaluating Different Homogenization Models, Journal of Phase Equilibria and Diffusion 42(1) (2021) 28-41.

[167] A. Di Gianfrancesco, P. Lombardi, D. Venditti, R. Montani, L. Foroni, IN718: Higher temperature application range for an old superalloys, Advances in Materials Technology for Fossil Power Plants - Proceedings from the 7th International Conference (2014) 1268-1282.

[168] W.J. Sames, K.A. Unocic, R.R. Dehoff, T. Lolla, S.S. Babu, Thermal effects on microstructural heterogeneity of Inconel 718 materials fabricated by electron beam melting, Journal of Materials Research 29(17) (2014) 1920-1930.

[169] K.A. Unocic, B.A. Pint, Effect of Environment on the High Temperature Oxidation Behavior of 718 and 718Plus, 8th International Symposium on Superalloy 718 and Derivatives2014, pp. 667-677.

[170] E. Epifano, D. Monceau, Ellingham diagram: A new look at an old tool, Corrosion Science 217 (2023) 111113.